Charge carrier dynamics and interfaces in perovskite solar cells

In order to obtain the academic degree of a

Doctor Engineer (Dr.-Ing.)

From the Department of

Electrical Engineering and Information Technology

Karlsruhe Institute of Technology (KIT)

postulated

Dissertation

From

M.Sc. Diana Paola Rueda Delgado

Born in Bucaramanga, Colombia

First Referee: Prof. Dr. Uli Lemmer

Second Referee: Prof. Dr. Jordi Martorell

Summary

Organometal halide perovskites for solar cells are hybrid semiconductors that recently have caught the attention of the scientific community due to its excellent performance and attractive optical properties. Since then, they have been used in solar cells, LEDs, and lasers, although the mechanisms by which such good performances are obtained are not known completely.

This dissertation presents a study of the optical characteristics of perovskites for thin-film solar cells. Due to their small thickness, the morphology of the layer is sensitive to manufacturing parameters. In this way, the manufacturing process is optimized, trying to improve its characteristics.

Among the challenges perovskites pose for implementation, the lack of stability during operation is one of the most relevant. Therefore, in this dissertation, the reasons for stability losses are also studied. For this purpose, interlayers are used, which introduce changes in the interface of the perovskite with the electron extraction layer, and with the initial purpose of reducing the hysteresis in the current-voltage curve. In addition to reducing it, they stabilize the power extracted from the solar cell under illumination. The effects of degradation on the characteristics of solar cells allow the identification of their origins and propose a solution to avoid or delay damage to the perovskite layer. With this in mind, it is established that the problem of stability does not only lie within the perovskite layer but also in the contact between the layers and in the charge transport within the perovskite solar cell. Careful control of these interfaces, then, facilitates the achievement of stable performances and long lifetimes of the perovskite solar cells.

Zusammenfassung

Organometallhalogenid-Perowskite sind hybride Halbleiter, die in jüngster Zeit aufgrund ihrer hervorragenden Halbleitereingeschaften und attraktiven optischen Eigenschaften die Aufmerksamkeit der Wissenschaft auf sich gezogen haben. Seitdem wurde die exzellente Eignung dieser Materialklasse für verschiedenste opto-elektrische Anwendungen wie z.B. Solarzellen, LEDs und Lasern unter Beweis gestellt. Die physikalischen Mechanismen, die die Grundlage für diese einzigartigen, qualitativ Hochwertigen Eigenschaften bilden, sind jedoch noch weitgehend unbekannt.

Dieses Manuskript stellt eine Studie über die optischen Eigenschaften von Perowskitfilmen für den Einsatz in Dünnschichtsolarzellen dar, die mit dem Spin-Coating-Verfahren hergestellt wurden. Aufgrund des geringen Dicken der Perowskitschichten ist deren Morphologie empfindlich gegenüber kleinen Variationen der Fertigungsparameter. Deshalb muss der Herstellungsprozess durch Feinjustierung dieser Parameter optimiert werden, um hocheffiziente Solarzellen herzustellen.

Eine der größten Herausforderungen für die Kommerzialisierung der Perowskitphotovoltaik ist neben der Herstellung durch die mangelnde Stabilität des Wirkungsgerades während des Betriebs gegeben. Daher werden in der vorliegenden Arbeit zusätzlich die Gründe für diese Stabilitätsverluste untersucht. Zu diesem Zweck werden zusätzliche Nanoschichten zwischen der Perowskit- und der Elektronenextraktionsschicht appliziert, die nicht nur eine Reduzierung der Hysterese in der Strom-Spannungskurve bewirken, sondern die Leistung der Solarzelle unter Sonneneinstrahlung stabilisieren.

Der Vergleich der Stabilität von Solarzellen mit und ohne zusätzlichen Zwischenschichten ermöglicht Rückschlüsse auf die Ursache der Degradationsmechanismen. Ein Hauptresultat dieser Stabilitäts- bzw. Degradationsstudie ist die Tatsache, dass ein Großteil des beobachteten Effizienzverlustes nicht durch die Perowskitdegradation innerhalb des Filmes, sondern vielmehr durch die Instabilität der Grenzflächen des Perowskits mit den Extraktionsschichten zustande kommt. Die Grenzflächendegradation erzeugt eine Barriere für den Ladungstransport durch die Erhöhung der lokalen „Trap-Dichte“. Basierend auf dieser Erkenntnis eröffnet die sorgfältige Modifikation der Grenzflächen innerhalb der Solarzelle vielfältige Möglichkeiten, um eine stabile Betriebsleistung der Solarzelle über längere Zeiten durch Vermeidung bzw. Verzögerung der Degradation zu erzielen.

Resumen

Las perovskitas organometálicas de haluros para celdas solares son un tipo de semiconductor híbrido que recientemente ha atrapado la atención de la comunidad científica debido a su excelente desempeño y atractivas propiedades ópticas. Desde entonces, han sido utilizadas en celdas solares, LEDs y lasers, a pesar de que los mecanismos por los cuales se obtienen tan buenos desempeños no son completamente conocidos.

Con esta disertación se presenta un estudio sobre las características ópticas de la perovskitas para su utilización en celdas solares de películas delgadas. Debido a su delgado grosor, la morfología de la capa es sensible a los parámetros de fabricación. De manera que se optimiza el proceso de fabricación tratando de mejorar sus características.

Entre los retos que presentan las perosvkitas para su implementación, la falta de estabilidad durante su funcionamiento es uno de los más relevantes. Entonces en este dissertationo se estudian también las razones por las que se presenta pérdidas de estabilidad. Para esto se utilizan entrecapas, que introducen cambios en la interfaz de la perovksite con la capa extractora de electrones, y con el propósito inicial de reducir la histéresis en la curva de corriente-voltaje. Además de reducirlo, estabilizan la potencia extraída de la celda solar bajo iluminación. Los efectos de la degradación en las características de las celdas solares nos permiten identificar sus orígenes y presentar propuestas para evitar o retardar los daños a la capa de perovskita. Teniendo esto en cuenta, podemos establecer que el problema de la estabilidad no radica sólo dentro de la perovskita, pero también en el contacto entre las capas y en el transporte de carga dentro de la celda solar de perovskita. El control cuidadoso de estas interfaces, entonces, permite la obtención de un rendimiento estable y una vida larga del dispositivo.

Contents

1. Introduction

Recently in the solar energy research area, perovskite solar cells (PSCs) have become the center of attention given their spectacular rise to fame. PSCs are solar cells with organo-metal halide (OMH) perovskites as the key component for absorbing light and converting it to electricity. This type of perovskites are semiconductors that, given their outstanding optical properties and ease of fabrication (among other reasons), have become the rising star of solar energy research.

The first paper with perovskites for solar cells is published in 2009[1], showing a power conversion efficiency (PCE) of 3.8 %. After just a few years of research, the PCEs achieved with PSCs have reached >20 % [2] and its ever-increasing efficiency has amazed the entire photovoltaic community. Among their many interesting optical properties, the absorption coefficient [3]–[5] and the tunability [6]–[9] of the bandgap have led to many researchers in solar energy research to readdress their efforts and choose the perovskites as the absorber for their devices. In consequence, the number of papers published on the topic has increased from a few dozen per year to thousands of papers per year (Figure 1).

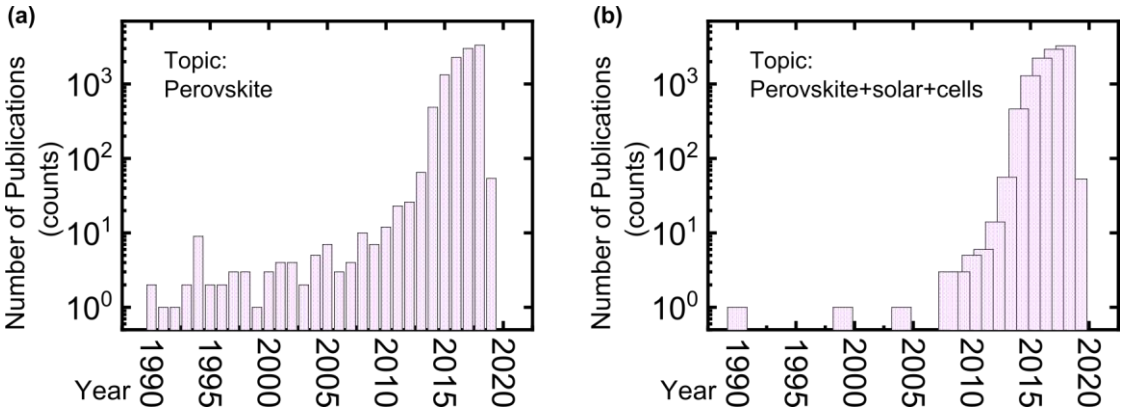

Figure 1. Number of publications on Web of Science, using the keywords: a.) Perovskite and b.) Perovskite solar cells. Source: Web of Science [10].

The combination of PSCs excellent optical properties with the diversity of deposition methods has been the key in the performance enhancement achieved in such a short time (compared to other solar cell types such as organic solar cells). For their fabrication, there is a wide variety of methods used. These methods include doctor blading, drop-casting, spin-coating and thermal evaporation. This versatility offers many fabrication options in comparison to silicon solar cells, which are fabricated using the Czochralski method for fabricating a monocrystalline silicon ingot[11]or by chemical decomposition of silane (SiH_4) as is the case in thin films Si-solar cells [12].

There are still many challenges in PSC's implementation. First, the main component of the perovskite crystalline structure is lead, and its toxicity is well known [13]. Second, the devices are usually short-lived, compared to the 20-year warranty for commercial Silicon solar modules [14]. Third, PSCs are strongly affected by environmental parameters such as air humidity [15],

[16], oxygen [17], temperature [18] and light [19]. Lastly, PSCs show hysteresis during the measurement of their PCE. Hysteresis is the deviation in the J-V curve when measured in the backward and forward direction, or with a different scanning speed. This hysteresis impedes the accurate estimation of the PCE in the devices. As a result of these challenges, much of the research currently addresses different methods to either minimize the damages due to the degradation of the absorber material or to reduce the hysteresis by different methods.

In terms of the underlying principles behind the performance of PSCs, the working mechanisms are not well understood yet. It is then required to analyze their transport properties through the characterization of the devices and layers.

1.1. Aims

The main goal of this thesis is to understand the charge carrier transport in perovskites, given its strong impact on the performance of perovskite solar cells (PSCs). To accomplish this goal I will explore the mechanisms behind the charge transport through the optical and electrical characterization of layers and devices, initially by analyzing the influence of the fabrication parameters in the quality of the layers, as well as its impact in the performance of the devices. Thereafter, I identify the mechanisms that assist the current generation and extraction in full devices. This is later used to improve the devices performance and long term stability.

This dissertation starts with the portrayal in chapter 2 of the fundamental concepts used throughout this dissertation, starting from the description of the band theory that describes the electronic band structure of semiconducting materials, followed by the definition of solar cells and the different technologies that have been implemented. Moreover, the crystalline structure of the perovskites used in PSCs is described in chapter 2, as well as the different architecture used in PSC and the usual architectures used. For the optical and electrical characterization of OMH perovskites, different techniques are used throughout the dissertation. They are described, alongside the underlying principles behind each technique, in chapter 3.

In chapter 4, the different fabrication methods used in this research are described. In chapter 5, the influence of the fabrication parameters in the photoelectric characteristics of perovskite is evaluated as well as the effects on the layer quality and device performance. Additionally, a study on the changes in the wettability of the substrate upon the presence of passivating layers is assessed. The light soaking effect seen in the perovskite absorber is presented, both in steady-state and time-resolved photoluminescence. In this chapter, an estimation of the influence of the fabrication parameters or methods on the absorption of the resulting perovskite layer is evaluated.

In chapter 6, a solution for hysteresis is proposed in the way of a fullerene passivating layer to improve the contact between the electron transport layer and the absorber. In this chapter we present a study of the time-dependent degradation of the devices, using the electrical performance of the devices as media. Upon fabrication, the devices fabricated with passivating layers maintain their power output for a longer time. To explain this boost in their long-term performance, further studies on the different *J-V* curve parameters are executed.

In chapter 7, an evaluation of the degradation of the solar cells is executed in devices with short shelf-time, in comparison to devices that present a longer shelf-time, in order to determine the mechanisms that lead to degradation.

2. Fundamental Concepts in Perovskites for Solar Cells

Solar cells rely on the photoelectric effect and semiconductor materials for their operation. In this chapter, I first describe the theory of electronic bands and the concept of semiconductors. Next, I describe how solar cells work and the different types of cells that exist. Lastly, I describe properties and optical characteristics that are used in the characterization and the concepts on which they are based.

2.1. Band theory and semiconductors

Band theory is a theoretical model used to describe the forbidden and allowed energy ranges in which electrons within the solid may have, differentiating between insulators, semiconductors and conducting materials. This model states that in a crystalline solid, where atoms are arranged in a periodic structure or lattice, there is an almost continuous structure of discretized energy levels for the electrons, forming bands of allowed and forbidden electron energies. The bands closer to the atom core enact little influence as they are deeply bound to the core. The bands that strongly influence the macroscopic properties are those generated by electrons in the outer shells of the atom (valence band, VB). The next (and higher) energy band is the conduction band (CB). The gap between these energy bands is also known as bandgap or forbidden zone. This band structure influences the electrical and optical properties of materials such as their conduction and absorption of electromagnetic radiation and can be grouped in four categories of materials, taking into account interactions between electrons and the nucleus and between the electrons themselves[20].

- Insulators: materials with a large bandgap and no available electrons in the conduction band. Due to these characteristics, they have very high thermal and electrical insulation capabilities (*e.g.* diamond).
- Semiconductors: materials with a small bandgap (~1 eV). Electrons can be excited from the valence to the conduction band with external stimuli such as thermal excitation or illumination, (*e.g.* Germanium, Silicon).
- Conductors type 1: materials with semi-filled conduction band. They are highly conductive both electrically and thermally.
- Conductors type 2 or semimetals: materials with empty conduction band but superimposed to the valence band.

The study of semiconductors and their implementation in different types of electronic devices (transistors, diodes, circuits) has led the current technological development. In the field of solar energy, semiconductors are used as charge carriers (electrons, carriers of a negative charge, and

holes, carriers of a positive charge[1]) generators. For the implementation of semiconductors in electronic devices, impurities are often added to the semiconductor crystalline structure during the fabrication process, creating n-type (doped with excess electrons and known as electron donors) or p-type (with vacancies in the semiconductor lattice and known as hole donors) materials, which will be briefly introduced next.

2.1.1. p-i-n junction

The p-i-n junction is an optoelectronic device that consists of an intrinsic semiconductor (i), an n-type material and a p-type material (Figure 2a). This type of junction is used to improve the charge extraction from a semiconductor device. Unaided, charges can be extracted upon excitation from intrinsic semiconductors placed between two electrodes but they are subject to many losses and, thus, the extraction process is not effective. Materials such as p-(hole) or n-type (electron) are used on either side of the semiconductor, forcing a band bending that ensures that electrons are driven into one direction of the junction and holes in the other direction (Figure 2b). Furthermore, this junction also blocks the back-transfer of charges of the opposite type. In the photovoltaics research field, the p-i-n junction is often used in thin-film solar cells.

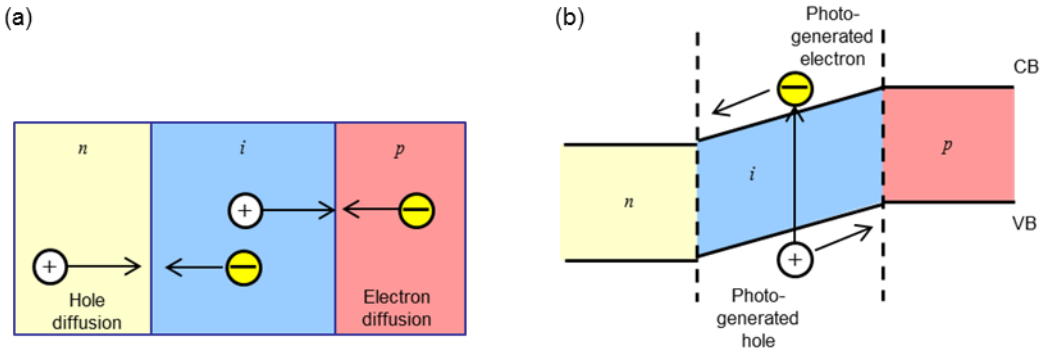

Figure 2. (a) Schematic diagram of a biased p-i-n junction (b) Band diagram of a p-i-n junction under bias voltage[21].

2.2. Solar cells

Solar cells (SC) are optoelectronic devices that use the photoelectric effect for the generation of electric current. The photoelectric effect, first demonstrated by Edmond Becquerel in 1839 [22] and explained by Albert Einstein in 1905 [23], [24], establishes that materials under electromagnetic radiation can generate free electrons. For solar cells, the source of the electromagnetic radiation is the sun, whose radiation is present in a broad spectral range (Figure 3), with the highest intensity in the 300-1100 nm range. As a consequence, the material to be chosen as the main absorber for solar cells should have a bandgap suitable for absorption in this wavelength range.

[1] The term "hole" is used throughout this dissertation following the definition of an "electron hole", that is, the absence of an electron, where there should be one (in an atom or crystal lattice). This absence will exert a net positive charge at the holes location[20].

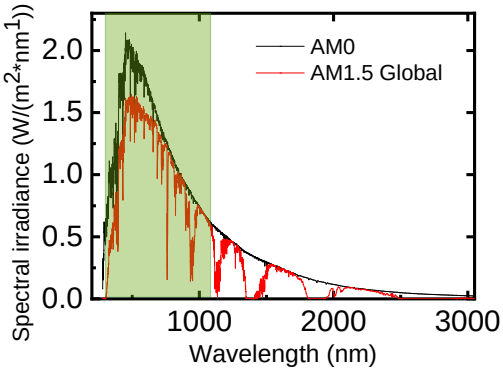

Figure 3. Standard solar spectrum in space (AM0) and terrestrial (AM1.5 Global), following the standards ASTM E490 and ASTMG 173[25]. In green, the 300-1100 nm range is highlighted.

Semiconductors with bandgap from 1-1.8 eV [26] are often used in solar cells with only one absorber, also called single-junction cells. The absorption process in this semiconductor film would be as described:

- Photons with energy lower than the semiconductor bandgap pass through the material as if it is transparent.
- Photons with energy equal to the bandgap have the ability to form an electron-hole pair and are absorbed by the semiconductor.
- Photons with larger energy to the bandgap are absorbed and will discard part of their excess energy through thermal vibrations inside the semiconductor lattice. After the absorption and conversion of the photons into electrons, the next process within a solar cell is charge extraction.

In addition to a semiconductor material to absorb light and generate electrons, a solar cell uses membranes for selective charge collection (also known as extraction layers) to attract the photo-generated charges according to their charge and extract them through the electrodes of the device. n-type materials or wide-bandgap semiconductors are used as electron extraction or transport layer (ETL) and p-type materials are used as hole transport layers (HTL).

2.2.1. Types of solar cells

Since the demonstration of the photoelectric effect in 1839, many types of solar cells have been proposed:

Silicon solar cell: Using silicon as the absorber material, these cells are the most commercially available. For the implementation, both monocrystalline and polycrystalline silicon are used. The record power conversion efficiencies (PCE) are 26.1% for the monocrystalline silicon and 22.3% for multicrystalline silicon SC [27]. The advantages they present include the long lifetime (20 years guaranteed [14]) and their low toxicity. Silicon is also an indirect band semiconductor (and this induces additional losses in the current extraction process).

Thin-film cells: So-called due to the thin thickness of the absorber material (from a few nanometers to tens of micrometers[2]). For the absorbent material, several semiconductors are used including CIGS (Cadmium-indium-gallium selenide, [28]), chalcopyrites ($Cu(In, Ga)(S, Se)_2$ [29]), sensitized high bandgap semiconductors[30] and perovskites.

Organic solar cells: organic semiconductors are used as absorber materials. Among the advantages they present is the reduction of fabrication costs and the diversity of substrates that can be used to implement them (flexible substrates [31] or wear-on PV [32], [33]). However, after 20 years of doing research on the subject, the highest PCE is 15.6% [27].

Dye-sensitized solar cells (DSSC): this type of cell uses a wide bandgap semiconductor (~3eV) that is sensitized by a dye absorbing in the visible range (380-740 nm) to increase light absorption in smaller energies. DSSCs were developed by Brian O'Regan and Michael Grätzel in 1991 as a thin-film solar cell with a wide band-gap semiconductor sensitized by an organic dye [34]. DSSCs consist of a mesoporous n-type titania (titanium dioxide, TiO_2) layer that collects photo-generated electrons, a sensitizing dye to infiltrate the mesoporous titania and absorb light in the visible range, and an electrolyte to regenerate the electrons in the dye. The main disadvantage of DSSCs is their low efficiency. Nonetheless, due to their promising performance, different strategies are being followed in order to achieve competitive efficiencies. One of the first steps to boost the DSSC's efficiency is the insertion of quantum dots as absorbers over the mesoporous layer. They are deposited alongside the dye, due to their bandgap tunability through variable particle size. However, overall efficiency has only reached 8.6 % [35], mostly due to charge recombination [36] generated by significant losses at the semiconductor-sensitizer interface [1].

2.2.2. Perovskites for solar cells

Another proposed solution for the DSSCs is the replacement of the dye as the sensitizer by organo-metal halide (OMH) perovskites. The efficiencies obtained with this architecture barely reached 3 % but this result launched the research of perovskite as an absorber for SCs [1]. After this implementation, a new branch of thin-film solar cells was established with OMH perovskites as the absorber material in SCs [37]. OMH perovskites as the main absorber in solar cells are first used in photovoltaics in 2009, achieving very low power conversion efficiency (PCE) [1], but the perovskite optical properties showed a lot of promise. Since then, perovskites have become the rising star of the solar energy research field, reaching PCE >20 % in less than 10 years.

Advantages of using organo-metal halide perovskite for solar cells include:

- Their advantageous intrinsic optical properties: the absorption coefficient in the visible range is higher in OMH perovskites than in crystalline silicon[38];
- The bandgap tunability: Perovskites can be fabricated from a variety of precursors and changing the ratio between precursors materials allows for a precise tunability of the bandgap either by mixing the organic cations or by using a mixture of halides for the inorganic ion [39], [40]; and

[2] Thin in comparison with the silicon wafers, which can be implemented up to 200 μm in devices [226]

- The assortment of fabrication methods: perovskites have been fabricated using solution-processed spin-coating [41], inkjet-printing [42], dip-coating [43], blade-coating [44], and thermally evaporation [39].

The conjunction of these characteristics offers a wide range of options for improving the efficiency in SCs and adapting it even further to other optoelectronic devices, such as LEDs [45] or lasers [46].

2.2.2.1. Organometal halide perovskites

Perovskites are materials that take their name from the perovskite mineral (calcium titanate, $CaTiO_3$), as they have the same crystalline structure. The general formula is ABX_3, where X is an anion that can be replaced by either carbon, oxygen, nitrogen or by the halogen elements [47], while the A and B are mono- or divalent cations that stabilize the structure (Figure 4). By changing the ions, the characteristics of the perovskite change. The perovskite family of materials is known for the diverse characteristics that can be present, such as ferroelectric behaviour [48]; superconductivity at high temperature or increase of their ionic conductivity due to oxygen vacancies [49]; and, acting as insulators or having photovoltaic properties due to their high absorption coefficient [47]. For SCs applications, OMH perovskites are used, where X is a halide anion; A, a monovalent organic cation and B, a metal cation [5].

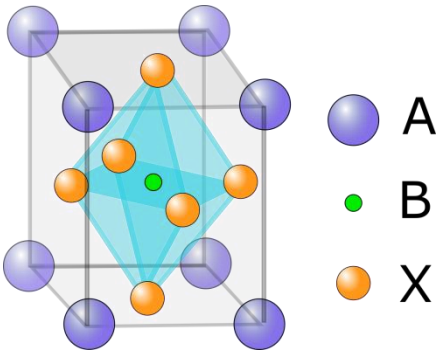

Figure 4. Crystalline structure of perovskites including a monovalent organic cation (A), a metal cation (B) and a halide anion (X).

The OMH perovskites follow the ABX_3 formula with the following components:

- A is an organic cation with oxidation state +1 (such as methylammonium (MA, $CH_3NH_3^+$), ethylammonium ($CH_3CH_2NH_3^+$) and formamidinium (FA, $NH_2CH{=}NH_2^+$) [50], [51]).
- B is a metallic cation with oxidation state +2 (tin (Sn^{2+}) or lead (Pb^{2+})) and
- X is a halide anion with oxidation state -1 limited to chloride (Cl^-), bromide (Br^-) and iodide (I^-) [47].

The first perovskite used for SCs is methylammonium lead tri-iodide ($CH_3NH_3PbI_3$) [37]. Deposited from two precursor materials (methylammonium iodide (MAI) and lead iodide (PbI_2)), this perovskite was the starting point for perovskite solar energy research. In order to improve its open circuit voltage and tuning the bandgap for different applications, other types of perovskite have been studied as well.

Methylammonium lead tri-iodide using $PbCl_2$ precursors is used as well [47], [52]–[57]. The addition of chlorine to the precursor materials modifies the morphology of the final perovskite layer, improving the crystalline structure and its optoelectrical properties [6], [58]. Layers of $MAPbI_{3-x}Cl_x$ have shown longer diffusion lengths than $CH_3NH_3PbI_3$ [59] and chlorine has shown a role in improving carrier transport [58]. Perovskite layers using $PbCl_2$ as lead precursors are deposited in a number of ways: directly from MAI and lead chloride ($PbCl_2$ [57]), or from MAI and a mixture of lead acetate ($PbAc_2$) and $PbCl_2$ [60], among others. There is, however, still some disagreement on whether the chlorine content from the precursor remains in the perovskite layer after annealing. A possible explanation is that a small percentage of chloride remains in the structure after annealing [61], [62] while some studies prove that there is no evidence of chloride left in the layer [63], [64]. In this document, I will use the $MAPbI_{3-x}Cl_x$ or MAPI notation for perovskite layers fabricated from precursors that include $PbCl_2$, to differentiate from $MAPbI_3$, fabricated only with PbI_2 precursors.

Mixed cation lead perovskites are another type of perovskites used in solar energy research since 2016 [65]. The organic precursors are prepared as a mixture of two organic cation sources (MA and FA [66]) with cesium (Cs) (for the triple cation perovskite, [67]). This has been shown to stabilize the FA phase and influence the crystal growth [9]. Additionally, for the halide component, a mixture of iodine and bromide is used to stabilize the perovskite structure at room temperature[68]. The general formula used to address these types of perovskite is $MA_y FA_{1-y} Pb (I_{1-x}Br_x)_3$ for double-cation perovskite and $Cs_z (MA_yFA_{1-y})_{1-z} Pb (I_{1-x}Br_x)_3$ (with x, y and z ranging from 0 to 1) for triple-cation perovskite.

Tin perovskites have also been investigated alongside the lead perovskites [69]–[72], although to a lesser degree. The tin iodide perovskites are strongly affected by air and moisture[73]. In order to maintain most of their performance in humid air for 15 days, mixed cation perovskites have been used (cesium with either MA or FA, [73]) as precursors for the organic part. These latter types of perovskite (mixed cation lead-based, and tin-based) are not studied in this document.

2.2.2.2. Working principle

The first PSCs are similar in their structure and working principle to the DSSCs: a compact layer of a wide-bandgap semiconductor is deposited over a transparent conductive substrate. On top of this, a layer of n-type mesoporous semiconductor is deposited to lengthen the recombination time of photo-generated electrons [74]. Titanium dioxide [75]–[77] and tin oxide [78], [79] are widely used, but others, such as aluminum oxide have also been used as scaffold [80], [81].

The perovskite layer deposited over a mesoporous layer can be performing in different capabilities:

- as a sensitizer, the perovskite infiltrating the n-type layer [82]–[85];
- as an absorber conformally coating an insulating layer (which acts only as scaffold),

A schematic diagram of PSC architectures can be seen in Figure 5. The most commonly used architecture is the n-i-p structure [43], [86], [87]. In this structure, the perovskite layer lies between an n-type material to act as electron transport layer (ETL) for electron extraction and a

p-type material to act as hole transport layer (HTL) for charge regeneration at the perovskite layer. By ensuring that the fabricated layers maintain homogeneous and planar surfaces, the efficiency of the devices is greatly increased [88]–[90]. Over the perovskite layer, a hole transport layer (HTL) is deposited, regenerating the perovskite after electron depletion. Finally, the circuit is closed with a metal electrode, usually gold, since lead-based perovskites corrode silver electrodes [91].

Devices with an inverted architecture (p-i-n) are also implemented using often organic layers for charge extraction, such as PEDOT:PSS (poly(3,4-ethylene dioxythiophene) polystyrene sulfonate) as p-type layer, and PCBM (phenyl-C_{61}-butyric acid methyl ester) or nickel oxide (NiO) as an n-type material [92].

Mesostructured cells have also been implemented, where the electron transport material is replaced by an insulator that acts as a scaffold for the perovskite layer [93]. In this type of cell, the electron charge transport occurs within the perovskite layer. HTL-free devices [94] have been implemented as well to a lesser degree, as evidence of the ambipolar (*i.e.* conduction of both electrons and holes) charge transport properties of perovskites [95], [96].

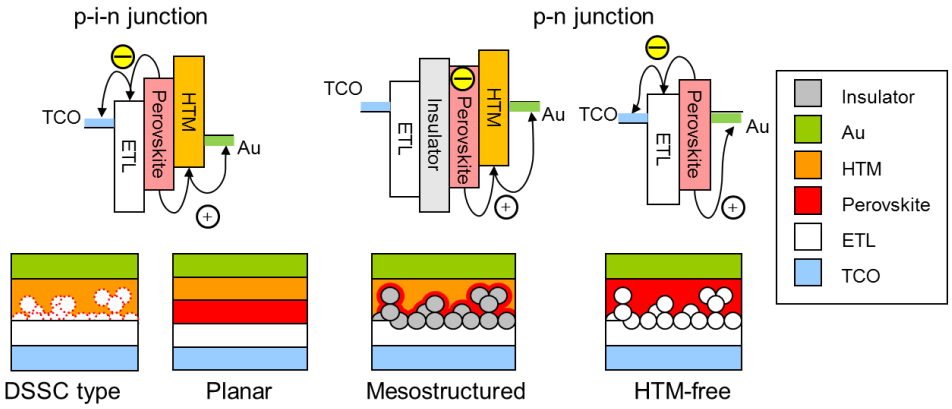

Figure 5. PSCs Architectures and the schematic of the band diagram. HTM: hole transfer material; ETL: electron transfer layer; TCO: transparent conductive oxide

There are currently two main principles for current generation within Perovskite-based Solar Cells, according to the layers inside the architecture. For PSC with DSSC and planar architectures, the photoactive layers form a p-i-n junction. In this case, the performance of the solar cell under illumination is described as follows: the solar cell, connected to an external load is illuminated. A photon with energy higher than the perovskite bandgap is absorbed by the perovskite layer and it excites an electron into the conduction band. This generates an electron-hole pair within the perovskite: an electron in the conduction band and a hole in the valence band. The charge separation occurs through two processes: the excited electron passes to the conduction band of the ETL (*e.g.* a TiO_2 mesoporous layer) and it is transported to the electrode for extraction (Figure 5, p-i-n junction). In the valence band of the perovskite, a positive charge (hole) is left behind and then regenerated to its original state by electrons from the HTM (e.g a SpiroMeOTAD layer), increasing the separation of charges. Holes are thus transported from the HTL into the electrode where it is finally extracted to an external load.

The second principle for current generation applies to mesostructured cells with an insulator used as a scaffold (for example, Al_2O_3) and HTM-free cells. Perovskites can act as absorbers, but also as electron and hole transport materials. Since the crystalline structure of perovskites allows the ambipolar transport [95], [96], the electron transport is executed within the perovskite itself (Figure 5, [50]). For these architectures, perovskite properties such as the long charge carrier diffusion length maintain the photovoltaic performance of the cell.

2.2.2.3. Challenges for OMH perovskites

Despite its many advantages, perovskites as absorbers for SCs face obstacles before an industrial implementation at a large scale is possible. A better understanding of the perovskite's structure, properties, and performance within a solar cell is paramount to bring this solar cell technology closer to industrial application.

The main challenges that need to be overcome for a large scale implementation of perovskite-based SCs are:

- the content of lead in the perovskite structure;
- the fast degradation of devices;
- the sensitivity of perovskites to oxygen and moisture;
- hysteresis in the *J-V* characteristic curve.

In terms of the perovskite itself, the sole *presence of lead* in its crystalline structure is a deterrent for the implementation of perovskites in solar cells and consequent use in a commercial capacity. The toxicity of the lead is well known [13], [97], and initial solutions have been proposed for overcoming this challenge. Replacing lead within the perovskite crystalline structure for another element from the same periodic table group [98], [99], tin perovskites have been proposed as a solution. However, recent studies have estimated that tin-based perovskites are not a substitution that is entirely toxicity-free [100]. Antimony, bismuth [101] and titanium [102] have also been suggested. Despite all these attempts, the performance of the lead-free perovskite solar cells is poorer compared to that of lead-based perovskites [2].

Degradation of the perovskite layers in the devices leads to a loss in electrical performance [103]–[105] and leakage of toxic material into the environment. A solution proposed to solve the latter issue is the encapsulation of the devices. The encapsulation consists of insulating the device in a transparent polymer [106], [107], with access only to the electrodes for electrical connection. The encapsulation has a two-fold purpose: to avoid leaking of lead waste from the device into the environment [108], and to prevent leakage of air and moisture into the device [16], [109]. This addition to the solar cell architecture is still being evaluated as the encapsulation introduces losses in the performance due to reduced incident light and it increases the cost of the entire device.

Due to the perovskite's *sensitivity to oxygen and moisture*, the life of the devices is currently short. Even factors related to solar cell implementation such as light exposure [19], [110] and temperature variations[18] contribute to the degradation and lower the performance even further [111]. Although device stability has been extended —maintaining 80 % of the initial

performance after 1000 h [112]—, it is still not comparable to that of silicon SCs (of 20 years [14]).

A challenge that has arisen in the evaluation of the performance of PSCs is the presence of *hysteresis* in the *J-V* characteristic curve. This phenomenon (described in more detail in Section 3.3) is first mentioned by Snaith *et al*. in 2014 [113] and it is seen as a discrepancy in the current extracted when the *J-V* measurement is executed under various starting conditions. Changing the measurement speed or the applied starting voltage delivers altered *J-V* curves with a range of power conversion efficiencies (PCE) for the same incident light, making the measurement of the real PCE a challenge. Reduction of the hysteresis in PSCs is paramount to determine accurately the performance of the solar cells.

Sources of the hysteresis in the *J-V* characteristic curve have been related to [114]–[116]:

- ion migration within the perovskite layer and
- charge trapping and detrapping at the perovskite interfaces

One of the sources of hysteresis in PSCs is the existence of *ion migration* within the perovskite layer, which consists of the drift of mobile ions in the perovskite layer due to vacancies. As a result, when a potential differential is applied to the perovskite solar cell or device (as is the case during the *J-V* curve measurement), the ions drift within the perovskite layer and accumulate at the interfaces [92]. This ion migration within the layer presents resistance to the current flow [117] and is reflected as a modification of the shape in the *J-V* characteristic curve that will depend on the measurement scan direction and speed.

Another source of hysteresis in PSCs is the *charge (de)trapping* in the interfaces. During the *J-V* measurement, charges can become trapped at the interface with either the HTL or ETL [118], [119]. It has been reported [120], [121] that the influence of both mechanisms during the measurement is the origin of the hysteresis in the *J-V* characteristic curve (Figure 13b).

In order to reduce the hysteresis due to ion migration, changes in the ratio of the perovskite precursors [122] or additives to the perovskite layer [123] have been implemented. Furthermore, to lessen the influence of charge trapping and detrapping, interface engineering has been employed [124] through the use of passivating layers [125] or double-layered contacts [126].

3. Characterization Techniques

In this chapter I describe the characterization techniques used in the following chapters during the evaluation of the perovskite layers and solar cells, and the evaluation of fabrication parameters on the layer quality.

For the evaluation of the influence of fabrication methods and to determine the processes that improve performance, characterization of the perovskite layers and solar cells is executed using several methods. Since solar cells are optoelectrical devices, both optical and electrical characterizations are required for an integral evaluation.

For evaluating the perovskite layers, the following techniques are investigated:

- photoluminescence characterization, which reflects the material quality and the efficiency of the charge transport (Section 3.1),
- transmittance and reflectance spectra which measures the transmission and absorption of materials for the estimation of the diffusion length (Section 3.2),
- x-ray diffraction, to study the crystalline structure of the layers (Section 3.5),
- scanning electron microscopy and atomic force microscopy for imaging the layers and their topography.

For evaluating the perovskite solar cells (PSCs), the following techniques are investigated:

- Current density-voltage (*J-V*) measurement of the devices, to determine the power conversion efficiency (PCE) and other photovoltaic parameters (Section 3.3),
- Evolution of the PCE under constant voltage, to establish the stability of the devices in time,
- Absorption measurements, in order to obtain the external quantum efficiency (EQE) spectra, to determine the spectral response of the PSCs and the loss mechanisms (Section 3.4).

3.1. Photoluminescence

Characterization of the photoluminescence (PL) is a method to detect changes in the quality of a material, giving a measure of the optical bandgap (E_g). In this technique, the layer under study is illuminated, or equivalently, optically excited using a photo-emitting light source (*e.g.* a laser) with energy higher than the bandgap of the material.

Photoluminescence emission can be measure in steady-state mode, to determine the bandgap of the layer under study, or in time-resolved mode, to evaluate the changes in PL intensity through

time. In this mode, the charge carrier lifetime can be estimated and charge transport mechanisms can be studied.

3.1.1. PL concepts

Photoluminescence (PL) is the emission of a photon due to the absorption of light in a semiconductor. Incoming photons with energy equal or higher than the bandgap are absorbed, exciting the electrons from the valence band into higher energy states (Figure 6). In other words, electrons (negative charges) are excited to the conduction band, leaving holes (positive charges) in the valence band. These photo-generated charges transmit the excess energy through the crystal lattice until they reach the lower edge of the conduction band, in a process called relaxation. Then, the electron at the edge of the conduction band recombines with holes in the valence band and this energy is emitted as a photon. The number of photons radiated in this PL process reflects the quality of the material.

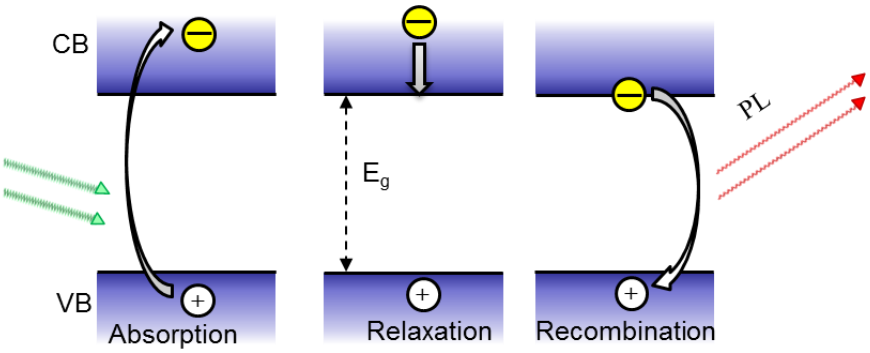

Figure 6. Schematic diagram of the radiative recombination upon illumination. In yellow circles, photo-generated electrons upon incident photons (green arrows) are shown; in white circles, holes or positive charges are shown. E_g: energy bandgap; PL: photoluminescence.

In practice, the absorption of a photon with energy larger than the bandgap (E_g) can generate different types of recombination [127]:

- Radiative recombination: the absorption of the photon leads to the excitation of an electron into the conduction band, leaving a hole in the valence band, known as an electron-hole pair. In the radiative recombination of the electron-hole pair, a photon with energy close to the bandgap is emitted as PL (Figure 6).
- Shockley-Read-Hall recombination: this is a type of non-radiative recombination, in which a photo-excited electron in the conduction band reaches an intermediate state in the energy bandgap (E_g). From this state, the photo-excited electron reaches a hole in the valence band. The excess energy is then thermally transmitted within the crystal.
- Auger recombination, or three-body recombination: a photo-excited electron recombines with a hole in the valence band, transmitting its energy to a second electron in the conduction band, instead of emitting a photon. This second electron then thermally dissipates the excess energy to reach the edge of the conduction band.

For PL measurements, the dominating recombination type and the photo-generated charge carrier density are determined by the fluence of the incident light. The fluence is defined in Eq

(3.1) as the incident laser pulse energy on the effective focal spot area and it is given in units of J/cm^2 [128]. The photo-generated charge carrier density (n) at the surface is calculated using Eq. (3.2):

$$\text{Fluence} = \frac{Pulse\ Energy}{Area} \tag{3.1}$$

$$n = \frac{Fluence * \alpha}{E_{ph}} \tag{3.2}$$

where E_{ph} is the energy of the incident photon and α the absorption coefficient of the semiconductor at the incident wavelength. For low fluences, the generated PL signal is linearly proportional to the photo-generated charge carrier density (n). The limit of the linear regimen for perovskites is n~3.7x10^{17}/cm^3 [129]. Exciting the perovskite layer with incident light in the linear fluence regime ensures that the response measured is that of monomolecular recombination, often related to trap-assisted recombination [127], [130]. Higher fluence will generate PL signals that are no longer following a single exponential response. For intermediate fluences, the PL is proportional to n^2, since it reflects the bimolecular charge carrier recombination [127]. For higher fluences, the PL is proportional to n^3, where the Auger recombination dominates the PL signal and quenches it much faster [127].

Under low fluences [131], the PL emission is linearly proportional to the photo-generated charge carrier density. Therefore the decay of the PL signal in time can be modeled for thin layers using the one-dimensional (1-D) diffusion equation [127]. This equation (also called the continuity equation) describes how the charge carrier density changes in time along one dimension and it is given by Eq. (3.3).

$$\frac{\partial \mathrm{n}}{\partial \mathrm{t}} = \mathrm{D}\frac{\partial^2 \mathrm{n}}{\partial \mathrm{z}^2} - \frac{\mathrm{n}}{\tau} + G(z), \tag{3.3}$$

where n is the charge carrier distribution, D is the diffusion coefficient, τ is the PL lifetime of the layer and G is the generation rate in which the charges are generated by an external field in terms of position within the absorber thickness (set as z in Eq. (3.3), [132]). For pulsed excitation such as the one used in time-resolved photoluminescence, the generation rate is set to zero as there is not further excitation after photoexcitation.

3.1.2. Estimation of the diffusion length

With time-resolved photoluminescence (trPL), optical parameters such as the diffusion coefficient can be calculated. Shaw *et al.* [133] used this method to calculate the exciton diffusion in organic semiconductors, and it has also been used to determine diffusion coefficients in semiconductors like silicon [134] and perovskites [135]. It should be noted, that for the perovskites, the photo-generated electron-hole pairs have binding energies below the thermal energy at room temperature [136] and are therefore considered free charges[130], [137].

The time-dependent PL emission of an absorber such as perovskites on an insulating substrate is measured (Figure 7, left). The emission presents a single exponential decay given by:

$$I(t) = I_0 * e^{-t/\tau_e} \tag{3.4}$$

where I_0 is the maximum intensity and τ_e is the time that it takes for the PL signal to reach 1/e of its maximum intensity. Additionally, to account for other types of recombination, a stretched exponential is often used to fit the PL signal:

$$I(t) = I_0 * e^{-(t/\tau_s)^{\beta_s}} \tag{3.5}$$

where τ_s is the lifetime of the stretched exponential and β_s is a dispersion factor between 0 and 1, as used in [135]. β is associated with the disorder within the crystal, whether due to variation of crystallite sizes or due to grain boundaries [138].

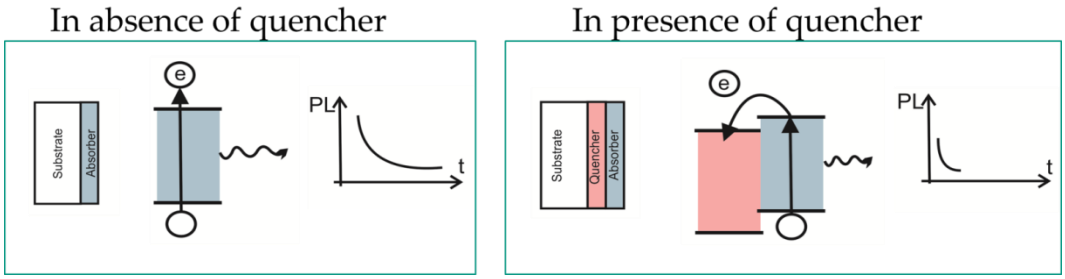

Figure 7. Schematic diagram of the architecture system used for extraction of the diffusion length based on the time-resolved photoluminescence: (left) the absorber on an insulating substrate and (right) in presence of an electron quencher. Thicknesses of layers in the schematic diagram are not in scale.

The measurement of the PL in the absorber itself provides information on the effective charge carrier decay within the film, but it does not determine the charge carrier dominating the decay. For that, the absorber is also measured on an electron quencher or on a hole quencher (Figure 7, right), resulting in the loss of photoluminescence in comparison to the absorber in an insulating substrate. This loss depends on the diffusion length of the semiconductor and the thickness of the semiconductor. The selection of the quencher layer is crucial: first, the quencher is either an n-type (for electrons) or p-type (for holes) material that facilitates the charge extraction. Also, the interface between the semiconductor and the quencher should be stable and well-defined, where the free charges are effectively disassociated. Last, no diffusion should occur between the two layers otherwise the level of quenching will be underestimated [133].

By fitting the normalized PL signal with the solution of the diffusion equation (Eq. (3.3)), parameters such as the diffusion coefficient can be extracted:

$$\frac{\partial n(z,t)}{\partial t} = D\frac{\partial^2 n(z,t)}{\partial z^2} - k(t) * n(z,t), \tag{3.6}$$

where n is the charge carrier distribution, D is the diffusion coefficient, and k(t) is the PL decay rate without quencher [135]. The PL decay rate is defined as:

$$k = k_r + k_{nr} = \beta * {\tau_S}^{-\beta_S} * t^{\beta-1} \tag{3.7}$$

To solve this equation, the boundary and initial conditions must be defined.

For the model, all charge carriers must be generated in the perovskite surface so the initial distribution is given by $n(z,0) = n_0 e^{-\alpha z}$, where α is the absorption coefficient at the excitation wavelength and n_0 is the initial charge distribution. Also, all charge carriers are quenched only

in the perovskite/quencher interface (as opposed to the perovskite/substrate interface) so: $n(L,t) = 0$. This applies for diffusion lengths longer than the thickness of the perovskite layer [139]. With these conditions taken into account, the equation can be solved for the charge carrier distribution:

$$n(z,t) = 2n_0 e^{-kt} \sum_{m=0}^{\infty} \left(e^{-\frac{\pi^2 D}{L}\left(m+\frac{1}{2}\right)^2 t} \cdot \frac{(-1)^m \cdot e^{-\alpha L} \cdot \pi\left(m+\frac{1}{2}\right) + \alpha L}{(\alpha L)^2 + \pi^2\left(m+\frac{1}{2}\right)^2} cos\left(\pi\left(m+\frac{1}{2}\right)\frac{z}{L}\right) \right) \tag{3.8}$$

The charge carrier density is integrated over the active layer thickness, we can obtain the number of charges N(t) [129]:

$$N(t) = \frac{2 * n_o * L}{\pi} * e^{-k*t} * \sum_{m=0}^{\infty} \left(e^{-\frac{\pi^2}{L^2}*D*\left(m+\frac{1}{2}\right)^2 *t} * \frac{e^{-\alpha*L} * \pi * \left(m+\frac{1}{2}\right) + (-1)^m * \alpha * L}{\left((\alpha * L)^2 + \pi^2 * \left(m+\frac{1}{2}\right)^2\right)\left(m+\frac{1}{2}\right)} \right) \tag{3.9}$$

If other types of recombination are included, the number of charges changes to:

$$N(t) = \frac{2 * n_o * L}{\pi} * e^{-\frac{A}{B+1}*t^{B+1}} * \sum_{m=0}^{\infty} \left(e^{-\frac{\pi^2}{L^2}*D*\left(m+\frac{1}{2}\right)^2 *t} * \frac{e^{-\alpha*L} * \pi * \left(m+\frac{1}{2}\right) + (-1)^m * \alpha * L}{\left((\alpha * L)^2 + \pi^2 * \left(m+\frac{1}{2}\right)^2\right) * \left(m+\frac{1}{2}\right)} \right) \tag{3.10}$$

with $A = \beta_s * \tau_s^{-\beta_s}$, $B = \beta_s - 1$, and the diffusion coefficient as the unknown variable [139], Eq. (3.10) is fitted to the normalized PL decay of the quenched sample and the diffusion coefficient can be extracted for electrons and holes. Once known, the diffusion length can be calculated from $L_D = \sqrt{D * \tau_e}$ [140], where the diffusion coefficient depends on the type of charge and the lifetime is measured in the absence of a quencher.

Another parameter to observe the efficiency of charge injection is the charge transfer efficiency (CTE) [141]. It is a figure of merit of the efficiency of the conversion from charge generation in the absorber to injection in the quencher. It is given by:

$$CTE = \frac{k_T}{\tau_A^{-1} + k_T} \tag{3.11}$$

where k_T is the sum of the transfer rate of all available acceptors and it is given by:

$$k_T = \frac{1}{\tau_{AQ}} - \frac{1}{\tau_A} \tag{3.12}$$

where τ_{DA} is the PL lifetime of the absorber in the presence of a quencher and τ_D is the PL lifetime of the absorber in the absence of a quencher.

3.1.3. PL Setup

In order to measure the photoluminescence in perovskite layers, the setup shown in Figure 8 is used. A green pump laser (532 nm, AOT ACE Laser) is used to illuminate the sample, with a temporal resolution of 2.5 ns. The emitted light is measured using an ACTON spectrometer and a gated ICCD (intensified charge-coupled device) camera PIMAX512 with a gated mode at room temperature. Unless otherwise stated, the fluence used in the experiments is 500 nJ/cm^2, in order to excite the absorber in the low fluence regimen.

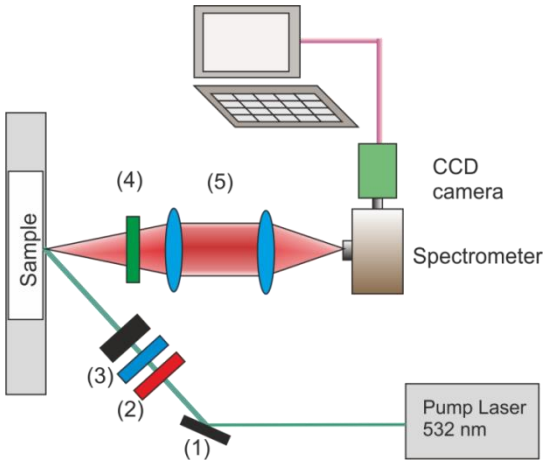

Figure 8. Schematic diagram of the time-resolved photoluminescence setup. The sample is placed in the sample holder and excited by the pump laser. In the diagram: (1) dichroic mirror, (2) UV filter, (3) neutral density (ND) filters, (4) Green laser filter, (5) Detection optics.

3.2.Transmission and Absorption

The UV-Vis spectrum is measured to observe the transmission (T) and absorption (A) of a material. Relative measurements allow additionally assessment of the influence that fabrication parameters have on the quality of the layer. In order to calculate the absorptance, Eq. (3.13) is used:

$$A = 100 - (R + T) \tag{3.13}$$

where A is the absorption, R is the reflection and T is the transmission of materials. Estimation of the absorption coefficient is calculated using the method described in Section 3.2.1.

3.2.1. Estimation of the absorption coefficient in thin-films

The absorption coefficient is an intrinsic property of a material, defined as the rate in which the photons are absorbed per unit length. However, when the layers are very thin (from the

nanometer to tens of micrometer range), as those used in thin-film SCs, the structural characteristics, morphology, and geometry of the layer play a larger role in the absorption. The absorption coefficient will then change depending on fabrication and coating techniques, and influence the response of the system to optical stimuli. Therefore, the challenge is to properly estimate the absorption coefficient, taking into account the characteristics of the system to provide an accurate description.

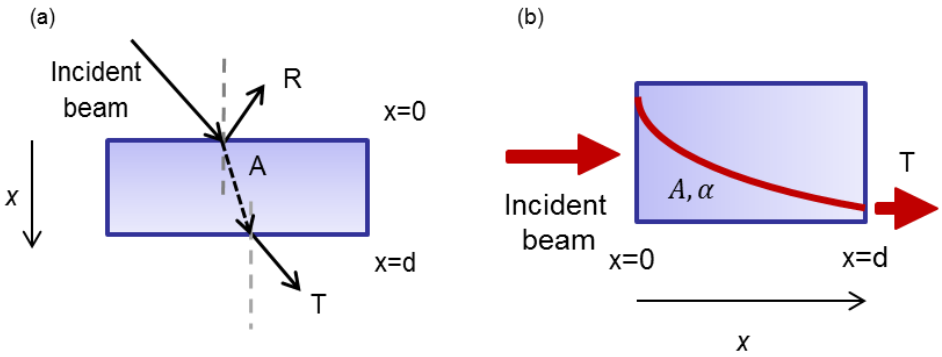

Figure 9. (a) Schematic diagram of the light beams as they pass through a single slab of material. (b) Absorption of the incident beam and how it affects the transmitted beam.

The classical approach derives the value for the absorption coefficient from the transmission and reflection measurements (Figure 9), normalized by the material thickness (Eq. (3.14)). Within the material, the intensity of the beam follows the Lambert-Beer law (Eq. (3.14)), as it decreases with the traveled distance and absorption coefficient. The transmitted beam can be estimated from the incident light intensity after reflection and the attenuation due to the material have been deducted, such that:

$$T = A * e^{(-\alpha * d_{material})}, \tag{3.14}$$

where α is the absorption coefficient and d is the thickness of the material. However, this derivation is valid only in the cases of one slab of material. When the absorption is calculated for a system where a thin layer is deposited over a substrate (*e.g.* an insulator) the classical approach fails to properly estimate the absorption coefficient.

The classical approach states two assumptions when a system of two finite layers is evaluated (Figure 10a). First, that the reflection of the system is due only to the first (top) layer (Eq. (3.15)), as it assumes that all internal reflections are absorbed and there is no influence of either the reflections at the interface or at the bottom of the substrate. Second, the transmission of the system is taken as a product of the transmission of the film and the transmission due to the substrate (Eq. (3.16)). From these assumptions, the absorption coefficient (α) of the film is estimated:

$$R_{film} \approx R_{tot} \tag{3.15}$$

$$T_{film} \approx \frac{T_{tot}}{T_{sub}} \tag{3.16}$$

$$\alpha_{film} = \frac{1}{d_{film}} \ln \frac{1 - R_{film}}{T_{film}} \tag{3.17}$$

From Eq. (3.17), the absorption coefficient of the film could be easily calculated from quantifiable data. And while this approach may be valid for architectures with layers of similar thickness, in the case of a thin film other considerations should be taken into account.

The conventional approach for the estimation of the absorption coefficient relies on two assumptions:

- the system to be studied presents a flat surface, and
- the reflections at the bottom interface are negligible, as mentioned above.

In the case of thin-film perovskite layer, such assumptions are not fulfilled. The perovskite film, when deposited from a solution, has good coverage of the substrate where they are deposited and presents a dark and shiny layer, indicators of a good reflection, but in the nanometer range, the film layer has a roughness of ~18 nm. Therefore estimation of the absorption coefficient that accounts for scattering is required.

Additional issues arise for the evaluation of thin films of a material deposited on a substrate: since the thickness of the material is thin, the internal morphology of the film comes into play, as well as the surface morphology. Also, the assumptions initially taken from the conventional approach have to be revised, as they no longer apply. The method to calculate the absorption coefficient of thin films deposited on a substrate (usually much thicker than the films) and to estimate it precisely is proposed by Cesaria [142].

For the description of the method, the system is defined in this section as the slab that contains the thin film and much thicker substrate (indicated by the suffix *sys* in Figure 10), not to be confused with either substrate measurements or by film estimations (indicated by suffix *sub* and *film*, respectively).

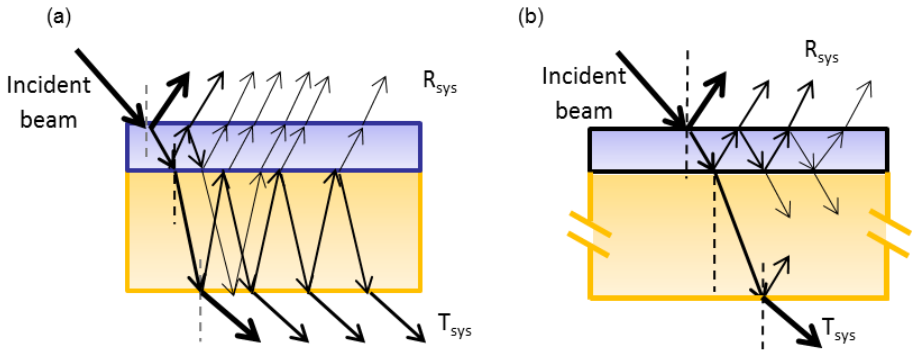

Figure 10. (a) Schematic diagram of the transmission and reflection beams for an architecture of a film-substrate system in a finite-thickness substrate (classical approach) and (b) with a semi-infinite substrate.

One of the revised assumptions is the measurement of the reflection upon the system. In the conventional approach, for a slab of material deposited on top of a substrate, the main component of the reflection beam comes directly from the top layer ($R_{sys} \approx R_{film}$). Other reflections (either of the interface with the substrate, or at the bottom of the system) are assumed to be negligible, based on a complete absorption of the reflected beams due to the thickness of both materials. On the other hand, when a thin film on a much thicker substrate is measured, this assumption is no longer correct. There is still an influence of the internal reflections at the film-substrate interface on the system reflectance.

The substrate itself is a semi-transparent material (*i.e.*, glass) with a thickness much larger than that of the film (Figure 10b). For films with hundreds of nanometer of thickness, a typical glass substrate of 1 mm is several orders of magnitude larger. In this system, the substrate can be assumed as semi-infinite, and the reflection beams generated at the bottom would not participate in the system´s reflection as they would be absorbed by the substrate on their path. The transmitted beams from the internal reflections would also not affect the total transmission of the system for the same reason, so the only component of the transmission of the system would be the (initial) transmitted incident beam.

When R_{sys} is measured, it contains the information regarding the reflection at the surface of the film, but also of the non-measurable influence of the interface film-substrate, as well as contributions of the interface formed by the perovskite film and the rear contact and additional scattering.

For the transmitted signal, Eq. (3.14) can be used to extract the transmission for the second slab. If we add the suffixes it can be written as:

$$\begin{aligned} T_{film} &= c * e^{(-\alpha_{film} * d_{film})} \\ T_{sub} &= c * e^{(-\alpha_{sub} * d_{sub})} \\ T_{sys} &= c * e^{(-\alpha_{sys} * d_{sys})} \end{aligned} \tag{3.18}$$

Where c is a value of the light entering the layer after reflection has been taken into account.

For a system with two layers, the beam transmitted to the substrate from the film is attenuated by a factor of $e^{-\alpha_{film} * d_{film}}$. In the same way, the total transmitted beam of the system would be dampened by a factor of $e^{-\alpha_{sub} * d_{sub}}$, such that

$$\begin{aligned} T_{sys} &= \left(1 - R_{sys}\right) * e^{(-\alpha_{film} * d_{film})} * e^{(-\alpha_{sub} * d_{sub})} \\ T_{sys} &= \left(1 - R_{sys}\right) * e^{(-\alpha_{film} * d_{film} - \alpha_{sub} * d_{sub})} \end{aligned} \tag{3.19}$$

and a relation between the absorption coefficient of the total system and that of each slab can be established

$$\alpha_{sys} * d_{sys} = -\alpha_{film} * d_{film} - \alpha_{sub} * d_{sub} \tag{3.20}$$

As the distance of the system is the sum of the thickness of each layer and the thickness of the film is much smaller than the thickness of the substrate, then Eq. (3.20) can be written as:

$$\begin{aligned} \alpha_{sys} * d_{sub}\left(1 + \frac{d_{film}}{d_{sub}}\right) &= -\alpha_{film} * d_{film} - \alpha_{sub} * d_{sub} \\ \alpha_{film} * d_{film} = \alpha_{sys} * d_{sub}\left(1 + \frac{d_{film}}{d_{sub}}\right) - \alpha_{sub} * d_{sub} &\approx \left(\alpha_{sys} - \alpha_{sub}\right) * d_{sub} \\ \alpha_{film} &= \frac{d_{sub}}{d_{film}}\left(\alpha_{sys} - \alpha_{sub}\right) \end{aligned} \tag{3.21}$$

where both α_{sys} and α_{sub} can be calculated from quantifiable data.

Following this method, the internal reflections at the back of the thin film will still influence the total reflectance of the system's reflectance. When evaluating thin films, reflection of the system is not only a reflection of the thin film itself but the sum of it and the internal reflections at the substrate/film interface, since the structural features of the film will have a stronger

contribution than in the case of a thick slab of material. Furthermore, beams reflected at the bottom or at the film-substrate interface are not neglected in the calculation. Therefore, this calculation is deemed realistic because it does not disregard the influences of the scattering from the internal interfaces and the film-volume interface [143].

The thickness of the thin film is assumed as uniform, but should it include a level of roughness, as it is in the case of perovskite layers. However, this method is still accurate in the estimation of the absorption coefficient as it takes into account the microstructural effects of the film[142]. Since this approach also includes the contribution of scattering, the non-uniform effects of changes in the film thickness are still taken into consideration, rendering this method valid for the perovskite layers here presented.

3.2.2. UV-Vis setup

The UV-Vis measurements are executed in air using a Lambda 1050 UV/VIS/NIR Spectrometer (PerkinElmer, Figure 11). The samples are illuminated with two lamps to have a broad range of the excitation spectrum: a deuterium lamp and a tungsten-halogen lamp. The wavelength range used for the measurements is 300-1200 nm. Unless otherwise stated, all samples are measured from the top side and in air.

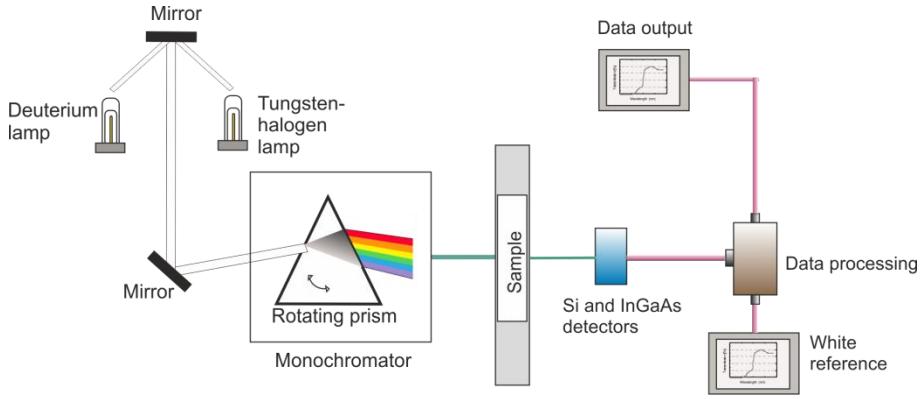

Figure 11. Schematic diagram of the UV-Vis setup.

3.3. *J-V* characterization

The measurement of the current-voltage characteristics of a solar cell under illumination is the tool that evaluates the electrical performance and quality of a completed solar cell or device on its implementation. In this measurement, the device is illuminated with a light source, simulating the light intensity and spectrum of the sun, while a voltage is applied to its terminals. An equivalent circuit for a solar cell can be found in Figure 12.

The current (I) extracted from the solar cell is the photo-generated current (I_L) minus the current consumed by the diode (I_D) and the shunt resistor (I_{SH}), so that:

$$I = I_L - I_D - I_{SH} \tag{3.22}$$

The electrical behavior can be rewritten in terms of the Shockley diode equation[144]:

$$I = I_L - I_o\left[e^{\frac{e*(V+IR_S)}{n*k_B*T}} - 1\right] - \frac{V + IR_S}{R_{SH}} \tag{3.23}$$

Where I_0 is the dark saturation current[3], e is the electron charge ($1.6\text{x}10^{-19}$ C), k_B is the Boltzmann constant ($1.38\text{x}10^{-23}$ m^2 kg s^{-2} K^{-1}), n is the diode ideality factor, V is the voltage, and R_S and R_{SH}, the series and shunt resistance, respectively[145].

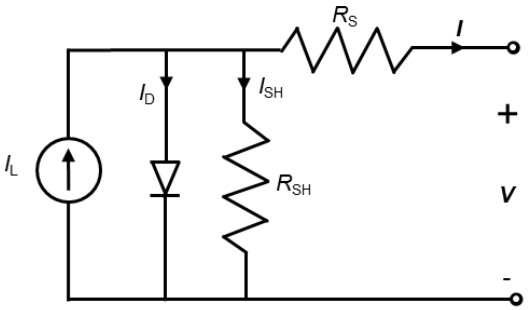

Figure 12. Equivalent circuit of a solar cell, including parasitic resistances.

However, for laboratory cells, the curve that is analyzed is the current density-voltage (*J-V*) characteristics, taking into account the small active area of each individual cell. From the *J-V* characteristic curve, several parameters can be extracted that reflect the devices' performance and limitations.

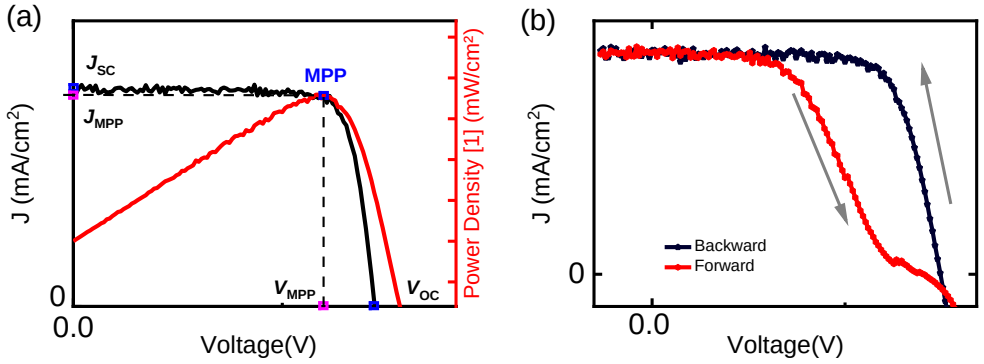

Figure 13. (a) *J-V* characteristics of a solar cell under illumination with important parameters shown on the plot. In red, the power extracted from the solar cell. (b) *J-V* characteristic curve of a solar cell with hysteresis, measured in backward and forward direction. In the plot: J_{SC} stands for short-circuit current density; J_{MPP}, for maximum power current density; V_{OC}, for open-circuit voltage; V_{MPP}, voltage at the maximum power point.

The open-circuit voltage (V_{OC}) [146], seen in Figure 13a at the intersection of the extracted current density and the x-axis, is the maximum voltage generated by the devices when no current is passing through the device. The short-circuit current density (J_{SC}), identifies the maximum extracted current density and it is set at the intersection of the extracted current density in the y-axis, where no voltage is applied to the device. The maximum power point (MPP) is the maximum of the power plot calculated from the *J-V* characteristic curve. The

[3] *i.e.* the current that flows through the diode in the dark under reverse bias

voltage at maximum power (V_{MPP}) and the current density at maximum power (J_{MPP}) are taken as the x and y- coordinates for the MPP.

The fill factor is a parameter that showcases the quality of the cell providing an estimation of how close to ideal the device performs. It is calculated from the ratio of the maximum power and the power calculated from V_{OC} and J_{SC} (Eq. (3.24)).

$$\mathrm{FF} = \frac{V_{MPP} * J_{MPP}}{V_{OC} * J_{SC}} \tag{3.24}$$

From these three parameters, and the incident light power, the power conversion efficiency (PCE) is calculated:

$$\mathrm{PCE} = \frac{V_{OC} * J_{SC} * FF}{\mathrm{P}_{in}} \tag{3.25}$$

where V_{OC} is the open-circuit voltage (in V), J_{SC} is the short-circuit current density (in mA/cm^2), FF the fill factor (adimensional) and P_{in} the incident power density.

Other criterions that are taken into consideration are the power conversion efficiency quotient (PCEq) and the hysteresis index (HI). PCEq is the ratio of the power conversion efficiency in backward and forward direction. The hysteresis index (HI) is the ratio of the area under the curve of the backward and forward direction. The main difference between the two parameters is that the first parameter takes into account only the variation of the maximum power point between the two measurements, while the second considers the entire data range.

These parameters have a strong relevance taking into account that perovskite SCs are known to show hysteresis in the *J-V* characteristic curve [147]. In other words, they present a deviation in the *J-V* curve when a measurement parameter is changed, like the measuring speed or the direction of measurement (whether it is done on the backward direction (V_{OC} to J_{SC}) or the forward direction (J_{SC} to V_{OC}) (Figure 13b). All devices described in this document are measured in both directions. The hysteresis is evaluated in two ways: with the PCEq and the hysteresis index (HI).

The sample is placed under illumination in a solar simulator for the evaluation of the power conversion efficiency. The solar simulator has a Xenon lamp calibrated at 1000 W/m^2 (AM 1.5G) with a certified Silicon solar cell (Newport) at 25 °C. The voltage is applied to the device with a Keithley Source Measure Unit (SMU). Each sample (16x16 mm) has 4 cells for statistical measurements of each parameter. The area of each individual cell is 10.5 mm^2. The speed of the measurement is kept at 600 mV/s.

The measurement of the samples is done through several cycles, to observe and record the light soaking effect, if present. Additionally the evaluation in time of the power conversion efficiency at constant voltage is measured to observe the stability of the devices. Between measurements the samples are stored in the dark inside a nitrogen glovebox to avoid degradation. In the cases of long term studies, silver ink is additionally used to cover the golden electrodes to prevent the breaking of the electrode contact points.

3.4. External Quantum Efficiency (EQE)

External quantum efficiency (EQE) is the measure of the charges extracted per incident photons at a given wavelength in a photovoltaic (PV) device. This measurement provides a spectral interpretation of the current extraction process and assists in the determination of the loss mechanisms that could be affecting the effective performance.

The photovoltaic devices are illuminated with a light source that simulates the solar spectrum and that has been previously calibrated with a certified silicon solar cell. The photo-generated current is measured, doing a spectral sweep of the incident light on the PV device. For the PSCs studied in this dissertation, with E_g ~1.6eV, the wavelength range used is 300-800 nm.

For the calculation of the EQE, the spectral response of the certified silicon solar cell is used as a reference to calculate the J_{SC} of the PSCs [148]. The equation used to calculate the external quantum efficiency is the following:

$$\mathrm{EQE}(\lambda) = \mathrm{EQE}^{ref}(\lambda)\frac{I_{ph}(\lambda)}{I_{ph}^{ref}(\lambda)} \tag{3.26}$$

where $I_{ph}(\lambda)$ and $I_{ph}^{ref}(\lambda)$ are the photocurrent flowing through the solar cell and the reference solar cell, respectively and $\mathrm{EQE}^{ref}(\lambda)$ is the known EQE of the certified silicon solar cell[149].

3.5. X-ray diffraction

X-ray diffraction is a characterization technique that uses X-ray radiation to extract information regarding the composition and crystalline structure of a material. When x-rays strike a sample of a crystalline material, the regular distribution of the atoms acts like a grid and diffracts the rays, as they are of the same order of magnitude. The scattered rays that are in phase achieve constructive interference and those that out of phase will suffer destructive interference.

The rays scattered in constructive interference are reinforced according to Bragg's law[150]:

$$2 * \mathrm{d_{hkl}} * \sin\theta = \mathrm{n} * \lambda \tag{3.27}$$

where d_{hkl} is the distance between the atomic planes; θ, the incident beam angle; n, the diffraction order (usually taken as 1 [20]) and λ, the X-ray wavelength. For X-ray diffraction, the condition described in Eq. (3.27) must be met.

For the evaluation of the x-ray diffraction presented in this dissertation, a Bruker D2 phaser, with Cu K_α radiation is used.

3.6. Transient absorption (TA)

Transient absorption is an optical characterization technique that measures the changes in the absorptance/transmittance of a sample after it has been illuminated (or probed). This technique uses two laser pulses: a pumping pulse and a probing light. The first excites the charges in the

sample, and the second is delayed to measure the changes of the transmission of the sample after it has been depleted.

3.7. Scanning electron microscopy (SEM)

Scanning electron microscopy (SEM) is a technique used for imaging at very high resolution (up to 10 nm). In order to obtain the images, the sample is bombarded with electrons that interact with the sample surface. This interaction releases charges and scattered electrons that are detected by the microscope and possess information on the morphology and the type of material at the surface of the sample. The SEM is used for scanning surfaces with a resolution in the nanometer scale and, that way; observe the morphology of the grains and layers.

3.8. Atomic force microscopy (AFM)

Atomic force microscopy (AFM) is a technique used to characterize the morphology of the layer, by measuring the atomic force between the probe and the sample. In this technique, a cantilever with a tip (or probe) is set on a piezoelectric support. The cantilever is swept across the sample, and the interactions between the tip and the sample surface will induce a force on the piezoelectric element, registering as changes in the mechanical pressure exerted by the cantilever. The probe is then scanned throughout the sample to obtain a mapping of the surface topography of the sample.

4. Fabrication methods

In this chapter, we describe the different deposition methods used in this dissertation and in the optimization of the devices.

In later chapters, the evaluation of the optical properties of perovskite thin-films will be examined comparing the influence of different fabrication methods in order to select the highest layer quality and device performance. In this chapter, the fabrication protocols are described for each method and layer.

4.1. Transport layer deposition

In this section, the method used to deposit the hole transport layer (HTL) and the electron transport layers (ETL) is described.

4.1.1. Spiro layer

SpiroMeOTAD (Spiro), used as HTL in the devices, is spin-coated over the perovskite layer from solution. The Spiro solution is prepared by dissolving 2,2,7,7-tetrakis-(N,N-di-p-methoxyphenylamine)-9,9-spirobifluorene (Lumtec) in a chlorobenzene (CB), 4-tert-butylpyridine (4tBP, Sigma Aldrich) and lithium salt solution. The lithium salt solution is prepared from bis (trifluoromethane) sulfonimide lithium salt (Li-salt, Sigma Aldrich) in acetonitrile (Table 1). The solution is warmed at 60 °C for 10 min after mixing the solvents and then left to cool down.

Spiro Solution	**160 mg Spiro**	**2010 µL CB**	**57.3 µL 4tBP**	**35.2 µL Li-salt solution**
Lithium salt solution	104.308 mg Li-salt	200 µL ACN		

Table 1. Parameters for the Spiro and the Lithium salt solution used.

After perovskite deposition and before spin-coating the Spiro layer, it is important to ensure that the samples are completely cooled down (~45 min). This is both for heat dissipation (in the samples) and for solvent extraction (from the glovebox).

For the deposition of the Spiro layer, 35 µL of the Spiro solution are used per sample (substrate area 16x16 mm) and the droplet is dragged throughout the surface before initiating the spin-coating cycle (slow dispense technique, Table 3). In order to finish the layer, the substrates are placed in a dry box for a period of ~16 h (23 % RH in air at room temperature) for oxygen doping.

4.1.2. SnO_2 layer

SnO_2 used as ETL is spin-coated over the ITO substrates from solution. The SnO_2 precursor solution is prepared from tin (IV) chloride pentahydrate (98%, Sigma Aldrich), dissolved in anhydrous isopropanol (IPA) in a concentration of 28 mg/ml [18] (weighted in air at 25 % and 30 % RH, inside the cleanroom). The SnO_2 precursor is weighted in air and the solvent added in nitrogen glovebox environment. Afterward, the vial is stirred to achieve a full dissolution of the solid precursors. For the deposition of each SnO_2 layer, 30 µL of this solution per sample are used, using a fast dispense spin-coating technique [151]. After spin-coating, the sample is placed on a hotplate for solvent evaporation and later annealed in air for the formation of a compact SnO_2 layer. The samples are kept in a nitrogen atmosphere between depositions.

Heating the samples with SnO_2 at 100 °C inside a glovebox is implemented as well, to extract any residual moisture content from the layers. However, devices built with this additional step presented lower power conversion efficiency in the *J-V* characteristic curve.

4.1.3. TiO_2 layer

Titanium dioxide (titania, TiO_2), used as ETL is prepared from a titanium dioxide precursor solution. The solution is prepared with titanium diisopropoxide bis(acetylacetonate) (TAA) dissolved in absolute ethanol in a 1:39 ratio[152]. The TiO_2 solution is spin-coated for 30 s at a 3000 rpm and the solvent evaporated in air for 10 min at 100 °C. The TiO_2 solution is deposited three times for each substrate. The TiO_2 compact layer is annealed (at 500 °C for 1 h in air) to allow electron conduction [30].

4.1.4. C_{60} layer

In chapter 6, an evaluation of the interfaces as a source of hysteresis is executed and a passivating layer (or interlayer) made of C_{60} fullerene (hereafter referred to as C_{60} or fullerene) is used to further these studies. In chapter 7, C_{60} is used as ETL to evaluate degradation mechanisms in the PSCs. Deposition of solution-processed C_{60} on top of hygroscopic surface such as SnO_2 and a posterior deposition of perovskite layer are a challenge, due to the conflicting wettability of the surfaces.

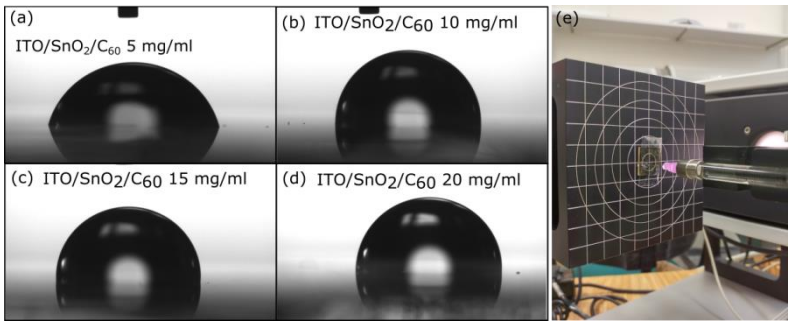

Figure 14. (a-d) Water droplet deposited on C_{60} layers for measurement of the static contact angle. (e) Attempt to measure the roll-off angle on C_{60} samples.

Therefore, before a complete implementation of a solution-processed C_{60} layer is achieved, the method for the fabrication of the C_{60} layer is optimized: variations of the substrate temperature and of the solution temperature, as well as optimization of the annealing treatment and deposition technique, are executed. The highest quality of the layer is found to be deposited by using slow dropping of the C_{60} solution before spin-coating, that is, executing a static (slow) dispense of the solution [151]. This technique was implemented upon measuring the water droplet contact angle on the C_{60} layers. With increasing the C_{60} concentration, the hydrophobicity increased until it reached a plateau (with a contact angle ~90 °). Measurement of the roll-off angles was also attempted but none was found. The slow dispense technique suits the deposition on the hydrophilic SnO_2 layers because it relies on the adhesion of the solution to the substrate. In the case of the C_{60} layer, the strong adhesion ensured the formation on a fully covered layer upon spin-coating[4] (Figure 14).

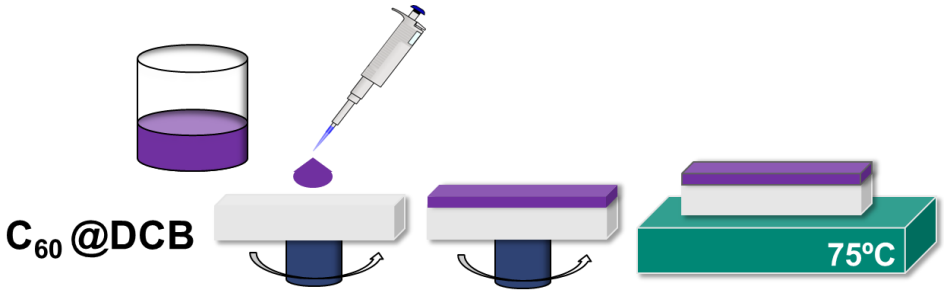

Figure 15. Schematic diagram of the deposition of the C_{60} layer via spin-coating.

C_{60} layers are deposited via solution processed spin-coating to maintain vacuum-free deposition throughout the active layers. C_{60} (Fullerene powder, sublimed, 99.9+%C_{60}, AlfaAesar) is dissolved in 1, 2-dichlorobenzene (DCB) and magnetically stirred overnight. For a systematic determination of the best concentration range for the C_{60} solution, steps of 2.5 mg/ml ranging from 2-20 mg/ml are evaluated. Higher concentrations than 20 mg/ml are not used to avoid reaching the solubility of C_{60} in DCB (~27 mg/ml, [153]). For each sample, 35 µL of the C_{60} solution is used. Before C_{60} deposition, the samples are set in the plasma oven for 1 min at 30 % in O_2. The C_{60} solution is deposited on the sample area and dragged throughout the entire sample before spin-coating. After spin-coating, the substrates are annealed on a hot plate for drying the solvent.

Samples with evaporated C_{60} are also implemented in order to compare performance. C_{60} layers (5-15 nm) are deposited via thermal evaporation (Model: Spectros, Kurt J. Lesker) under high vacuum (10^{-6} mbar) for comparing the validity of the solution process method.

4.2. Perovskite layer fabrication

As mentioned before, one of the advantages of using perovskites for SCs is that this group of materials allows a broad range of fabrication methods. From solutions, perovskites can be spin-coated [154]–[156], blade-coated [44], [157], inkjet-printed [158], [159] or dipped [83], [160];

[4] The contact angle images are taken by Aiman Roslizar.

from powders, they can be evaporated individually [161] or from dual sources for homogeneous morphology of the resulting perovskite layers [85], [162].

The same advantage can become one of the challenges as there are many approaches for the fabrication of organo-metal halide (OMH) perovskites. In that case, it is important to evaluate and optimize the fabrication method that offers the most advantages. There are several methods used and part of the optimization process involves, not only getting the highest quality of layer (which can be interpreted as better coverage, larger grain size, and homogeneity of the layers) but also, the morphology that ensures best electrical performance.

A preferred method of solution-processed perovskite fabrication is the spin-coating of perovskite solutions, followed by an annealing process. Advantages involve the scalability of the fabrication method along with the compatibility of this technology with pre-existing processing methods as well as the possibility of using it as a top cell in tandem with CIGS or c-Si [163]. One of the disadvantages is that during spin-coating, the resulting perovskite layer can be irregular and present uncovered regions, especially when it is compared to the layers fabricated from dual-source thermal evaporation, typically planar and uniform. In this dissertation, the focus is on the solution-processed fabrication of perovskite layers as our goal is the scalability of the fabrication methods.

4.2.1. One-step lead iodide

The perovskite layer fabrication described in this section is used in the layers studied in Chapter 5.

MAPI (or $MAPbI_3$, methylammonium lead triiodide) is the first type of perovskites used for solar cells. To form the MAPI layers, the one-step process with a solvent-engineering step is implemented. The perovskite precursors: lead iodide (PbI_2, Sigma Aldrich) and methylammonium iodide (MAI, Lumtec) are dissolved (MAI:PbI_2 in 1:1 ratio) in a molar concentration of 1.4M $MAPbI_3$ in a solvent mixture. For this deposition, the solvents are γ-butyrolactone (GBL, Sigma Aldrich) and dimethylsulfoxide (DMSO, Sigma Aldrich) used in a 7:3 ratio [158], [164]. Furthermore, a solvent-engineering step is also implemented using toluene during spin-coating of the perovskite solution, schematized in Figure 16.

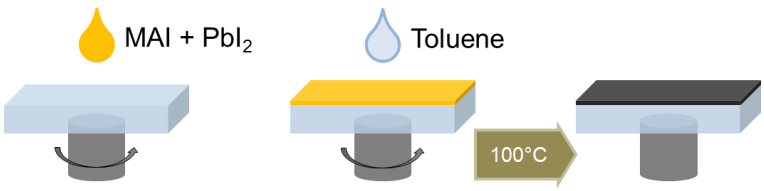

Figure 16. Schematic diagram of the deposition of perovskite with the one-step solvent-engineering (toluene) process.

The perovskite solution is left in the hotplate at 65 °C until the solid content is completely dissolved (c.a. 15 min). The substrates are cleaned with isopropanol and acetone followed by plasma etching. The TiO_2 ETL is deposited using the method described in the previous section. The warm substrate is placed in the spin-coater and 25 μL of the perovskite solution is deposited with a fast-dispense method for the spinning cycle (1000 rpm for 13 s, followed by

5000 rpm for 25 s, Figure 16). Between the spin-coating cycles, 1 µL of toluene is deposited on the layer[165], [166]. After the spinning cycle is finished, the substrates are placed again in a hotplate at 100°C for 10 min under nitrogen flow, before they are left to cool down in air. The perovskite layers produced using this method will be addressed as MAPI (or MAPbI).

4.2.2. Lead acetate process

The perovskite layer fabrication described in this section is used in the layers studied in Chapter 5.

In order to improve efficiency and layer quality, the one-step lead acetate process is implemented. In the perovskite solution, MAI is used alongside lead diacetate trihydrate (PbAc, Pb $(CH_3CO_2)_2{\cdot}3H_2O$)) as the lead precursors [156]. The solid content is dissolved in dimethylformamide (DMF, Sigma Aldrich). Moreover, the solvent-engineering step is implemented in the perovskite solution by adding hypophosphorous acid (HPA, Sigma Aldrich [167]) (Figure 17).

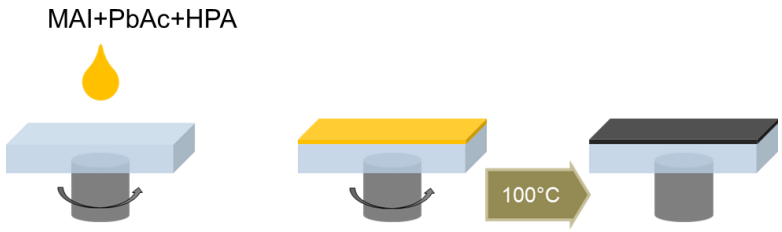

Figure 17. Schematic diagram of the deposition of perovskite with lead acetate process

Mixed halide perovskites are also implemented, using the lead acetate process and adding lead chloride ($PbCl_2$, Sigma Aldrich) to the perovskite solution. Perovskite layers with $PbCl_2$ [41], [57], [129], [168]–[170] as a precursor do not show a bandgap shift (as is seen with the usage of lead bromide [171]) but show a slower crystallization rate, resulting in an improvement of the layer quality and of the electrical properties [61], while maintaining optical properties. In earlier communications on the topic, perovskite thus fabricated are called mixed halides [172], [173], but x-ray diffraction (XRD) measurements executed on the samples indicate that the presence of chloride is acting as a scaffold that is evaporated during post-deposition thermal treatment (or annealing). In this dissertation, the perovskite deposited from lead chloride precursors will be noted as $MAPbI_{3-x}Cl_x$, even though the crystalline distribution is that of methylammonium lead triiodide, to differentiate it from precursors with only lead iodide as the lead base.

4.2.3. Optimized lead acetate method

The perovskite layer fabrication described in this section is used in the layers studied in Chapter 5, and devices studied in Chapter 6 and 7.

In the optimized lead acetate method, the perovskite solution is prepared for two precursor solutions: the first solution uses lead diacetate trihydrate (PbAc, Pb $(CH_3CO_2)_2{\cdot}3H_2O$, Sigma

Aldrich) and methylammonium iodide (MAI, Lumtec) dissolved in dimethylformamide (DMF, Sigma Aldrich); the second, lead (II) chloride ($PbCl_2$, Sigma Aldrich) and MAI dissolved in DMF. The weight and volume used for each chemical can be found in Table 2. The two solutions are stirred overnight with a magnetic stirrer and 360 µL of the $PbCl_2$ solution is added to the PbAc solution before using (Table 2). Before perovskite deposition, the samples are set in the plasma oven for 1 min at 30 % in O_2. If the samples have a C_{60} layer, this step is skipped since the plasma treatment destroys the C_{60} layer. For each perovskite layer, 40 µL of the perovskite solution is used to ensure coverage of the substrates.

PbAc solution	455.2 mg PbAc	572.0 mg MAI	1140 µL DMF
$PbCl_2$ solution	89.4 mg $PbCl_2$	152.1 mg MAI	400 µL DMF

Table 2. Parameters for the perovskite solutions used in the optimized lead acetate method.

The deposition technique for the lead acetate method is optimized for the implementation of hydrophobic substrates (namely C_{60} layers, further discussions in Chapter 6 and 7). C_{60}, used as interlayer and as ETL in Chapters 6 and 7, forms layers that reduce the wettability of the perovskite solution. The decrease in wettability resulted in a lack of coverage upon deposition of the perovskite solution since most of it would be swept away from the substrate when the spin-coating cycle is started (Figure 18b). This resulted in incomplete coverage and the loss of a high percentage of the fabricated devices. It is often suggested that the hydrophobicity of the C_{60} surface hampers the formation of high-quality perovskite films (Figure 18, [174], [175]) and therefore, thermally evaporated C_{60} has been widely used both in n-i-p [126], [174], [176] and p-i-n [87], [125], [177]–[180] architectures to ensure full coverage, often followed by the evaporation of the perovskite layer [181]. In p-i-n architecture, the C_{60} layer is deposited on top of phenyl-C_{61}-butyric acid methyl ester (PCBM)/perovskite layers and thus, the lack of wettability would not interfere in the formation of the perovskite layer. However, vacuum-based fabrication methods are difficult for the large-scale implementations of PSCs. Solution-processed fabrication methods are, on the other hand, easily scalable and cheaper to implement at larger scales. Therefore a method is devised to implement high-quality perovskite layers on hydrophobic substrates.

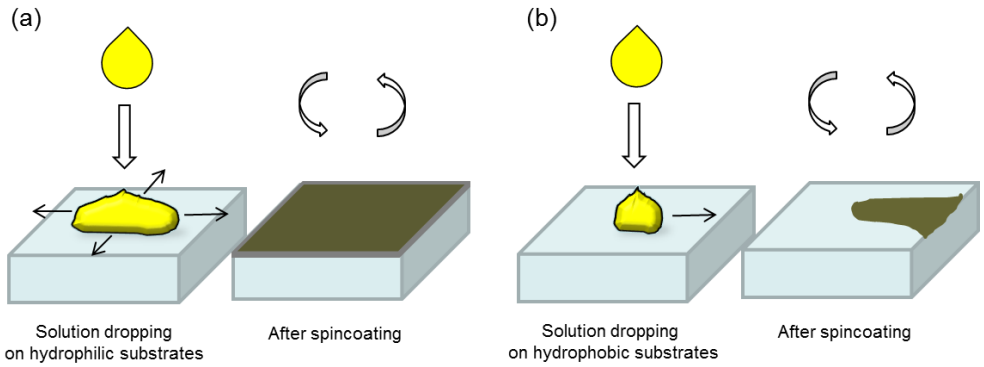

Figure 18. Wettability issues in the perovskite layers due to the hydrophobic substrates (a) fast dispense on hydrophilic substrates (*e.g.* SnO_2). (b). fast dispense on hydrophobic substrates

In the literature, it is acknowledged that control of the perovskite crystallization rate is very important for high-quality layer [156], [182] and many authors recommend a fast dispense technique for the deposition of the perovskite solution, either by spin-coating the perovskite

solution on an already spinning substrate or by using a solvent to slow down the crystallization [165], [166]. This technique, when implemented on hydrophilic substrates such as SnO_2, guarantees a fully covered substrate with homogeneous layers (Figure 18a). However, using a fast dispense deposition technique on hydrophobic substrate reduces the area covered by the perovskite solution and the final layers do not cover the substrate and are often inhomogeneous (a schematic is shown in Figure 18b; photo of the layers, in Figure 20a).

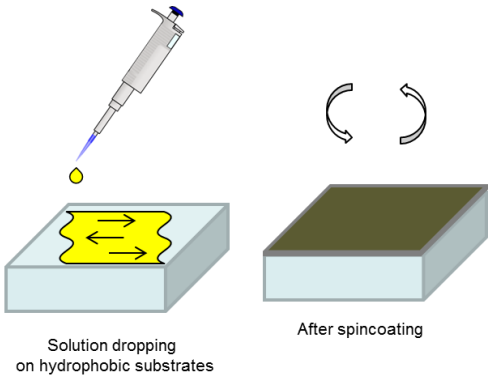

Figure 19. Schematic diagram of the slow dispense deposition of the perovskite solution on hydrophobic substrates.

Good coverage of the substrate is achieved by using the strong adhesion of the C_{60} layer (Section 4.1.4). Even though C_{60} performs as a hydrophobic surface (water droplet contact angle measured is 90° for concentrations of 10-20 mg/ml, in Figure 14), the adhesion of the water droplet indicates that once the surface coverage (by the solution) is ensured, a layer will be formed. A slow dispense technique for the deposition of the perovskite solution is thus implemented (Figure 19): the perovskite solution is placed on the substrate and dragged throughout the entire sample area before initiating the spin-coating cycle. This ensures that the solution covers the entirety of the substrate and upon spin-coating; a fully covered homogeneous layer is achieved (Figure 20b).

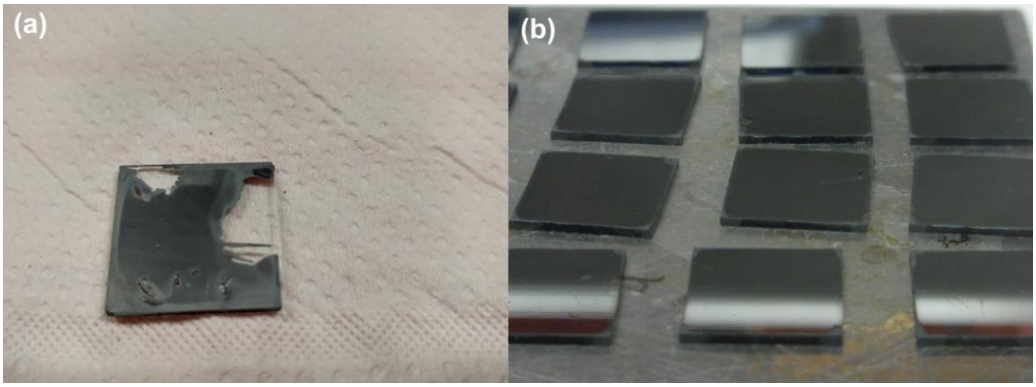

Figure 20. (a) Perovskite layers deposited on C_{60} layers using fast solution dropping. (b) Perovskite layers deposited on C_{60} layers using slow solution dropping.

The perovskite solution is placed on the substrate and dragged throughout the entire sample area before initiating the spin-coating cycle, ensuring that the entire surface is covered by the perovskite solution, before initiating the spin-coating cycle. After the spin-coating cycle, the samples are set aside for a waiting period, after which they are annealed. They are left to cool

down completely before Spiro deposition (a period longer than an hour provided the best results).

With the method here described, the strong adhesion of the C_{60} surface, described in Section 4.1.4, is contributing to the perovskite layer formation, by facilitating the attachment of the perovskite solution to the substrate. During spin-coating, the layer becomes homogeneous and control over the crystallization rate is achieved by keeping the samples 10-15 min at room temperature after spin-coating and before the annealing process.

The timeframe between the slow dispense and the start of the spin-coating cycle may be enough for the perovskite layer to start growing on the C_{60} substrate, and thus, the C_{60} layer below is maintained (not be driven away before perovskite crystallization). Evidence of C_{60} layer still being present in the architecture are quenching of the PL amplitude and lifetime, change of the transmission interference peak due to the different C_{60} thickness used in the range, among others (discussed further in Chapter 6).

4.3. Optimization of the solar cell architecture

The solar cell fabrication described in this section is used in the devices studied in Chapter 6 and 7.

ITO substrates are cleaned with glass cleaning detergent and cut into 16x16 mm samples, then labeled and sonicated with acetone for 10 min, dried with nitrogen gun, then sonicated with isopropanol anhydrous for 10 min and dried upon extraction. They are placed in a plasma oven with O_2 for 3 min at maximum power before the deposition of the SnO_2 layer. The spin-coating parameters and post-deposition treatment used for SnO_2, C_{60}, perovskite[5], and SpiroMeoTAD are indicated in Table 3.

	Concentration	Solvent	Spin-coating	Post-annealing
SnO_2	28 mg/mL	Isopropanol anhydrous (IPA)	1500 rpm, 30 s, 1000 ramp	Drying: 100 °C, 10 min (Nitrogen) Annealing: 180 °C, 1 h (air)
C_{60}	2, 5, 7.5, 10, 12.5, 15, 20 mg/mL	1,2-dichloro-benzene (DCB)	150 rpm, 60 s, 1500 ramp	75 °C, 5 min
SpiroMeOTAD			4000 rpm, 30 s, 1000 ramp	NA, oxygen doping overnight
$MAPbI_{3-x}Cl_x$		Dimethyl-formamide (DMF)	3000 rpm, 30 s, 1000 ramp	Waiting: 15 min Annealing: 115°C for 10 min, leave to cool down before Spiro.

Table 3. Spin-coating parameters for the layers in the devices for the optimized method.

[5] Using the optimized lead acetate method

Before the gold electrode is evaporated on the substrates, the samples are swiped with different solvents to ensure contact of the evaporated electrode to the ITO. GBL is used to remove the perovskite layer and IPA is used to remove traces of GBL, followed by a clean swipe for removing excess solvents. Nitrogen is also used to ensure all solvents are dried from the substrates before electrode evaporation. Special care should be taken when using the IPA as it can damage the C_{60} layer (seen as cracks in the perovskite layer).

The gold electrodes are evaporated on the samples at room temperature using a BellJar evaporating chamber to obtain 60 nm-thick Au layers. In order to protect the electrode from scratches, silver ink is used to ensure the contacts remain after several measurements.

5. Optimization of the fabrication method via optical characterization

In this chapter, I consider three solution-processed methods for the fabrication of the perovskite layer and we compare the results of the optical characterization to determine which offers the best layer quality. In order to do this, characterization of the optical properties is executed on perovskite layers fabricated with different methods. Thus, the influence of the varying fabrication parameters on the layer characteristics such as defect density but also the optical properties like the absorption coefficient can be estimated.

Furthermore, the light soaking (LS) effect in perovskites is described and studied through steady-state and time-resolved photoluminescence. Upon light soaking, the lifetime in the perovskite shows an increase, which may be related to photoactive traps filling. The variations in the recombination rate k are estimated in a variable to quantify the LS effect, Δk. This variable is defined for the different fabrication methods to compare the quality of the resulting layer made with each method. From there, we optimize and define the method that will be defined as a reference for chapters 6 and 7.

Perovskite solar cells (PSCs) use thin perovskite layers, in the nanometer range (also called thin-films), to absorb sunlight and convert it to electricity. The challenges of the implementation of such thin-films include the dependence of the macroscopic characteristics of the perovskite on the layer morphology and on the fabrication parameters. Therefore it is relevant to evaluate the influence of the fabrication method and parameters on the effective layer quality and optical properties.

In order to determine how steps from a deposition method or how different methods of deposition affect the quality of the final perovskite layer, samples with perovskite layers prepared with different deposition methods are studied to determine the influence in the final optical characteristics of the perovskite layers.

5.1. Evaluation of one-step lead iodine process

The first perovskite fabrication methods for solar cells use the one-step lead iodide method [74], [135][6]. This method consists of spin-coating the perovskite layer from a single precursor solution, followed by a thermal annealing. The perovskite solution is fabricated for two precursor materials: methylammonium iodide (MAI) and lead iodide (PbI_2) dissolved in dimethylsulfoxide (DMSO). The one-step lead iodide process facilitates the implementation of

[6] The layer deposition using this method was executed by Dr. Aina Quintilla.

the perovskite layer due to its simplicity but the quality of the layers formed with this method is not very high. From the optical point of view, it presents both pinholes reducing the amount of perovskite material absorbing the light. Besides this, there are imperfections in the crystal, which present nonradiative recombination centers, trapping the photogenerated charges. In Figure 21a, layers manufactured with the one-step lead iodide method show a white haze throughout the surface, evidence of pinholes in the layer.

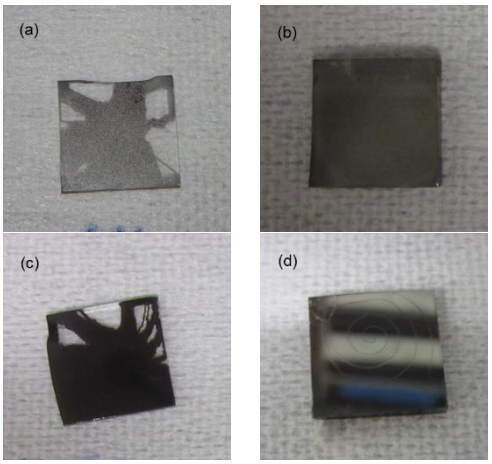

Figure 21. $MAPbI_3$ layers fabricated with the one-step lead iodide method (a) on glass and (b) on FTO/TiO_2 and using the toluene solvent-engineering step (c) on glass, (d) on FTO/TiO_2, with visible scratches from the toluene drop.

In order to improve the crystallization of the perovskite layer, the solvent-engineering step was proposed [165]. The solvent-engineering step consists of the addition of a solvent to induce the crystallization in the forming crystal layer[183] so that imperfections that may form during the rapid crystallization process are reduced. Solvent-engineering aims to control the speed of the perovskite layer formation being able to slow down the process, which starts upon first contact of the perovskite solution on the substrate. The addition of solvent during spin-coating helps to induce crystallization and improve the coverage of the layer [166]. Additionally, it is proposed that the presence of toluene expels residues from the solvent of the perovskite solution [184]. Different solvents are used in the solvent-engineering step to improve the perovskite layer: toluene [185], diethyl ether [186], isopropanol ([87] and anhydrous chlorobenzene [187], among others. In this section I address the usage of toluene dropping as solvent-engineering step.

The optical characteristics of the perovskite layer fabricated with and without the toluene dropping (solvent-engineering) step are analyzed. The photoluminescence (PL) spectra and time-resolved PL (trPL) of the perovskite layer on glass is evaluated to assess the perovskite layer quality and optical properties (Figure 22a and b). By implementing the solvent-engineering step during the perovskite deposition, the layer appears to the eye to have better quality, with the white haze no longer visible and presenting a homogeneous layer. The higher layer quality is evidenced in the increase of the PL of the perovskite layer on glass. Moreover, the lifetime is extended. The absorptance is increased as well compared to the layer deposited without toluene dropping, given the better coverage and lack of pinholes (Figure 22c). Estimation of the absorption coefficient using the Cesaria method [142], described in Section 3.1.2, corroborates that the absorption coefficient (α) is increased in the perovskite layers with the toluene step: it increases from an absorption coefficient of 0.69 $x10^5$ cm^{-1} in the layer deposited using the one-step lead iodide method to an absorption coefficient of 4.7 x 10^5 cm^{-1} in

the layer with the toluene step (Figure 22d)[7]. Furthermore, the calculated (effective) diffusion coefficient using the trPL measurements for the one-step process was $0.87x10^{-2}$ cm^2/s for electrons, and 1.53×10^{-2} cm^2/s for the toluene process, indicating a change in the diffusion length from 89 nm to 117 nm[8].

This increase can only be an indication of the reduction in the layer pinhole density. The PL measurements indicate that the addition of the toluene solvent-engineering step is reducing the transmission by improving the perovskite layer coverage, and increasing the charge carrier lifetime by reducing the recombination centers.

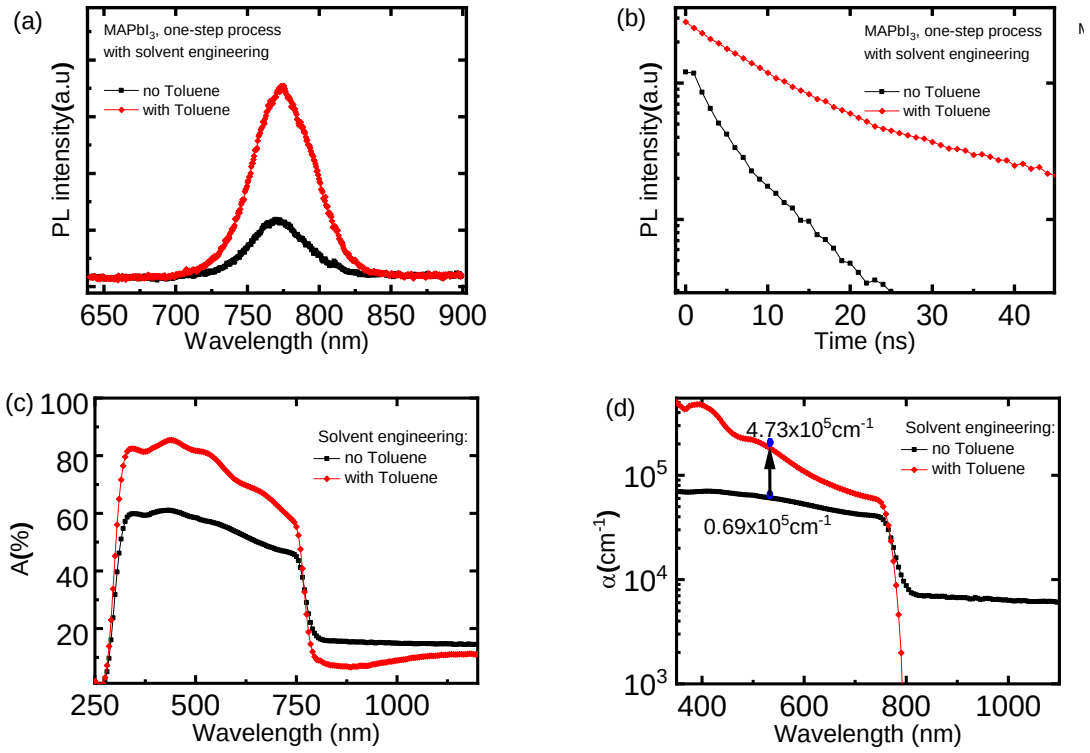

Figure 22. Perovskite layer fabricated with the lead iodide method, with and without solvent-engineering step (toluene), (a) Absorptance, (b) Absorption coefficient.

Adding the solvent-engineering step improves the quality of the perovskite layer. This improvement can be corroborated from the optical characterization where it is observed that the absorptance and the PL emission are increased. Even though the changes in the absorptance can be related to a reduction of pinholes in the layer, the increase of the absorption coefficient and the charge carrier lifetime indicate an improvement in the quality and optical properties of the layer fabricated with the solvent engineering step.

In Figure 23, a scheme is presented with the differences in the perovskite layers prepared with this method: Samples prepared with the one-step lead iodide method have a higher number of pinholes, reducing the total absorbed light. Furthermore, the low lifetimes (3 ns) indicate high

[7] The absorption coefficient here indicated is the estimated at 532 nm. This wavelength was used to excite charge carriers in the photoluminescence measurements

8 The diffusion coefficient is a property of the material and as such it is not sensible to changes in the macrostructure. However, the modifications in the fabrication method imply a change in the quality of the layer and its contact with the (electron) quencher. Therefore, it is an effective value, not an absolute one.

influence of recombination centers in the charge carrier dynamics within the perovskite layers. Samples prepared with the toluene process, show an improved absorption given by the better coverage and reduced number of pinholes, with lifetimes larger than in samples without the solvent-engineering step but still remaining at low values (~6 ns, compared to those obtained in the literature ~100 ns [168], [188]). Moreover, a challenge presented by the use of the solvent-engineering step is the application of the toluene drop to the layers, because it can introduce scratches in the layer during toluene dropping, rendering the method very unreliable. (Figure 21d). It is necessary then to improve the fabrication process to reduce recombination centers and increase reliability to the perovskite fabrication method.

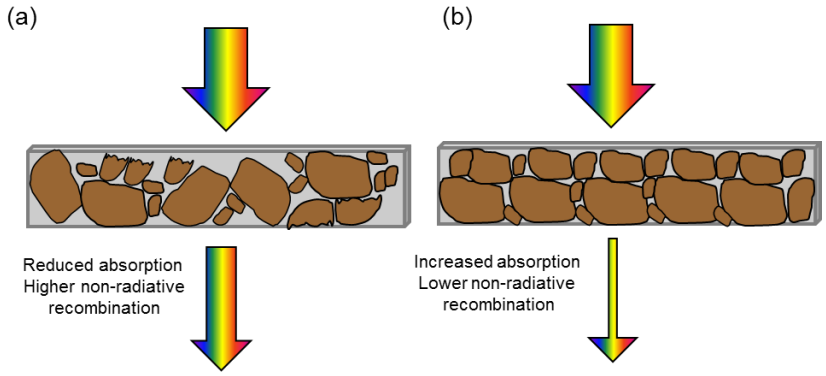

Figure 23. Schematic diagram of the perovskite layer quality in the: (a) one-step lead iodide process (b) one step process with the solvent engineering (toluene) step.

The reduction of the recombination centers in the perovskite layer will not only improve the charge carrier dynamics but also improve the power conversion efficiency of the solar cells fabricated with such layers. Perovskite solar cells fabricated with the toluene solvent-engineering method performed with a power conversion efficiency of 12% (backward direction), compared to the 6.5-7.4 % PCE of solar cells fabricated without the solvent-engineering step, with unstable performance and a large percentage of devices lost due to the unreliability of this method.

5.2. Evaluation of the lead acetate method

In order to remove the solvent-engineering step that introduced uncertainty during device fabrication, another method was evaluated, changing the lead precursor. The lead acetate method replaces the lead iodide within the perovskite precursor materials for lead acetate[9] (lead diacetate trihydrate, PbAc, Pb $(CH_3CO_2)_2 \cdot 3H_2O$) [156], to improve coverage and layer morphology. In the perovskite solution, the lead acetate is combined with MAI in dimethylformamide (DMF). Moreover, hypophosphorous acid (HPA) [189] is added to the perovskite solution to improve the perovskite layer optoelectrical properties, via crystallization enhancement[10]. During the spin-coating process and posterior annealing, the acetate anion evaporates and then the perovskite crystal maintains its $MAPbI_3$ structure [156].

[9] The layer deposition was executed by Tobias Abzieher and Florian Holley.

[10] This step is an equivalent to the toluene solvent-engineering step from the previous section, with the added benefit of removing the uncertainty created by dropping the solvent during spin-coating.

In Figure 24, the steady-state (a) and time-resolved (b) PL of layers deposited with the lead acetate method and further evaluation of the HPA solvent-engineering step is shown. The comparison then provided information on the crystallization of the perovskite layer. It can be observed that the PL signal is increased for the 2.5 and 7.5 µL/mL concentrations of HPA. There is, however, an unpredicted red-shift in the PL center for the sample with HPA in comparison to the perovskite layer deposited with the lead acetate process and a broadening of the PL spectra indicating a stronger presence of traps close to the bandgap. Moreover, the range of lifetimes is also low compared to those in the literature (~13 ns compared to ~100 ns [190], [191]). Therefore another approach is necessary.

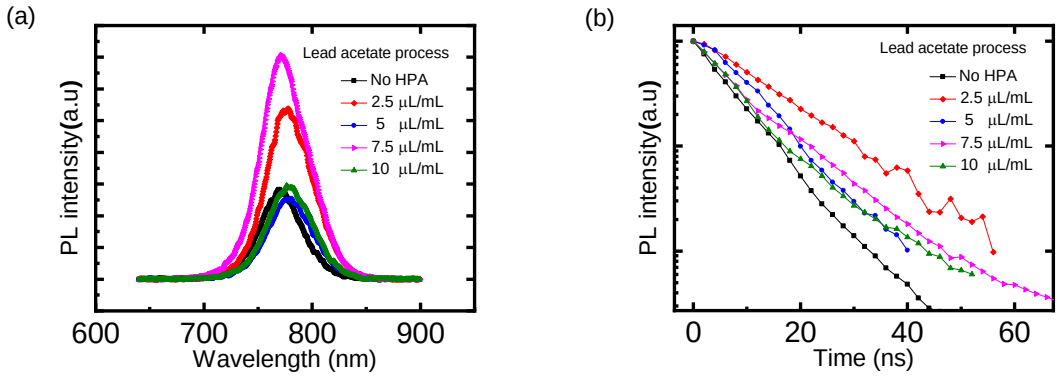

Figure 24. Steady-state and time-resolved PL for reference device under different fluences

Further optimization of the lead acetate process includes the variation of the solid content percentage in the perovskite solution (indicated as weight percent in Figure 25). The thickness of the perovskite layers is controlled through different solid content percentages. From the studied range, the solid content showing the best optical properties is for 40-50 wt.% of PbAc in DMF.

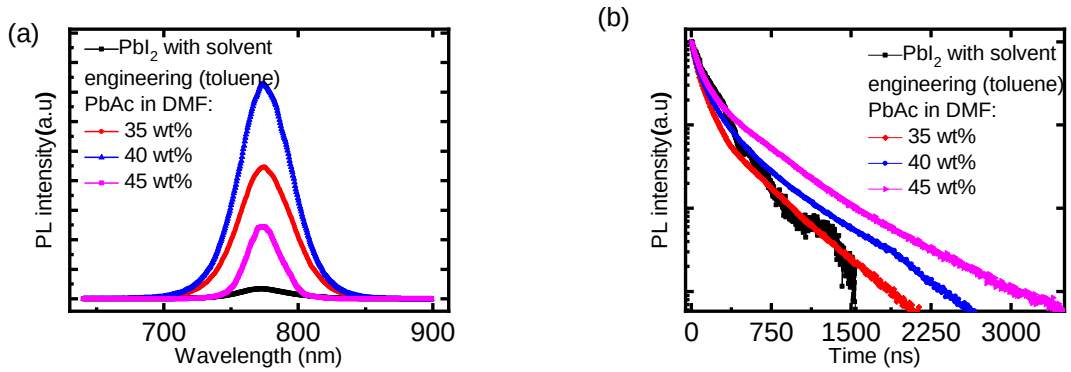

Figure 25. Steady-state and time-resolved PL of lead acetate process on glass, with different solid concentration of the precursor powders in the solvent, compared to perovskite layers deposited from the one-step lead iodide (with solvent engineering step).

5.2.1. Mixed halide lead acetate process

In organo metal-halide perovskites, the halogen component can be iodine, bromine or chlorine. Bromide-based perovskites emit in the 500-550 nm range ([192]) making them not suitable for solar cells on their own. $CH_3NH_3PbCl_3$ perovskites (methylammonium lead trichloride [193])

are used as ultraviolet detectors due to the strong responsivity in the UV and emission in the 400-430 nm range. $CH_3NH_3PbI_3$ or MAPI is the perovskite most often used for PSCs since it has an emission in the 750-800 nm range with a bandgap of 1.61 eV. Nevertheless, in order to improve the perovskite layer, mixed-halide perovskites are often used. With the addition of lead bromide ($PbBr_2$) to the perovskite solution, the perovskite bandgap shows a blue-shift with increasing $PbBr_2$ percentage and as such, it is often used to tune the bandgap of perovskite layer[192]. Lead chloride ($PbCl_2$) is also used in PSCs to stabilize the perovskite crystal [61], [194], [195]. The chloride ion modifies the perovskite crystallization rate, facilitating the formation of a higher quality layer [64], [194], improving the transport properties, without modifying the bandgap. In this section, the perovskite solution was prepared using lead acetate and lead chloride in small percentages.

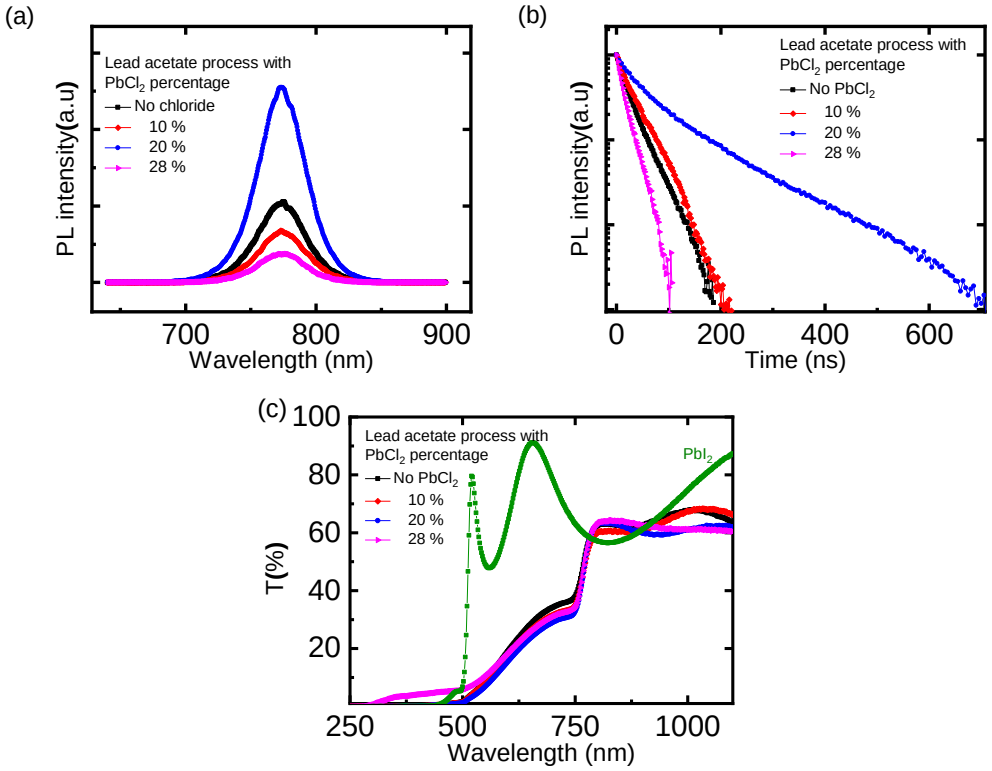

Figure 26. (a) Steady-state, (b) time-resolved PL and (c) transmittance spectra of perovskite layers on glass, deposited with the lead acetate process, with different $PbCl_2$ percentage in the perovskite solution. In (c), the transmittance of PbI_2 spin-coated on glass is included (in green) for comparison.

Samples of perovskite layers on glass are fabricated using the lead acetate method with different percentages of $PbCl_2$. In the PL spectra (Figure 26a) no shifts are observed as expected. There is however an increase of the PL amplitude for a optimal concentration of $PbCl_2$. Excess or lower $PbCl_2$ percentages than the critical hinder the optical characteristics. The response in time is also extended by changing lifetimes from 30 ns to 100 ns for the critical concentration (Figure 26b, 20%). In the transmission spectrum, it can be seen that the main change in is the range of 500-750 nm. Comparing the transmission spectra of the perovskite layers with PbI_2 spin-coated on glass (Figure 26c), it can be stated that the 500-700 nm range in the perovskite spectrum is related to the remnant PbI_2 in the layer. Under not-critical $PbCl_2$ percentages, PbI_2 is in excess in the layer, showing as an increased in the transmission spectra before the perovskite bandgap onset (750 nm). In the sample with critical $PbCl_2$ percentage (20%), the transmittance in this

wavelength range is reduced due to a reduction of PbI_2 in the resulting perovskite layer and the PL lifetime lengthened, evidence of an improved layer quality. However, despite the long lifetime obtained with the optimal $PbCl_2$ percentage, devices maintained low performances: the best performing device had a PCE of 14%, with a fill factor of 0.6 and strong instability in the *J-V* curve. Therefore, other PL-based method was devised to evaluate the stability of the perovskite layer.

5.3.Light soaking effect

One of the limitations of the perovskite for large scale implementation is their lack of stability. During current density-voltage (*J-V*) measurements, the power conversion efficiency (PCE) incurs an increase after repeating the measurement several times. This makes the identification of the real power conversion efficiency (PCE) of the PSCs a great challenge. This increase in the PCE is known in the CIGS research community [196] as the light soaking (LS) effect and it is a sign of self-healing of the material [197].

In order to establish the origin of the LS effect, photoluminescence (PL) measurements on the perovskite layers on glass deposited from the considered solution-processed methods are executed throughout a time frame. The measurements are executed with a 532 nm pulsed laser (further described in Chapter 0) during 30 minutes with a fluence in the range from 30-500 nJ/cm^2 to avoid nonlinear effects [198], at constant room temperature. The samples are measured before and after LS for 30 min.

PL spectra of the perovskite layers exhibit an increase of the PL emission upon constant illumination. The evolution of this increase is presented in Figure 27, for a $MAPbI_3$ layer deposited with the toluene process. After a time, the increase reaches a stable state. The time for stabilization depends on the fluence used to illuminate, reaching the stabilization point faster with higher fluences (within the measured range) [199].

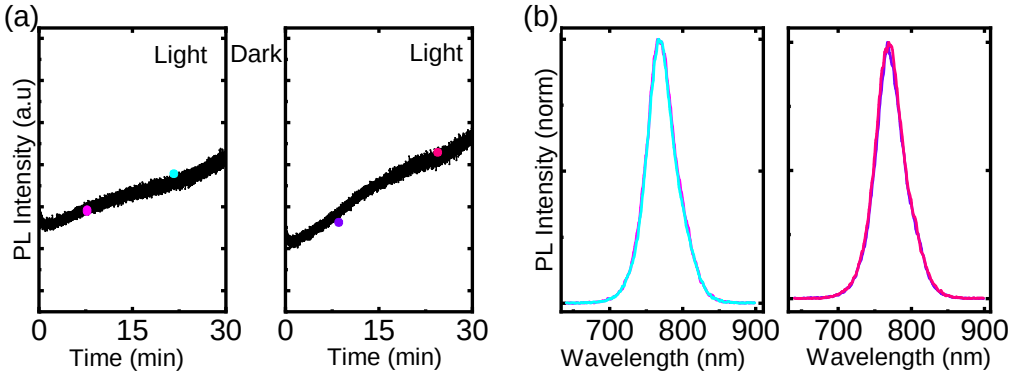

Figure 27. (a) Light soaking on perovskite samples during illumination and after 2 cycles of darkness. (b.) Normalized values of the PL spectra, showing no degradation of the sample.

Further evaluation of this increase after illumination in a series of intermittent dark and light cycles shows that the light soaking effect is a reversible phenomenon (Figure 27a). This change is reversible, as the PL emission is back to the original state after 30 min in the dark.

Comparison of the PL steady-state measurement in different points of the light soaking period (Figure 27b) shows that the PL spectra does not incur in spectral shifts or reshaping of the perovskite peak, indicating that the increase in the PL intensity is not associated to a degradation of the perovskite peak or the formation of different phases within the layer. Therefore the origin of the LS effect cannot be related to changes in the composition of the perovskite layer.

The PL dynamics are also evaluated, before and after LS (Figure 28). After LS, the PL emission is increased; both in amplitude and in lifetime indicating that, after the light soaking period, there are more free charges available for radiative recombination. The increase in PL amplitude (Figure 28a), for the same incident fluence, indicates that the absorption and emission conversion process are more effective in the perovskite layers after LS. Since the measured spot remains constant (and thus changes in the topography can be disregarded), for the same amount of incident photons there are fewer losses after light soaking.

The slope change in the semi-log plot of the time-resolved PL (Figure 28b) leads to the same conclusion. The total recombination rate, that is the inverse of the lifetime measured ($1/\tau$) depends on the rate of radiative and non-radiative recombination. The radiative depends on the material, and is not subject to changes, while the non-radiative depends on layer morphology, substrate temperature, surface traps, among others. An increase in the lifetime after light soaking indicates that the non-radiative processes are reduced.

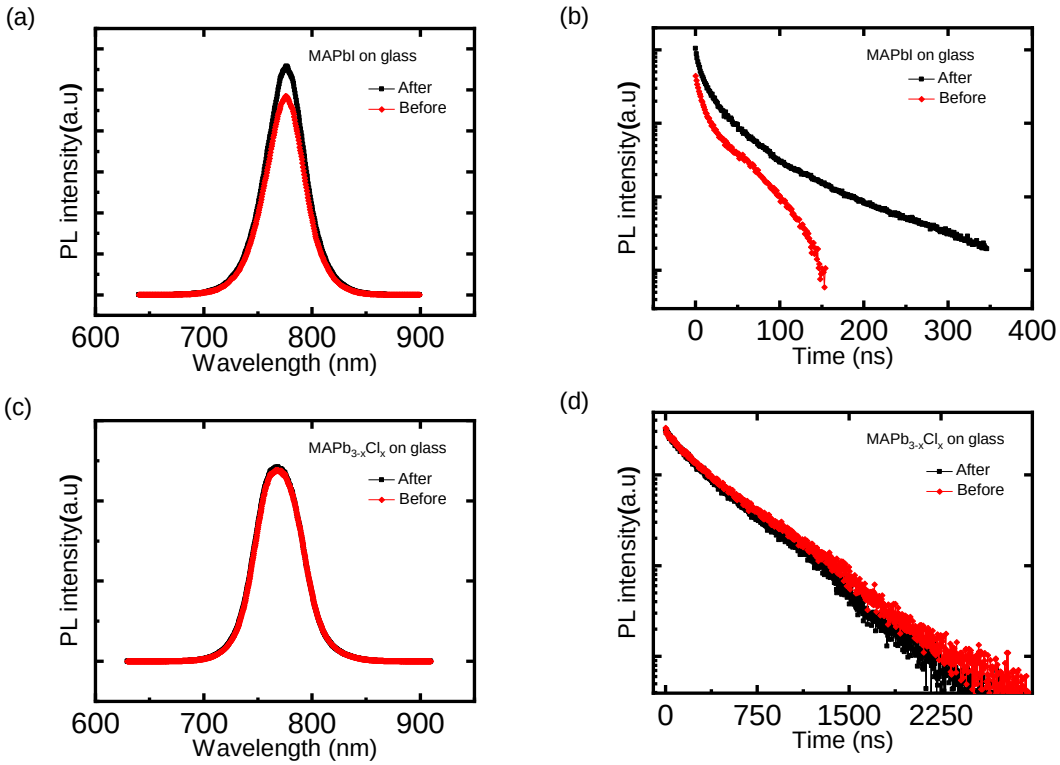

Figure 28. Steady-state and time-resolve PL of MAPI on glass before and after LS deposited using the one-step solvent-engineering process (a, b) and of $MAPbI_{3-x}Cl_x$ on glass deposited using the optimized lead-acetate process (c, d).

The same LS effect measurement is taken on $MAPbI_{3-x}Cl_x$[11] layers deposited from the optimized lead acetate process (Figure 28c and d). Upon light soaking for the same timeframe and fluence, the PL spectra present changes but much less pronounced than in the samples fabricated from the toluene process, making the layers less susceptible to the LS effect upon illumination. This different response indicates that the light soaking effect is dependent on the fabrication process and also on the layer quality.

5.4.1. Delta k estimation

When the PL of a perovskite layer, stored in the dark for a long time, is evaluated, all the traps in the perovskite layer are empty and the number of photons to be emitted after light absorption will be reduced by them. By using light soaking to study the PL dynamics, the photoactive traps are filled, so that their influence on the emitted PL is reduced. A more precise estimation can be then made of the lifetime of the charge carriers in the material.

Time-resolved PL before and after illumination (that is, the light soaking period), evaluates the decay rate in which the charge carriers are recombining radiatively. Therefore, in the case that illumination fills the traps at the perovskite layer, then, non-radiative recombination centers will be reduced, and a higher charge carrier density will recombine radiatively (Figure 29) [137], [199].

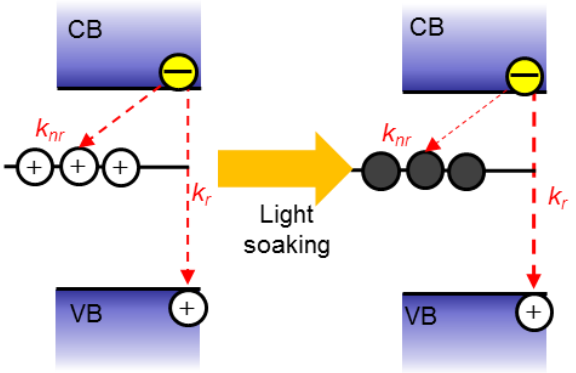

Figure 29. Schematic diagram of the trap filling in the perovskite layer upon light soaking.

The higher trap density in the evaluated samples, the higher the probability of a charge loss (that is, that non-radiatively recombines [200]). As consequence, the PL amplitude will be reduced, and also, the decay rate will be increased, as the charges have a higher probability of being trapped by the traps, and the PL transients will decay faster.

Trap deactivation occurs by illuminating the sample [201]. The absorbed photons will be effectively converted to electron-hole pairs and then reemitted after recombination, reducing the number of trapped charges since the losses due to traps will no longer have an influence on the final recombination rate. The total recombination rate is then the sum of the radiative

[11] In chapter 4.3 it was stated that the notations used here for the perovskite layer ($MAPbI_3$ and $MAPbI_{3-x}Cl_x$) do not indicate different crystalline structure. The notations are a reminder of the lead precursor of the perovskite layer (PbI_3 in the case of $MAPbI_3$ and $PbCl_2$ for $MAPb_{3-x}Cl_x$).

recombination rate and the non-radiative recombination rate, presented in Eq.(5.1). There, the suffix 1 is for the measurement before LS and the suffix 2 for the measurement after LS.

$$k_{PL1} = k_{r1} + k_{nr1}$$
$$k_{PL2} = k_{r2} + k_{nr2} \quad (5.1)$$

where k_r is the intrinsic decay rate, in the absence of non-radiative processes. k_{nr} is the non-radiative recombination rate and it will be affected by changes in the temperature, trap density, and layers defects. As the measurements are being executed on the same spot, same fluence and under constant temperature, the radiative recombination rate before and after does not change and thus $k_{r1} = k_{r2}$. Rewriting (5.1)

$$k_{PL1} - k_{nr1} = k_{PL2} - k_{nr2}$$
$$k_{PL1} - k_{PL2} = k_{nr1} - k_{nr2} \quad (5.2)$$

In this case, $k_{nr2} < k_{nr1}$, since after lightsoaking, the influence of the photoactive traps on the non-radiative recombination is reduced. Δk is defined as the difference between the non-radiative recombination before and after LS and will be related to the photoactive traps that are passivated by irradiation:

$$\Delta k = k_{nr1} - k_{nr2} \quad (5.3)$$

The photoluminescence phenomenon is the consequence of an effective conversion from absorbed photon to an excited state (electron) in the conduction band of a semiconductor and a hole left behind in the valence band, which recombine radiatively emitting a photon. During this process, the presence of traps can generate losses showing in the PL measurements as quenching. During fabrication and deposition, defects and traps may be formed and can act as electron leaks. In SCs this will manifest as a loss in performance, and part of the absorbed light will be lost and not participate in the current extraction.

In this case, the value of Δk will estimate the change in the PL decay due to the photoactive traps present on the illuminated sample. Traps that are not photoactive will not be modified before and after the measurement and will continue to hinder but these temporal changes will not address them. This value is sensitive to the morphology of the sample and of the local quality of the layer; therefore the experiment is repeated in different spots for a range of samples to obtain a better picture of the average influence of the traps in the decay.

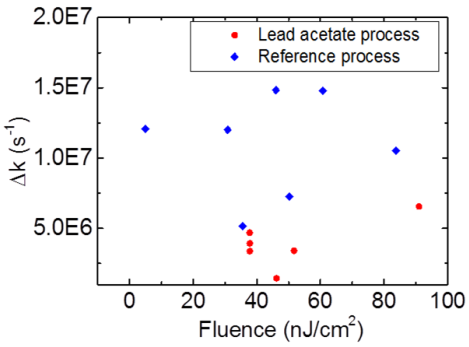

Figure 30. Δk values for perovskite layers deposited from lead acetate two-step process and the reference process, under different fluences

In Figure 30, Δk is presented for two methods of deposition: the toluene process (2-step solution deposition of MAI and PbI_2 with solvent-engineering step), the lead acetate process (1-

step solution deposition of MAI and PbAc). For the toluene process, the Δk value is larger compared to low solid concentrations of the lead acetate process and one order of magnitude larger than the results from the optimized lead acetate process, meaning that the decay slope has a stronger change after LS. Such changes are usually related to photoactive traps that are passivated by the incoming photons [75] and that, in the initial state, quench the total PL emission and shorten the decay.

Perovskite layers that show little or no increase in the PL intensity (and lifetime) after light soaking may still contain traps that hinder the optical characteristics. These traps are not photoactive[12] and implementation in devices will render no light soaking effect in the measurement of the power conversion efficiency.

5.4. Evaluation of optimized lead acetate method

In spite of the optimization processes, in many cases, the solar cells maintained low levels of efficiency, with strong hysteresis in the *J-V* characteristic curve and reduced stability in the evaluation of the PCE evolution in time. In order to reduce the hysteresis in the devices, a C_{60} fullerene interlayer is used (further discussed in chapter 6). However, this extra layer presents an additional challenge: the deposition of perovskite layers on hydrophobic substrates (C_{60}) limited the number of pixels per sample and often prevented the formation of a fully covered layer.

Figure 31. Perovskite layer quality on hydrophobic substrates deposited on (a) hot substrates, (b) cold substrates. (Perovskite solution deposited with slow dispense technique before spin-coating).

The lead acetate process, less sensitive to the light soaking effect, was implemented and optimized taking into account the implementation in hydrophobic substrates. In order to maintain the perovskite layer quality, factors such as the substrate temperature before perovskite deposition and the waiting time after spin-coating and before thermal annealing are optimized. The temperature change of the substrate would accelerate the formation of the perovskite layer before it was dispersed during the spin-coating. The evaluation of different waiting times after spin-coating would assist in ensuring a controlled crystallization rate for the perovskite layer.

[12] At the wavelength that the samples are being excited.

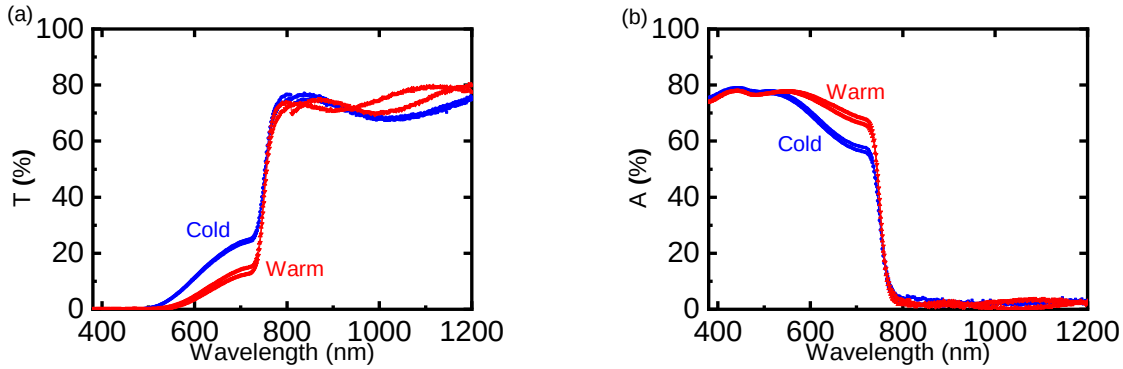

Figure 32. (a) Transmittance and (b) absorptance spectra of perovskite layers deposited on warm substrates (red), and cold substrates (blue). (Perovskite solution deposited with slow dispense technique before spin-coating).

Deposition of the perovskite layer on warm (75 °C) substrates facilitated the formation of the perovskite layer on hydrophobic substrates but it increased the inhomogeneities in the layer quality. Despite attempts of achieving homogeneous layers from sample to sample, the fast formation of the perovskite layer (upon perovskite solution dropping) hindered the homogeneity of the entire sample group (Figure 31a). Deposition of the perovskite solution on cold substrates (at room temperature) using the slow dispense technique, provided good continuity in the perovskite layer quality (Figure 31b).

Measurement of the transmission spectra showed the same onset for the perovskite absorption (740 nm) for both cold and warm substrates (Figure 32a). The main difference observed is in the 500-700 nm range, where the lead iodide peak is present (Appendix, Figure 75). In the cold substrates, the transmission in this range is larger, while it is suppressed in the warm substrates, indicating a stronger presence of PbI_2 in the perovskite layers deposited on the cold substrates. Higher PbI_2 content in the layers is reflected as a reduced absorptance in this wavelength range (Figure 32b).

Solar cells (devices) using this method are fabricated with the architecture: ITO/SnO_2/Perovskite/Spiro/Au, with increasing C_{60} interlayers between SnO_2 and the perovskite layer. The devices presented a large dispersion on the *J-V* statistics and a large series resistance (R_s). Temperature variation of the perovskite solution on top of the perovskite layer facilitated the coverage of the perovskite solution, but these perovskite layers are inhomogeneous and filled with pinholes, which explains the low power conversion efficiencies (PCE) obtained (Figure 33) despite the larger short-current density. Devices fabricated from cold substrates, performed with higher open-circuit voltage and fill factor, that is reflected on the larger PCE compared to the warm substrates.

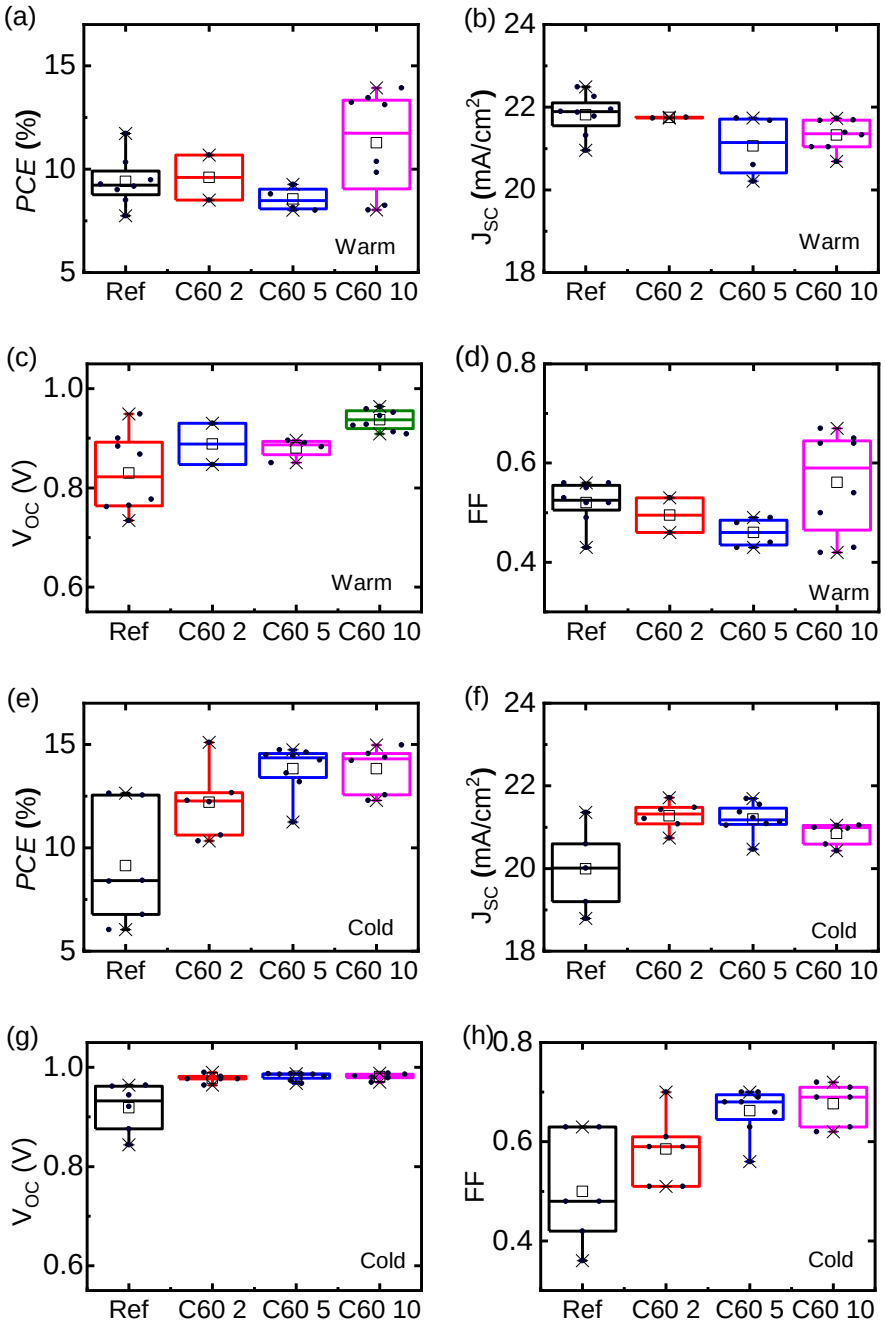

Figure 33. Statistical distribution of solar cell parameters extracted from *J-V* measurements in PSCs deposited with the optimized lead acetate with warm (a)-(d) and cold (e)-(h) substrates. Architecture: ITO/SnO_2/C_{60}/$MAPbI_{3-x}Cl_x$/Spiro/Au with solution-processed C_{60} interlayers (for evaluation of the process on hydrophobic substrates). In the figure: PCE: power conversion efficiency, J_{SC}: short-circuit current, V_{OC}: open circuit voltage and FF: fill factor.

Having established a protocol for the substrate temperature, the following factor to be evaluated is the waiting time. The manufacturing process on hydrophobic surfaces takes into account a slow deposition of the perovskite solution on the substrate. But as such, the use of a slow dispense system indicates that with rapid crystallization of the perovskite, accelerated crystallization can be created (leading to a higher number of defects and voids). Thus, to delay

the crystallization of the perovskite layer, a short time period (hereafter named waiting time) is inserted between the spin-coating and annealing cycles.

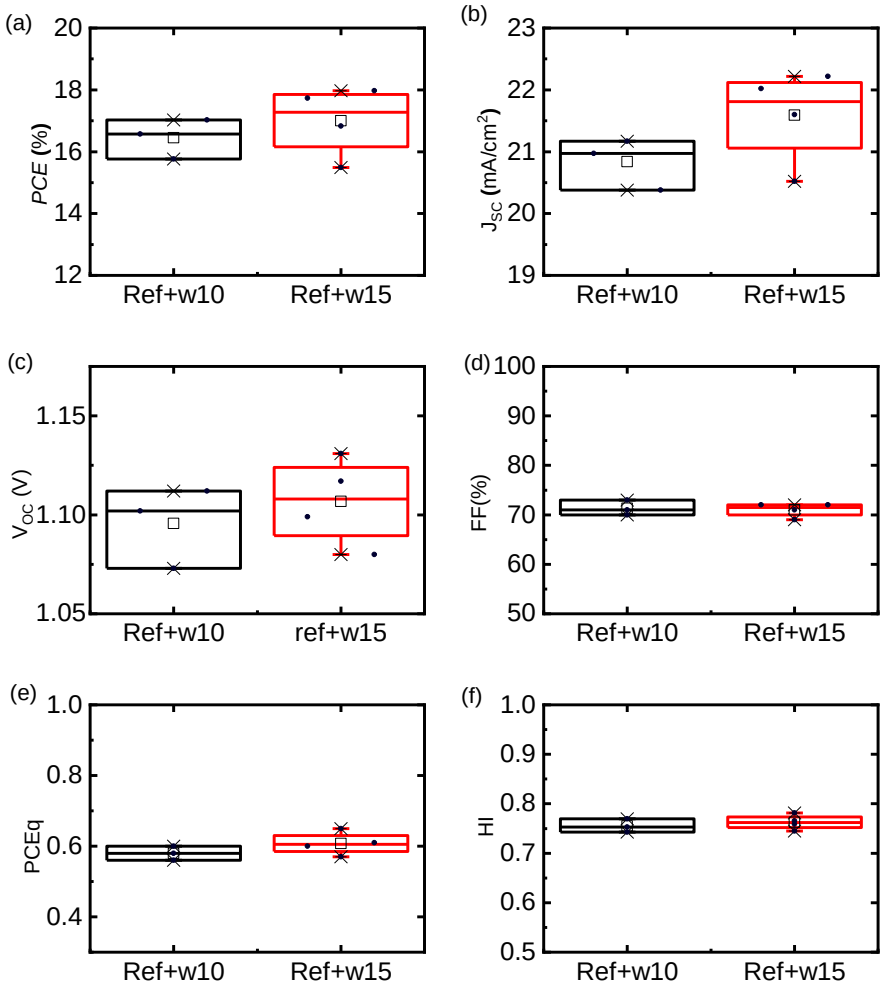

Figure 34. Statistical distribution of solar cell parameters extracted from *J-V* measurements in PSCs deposited with the optimized lead acetate with 10 and 15 minutes of waiting time. Architecture: ITO/SnO_2/$MAPbI_{3-x}Cl_x$/Spiro/Au. (a) Power conversion efficiency, PCE. (b) Short-circuit current, J_{SC}. (c) Open circuit voltage, V_{OC}. (d) Fill factor, FF. (e) PCE quotient, PCEq, the ratio of the backward and forward PCE, and (f) Hysteresis index, HI.

During the waiting time, the slow formation of a transparent brown perovskite layer is observed. 10 min is the minimum time it takes for the entire layer to present the same brown shade (shorter times show transparent yellow areas), but statistical evaluation shows that 15 min is a more suitable waiting time. Upon annealing after the waiting time, all layers turn opaque dark grey. In Figure 34, the statistical J-V parameters of devices with the architecture ITO/SnO_2/$MAPbI_{3-x}Cl_x$/Spiro/Au are shown. The addition of the waiting time improved the PCE compared to devices without any waiting time (Figure 33) and for a waiting time of 15 min a higher short-current density and open-circuit voltage are achieved. Furthermore, the PCEq and HI are slightly higher in the PSCs with longer waiting times. These two parameters are indicators of the deviation between the two measurements (back- and forward direction) or hysteresis.

In Figure 35, the UV-Vis spectra of $MAPbI_{3-x}Cl_x$ samples deposited on glass with the optimized lead acetate method and a waiting time of 15 min are presented to showcase the reproducibility of the method and the estimation of the absorption coefficient calculated from these measurements (1.5 $x10^5$ cm^{-1} at 532 nm). The (effective) diffusion coefficient and diffusion length calculated from the time-resolved PL (Figure 28d) and the method described in chapter 3.1.2 reaches up to 5.5$x10^2$ cm^2/s and 1300 nm, respectively, for electron extraction. These values are comparable to very high quality perovskite layers and are consistent with the literature[93], [135], [202]. Furthermore, the values calculated for the optimized lead acetate method are from 2-3 times larger than those obtained with the previous methods. Additional PL spectra and decay discussion on these layers is executed in chapter 6.

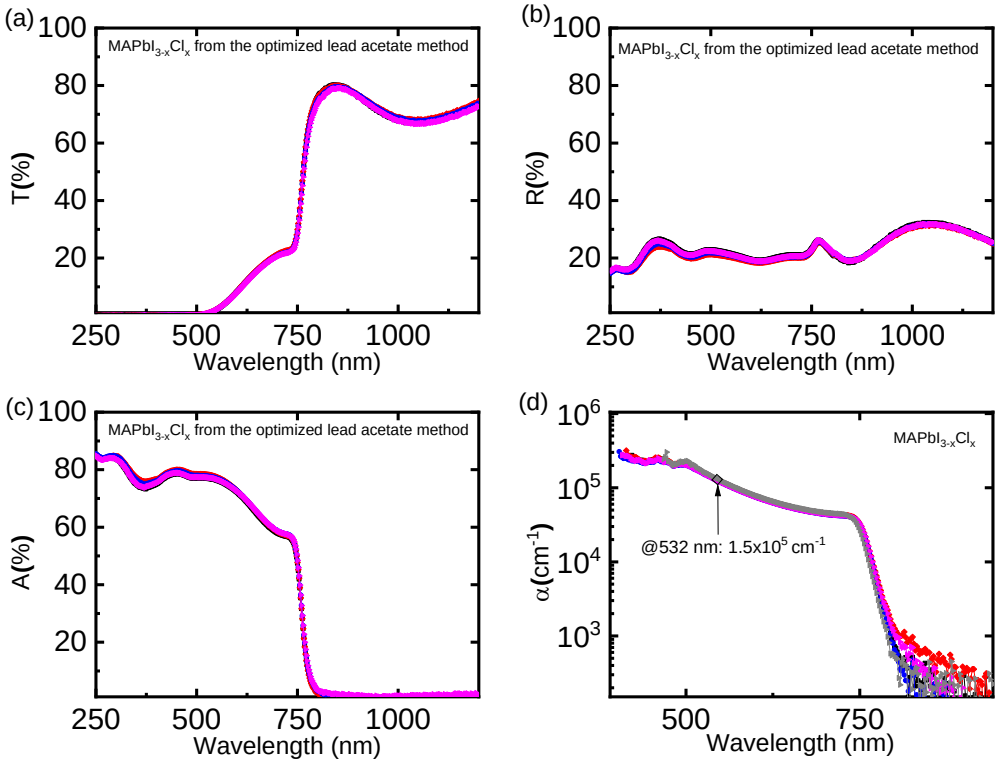

Figure 35. (a) Transmittance, (b) reflectance, (c) absorptance spectra and (d) absorption coefficient of perovskite layers deposited from the optimized lead acetate with 15 minutes of waiting time. Architecture: Glass/$MAPbI_{3-x}Cl_x$. Colors denote several samples to confirm reproducibility.

5.5. Discussion

In this chapter three perovskite solution manufacturing methods are evaluated. As a result of the changes in the optical properties of the resultant layers, the optimization of each method is carried out.

After LS, it is also important to evaluate the performance of samples with varying parameters by comparing data that has been generated by the same recombination mechanisms. By increasing the fluence from a low-injection regimen, we can observe that the PL decay changes, from presenting a mono-exponential decay to decays with more than one time constant. This means that if we measure using different fluences, we may obtain lifetimes that are not generated by

the same recombination mechanism and then the comparison will not provide an accurate description of changes in the film charge transport.

A value interesting to evaluate for morphology studies is Δk, described as the difference between the linear recombination rate before LS and after LS. As this process may fill surface traps that inhibit the radiative recombination of the charges, it provides information on the influence of the surface trap density on the recombination of the charge carriers. This indicated that changes in the fabrication method (in this case, precursor wise) cause a difference of an order of magnitude in the density values of photo-active traps. Of the three methods, the optimized lead acetate using the slow-dispense technique shows the lowest value, *i.e.* less susceptibility to the light soaking effect. This method is then used as the perovskite deposition method for the studies in chapters 6 and 7.

6. Perovskite interfaces as a source of hysteresis

In this chapter one of the sources of hysteresis in perovskite solar cells, charge trapping and detrapping at the perovskite interfaces, is addressed. A method to reduce the hysteresis is presented, where the J-V performance is improved by introducing an interlayer thus improving the contact between the electron transport layer (ETL) and the perovskite layer. Additionally, a study on the changes in the optical characteristics of the samples is performed to determine the mechanisms that lead to this improvement.

One of the challenges to overcome when fabricating perovskite solar cells (PSCs) is the presence of hysteresis in the evaluation of the electrical performance. The hysteresis is a deviation of the current extracted in the current density-voltage (*J-V)* characteristic curve when the measurement is executed in the backward or forward direction (described in Chapter 2), or by changing the speed of the measurement. This variation makes the reproducible characterization and optimization challenging.

Processes that originate hysteresis in PSCs are *ion migration within the perovskite layer* [203]–[207] and *charge trapping and detrapping at the perovskite interfaces* [118], [119], [125], [208]. Imram *et al*. state that it is the interaction of both these processes that yields a valid theoretical description for hysteresis as observed in the *J-V* curve [120]. Furthermore, they include a theoretical description of the *J-V* curve deformations close to the point (V_{OC}, J_{SC}) typically referred to as s-shapes. A crucial consequence of their findings is that interface properties between the perovskite and the ETL as well as the HTL can have a huge impact on the observed hysteresis.

In this chapter, we examine the impact of tin (IV) oxide (SnO_2)/perovskite interfaces on the hysteresis and s-shape effects in devices with the planar architecture: ITO/SnO_2/$MAPbI_{3-x}Cl_x$/Spiro/Au. Tin (IV) oxide (SnO_2) is commonly used as a compact ETL[209], as an alternative to titanium dioxide (TiO_2), due to its high mobility and low fabrication temperature. Both hysteresis and s-shape effects, however, remained a challenge to overcome for the device fabrication, as can be seen in the *J-V* curve in Figure 36(a). Juarez-Perez *et al*. in [210] state that the hysteresis is an indication of imperfect contacts at the perovskite interfaces and Xu *et al*. in [211] propose that the s-shape in the *J-V* curve is generated by the accumulation of charges in the interface. This configuration is known to present charge accumulation in the perovskite interface due to deep trap states[212]. Aygüler *et al*. mention that the optimum annealing temperature for achieving maximum power conversion efficiency (PCE) and smallest hysteresis in devices with SnO_2 as ETL is 180 °C. Thus, the reference device used in this study is fabricated at this annealing temperature. In this chapter, I address the charge trapping at the perovskite interface with the ETL by introducing a solution-processed C_{60} interlayer with the purpose to reduce hysteresis and improve the device performance.

C_{60} is introduced in the architecture as it is an effective electron acceptor [168] that has been largely used as a passivating layer in photovoltaics [213]. Fullerene-C_{60} or commonly known as C_{60} has been thermally evaporated alongside a PCBM (phenyl-C_{61}-butyric acid methyl ester) layer to passivate the traps at the interface [125]. The introduction of a passivating layer or interlayer into the PSC architecture will affect not only the optical characteristics, as there is an additional layer before the absorber layer, but also the transport properties, due to the presence of an interlayer that changes the charge extraction processes. Regarding the morphology of the perovskite layer, an interlayer would introduce changes in the surface where the perovskite crystallization is occurring, possibly affecting the crystalline orientation within the perovskite layer, and at a larger scale, variations in grain size and roughness.

6.1. Electrical Performance

The solution-processed C_{60} layer to be used as interlayer is spin-coated on top of SnO_2, followed by a thermal treatment, to evaporate the solvent before perovskite deposition. Further description of the fabrication method can be found in Chapter 4.

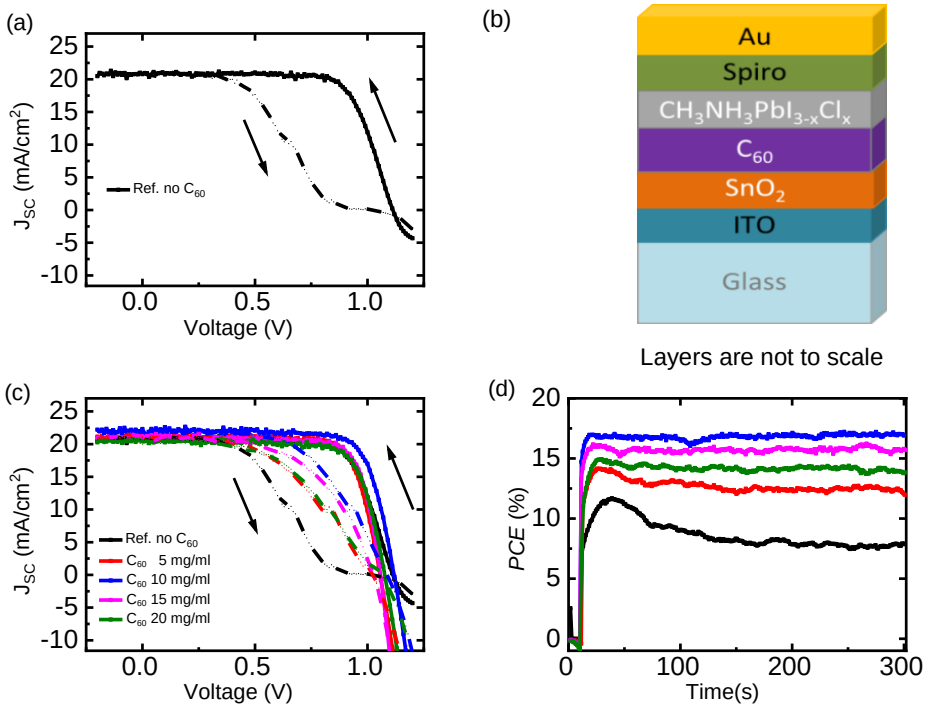

Figure 36. (a) *J-V* characteristic curve of the reference architecture. (b) Schematic diagram of the architecture used for PSCs with C_{60} interlayers. (c) *J-V* characteristic of perovskite solar cells with solution-process C_{60} interlayer in different concentrations (reference device in black). (d) Evolution of the PCE measured at constant voltage for the PSCs.

It was previously reported that through the control of the concentration of C_{60} in 1-2, dichlorobenzene (DCB), a range of thicknesses for the C_{60} layer can be achieved[13]. Here the concentration range shown for the devices and analysis is from 5 to 20 mg/ml in 5 mg/ml steps as this led to the best solar cell performance. The perovskite ($MAPbI_{3-x}Cl_x$) is deposited using the optimized 1-step lead acetate method described in Chapter 4. The hole transport layer used is

[13] Due to their small thickness, the determination of the thickness of solution-processed layer was non-trivial. However, the thicker layers are in the 10 nm range.

Spiro-MeOTAD (or in short Spiro), and the back electrode is a layer of evaporated gold (Figure 36b). With the inclusion of passivating layers into the device architecture, a modification of the electrical response is achieved: the s-shape of the reference in the forward *J-V* measurement (Figure 36c) is absent in the C_{60} devices. Additionally, the hysteresis between the forward and backward measurement is reduced. This effect can be related to a reduction of the charge carrier accumulation at the interface [211], indicating that the addition of the C_{60} interlayer is improving the contact between the ETL and perovskite layer.

The evolution in time of the power conversion efficiency measured under constant voltage (stabilized PCE or SPCE) is compared in Figure 36d. The reference device shows power conversion efficiency (PCE) of 12.5 % initially but after some minutes, this efficiency drops to 10 %. For the devices with C_{60} interlayers, the PCE stabilizes after a few seconds and at higher values (Figure 36d, Table 4). The usage of different C_{60} concentration for the interlayer formation point to a critical thickness of the C_{60} interlayer required for an optimum performance.

ETL	Scan direction	J_{SC} (mA/cm²)	FF (%)	V_{OC} (V)	PCE (%)	SPCE (%)
SnO_2: ref	forward	21.42±0.83	46.25±2.22	1.04±0.01	10.34±0.62	7.9
	backward	21.59±0.76	71±1.41	1.11±0.01	17.01±1.12	
SnO_2/C_{60} 5 mg/ml	forward	20.65±0.67	53.57±2.37	0.99±0.01	11.15±0.70	12.3
	backward	20.88±0.43	79.14±0.90	1.06±0.01	17.34±0.66	
SnO_2/C_{60} 10 mg/ml	forward	21.03±0.32	57.75±2.06	1.02±0.01	12.36±0.66	17.1
	backward	21.15±0.44	82.0±1.15	1.07±0.01	18.54±0.35	
SnO_2/C_{60} 15 mg/ml	forward	21.09±0.52	54.00±4.05	1.02±0.02	11.67±1.06	15.8
	backward	21.13±0.27	79.83±2.14	1.07±0.012	18.06±0.73	
SnO_2/C_{60} 20 mg/ml	forward	20.86±0.45	56.5±5.21	1.03±0.01	12.21±1.33	14.0
	backward	21.10±0.51	78.00±2.90	1.07±0.003	17.71±1.03	

Table 4. Average parameters for the devices with architecture ITO/SnO_2/C_{60}/$MAPbI_{3-x}Cl_x$/Spiro/Au, with different C_{60} concentrations, extracted from the current density-voltage curve and power conversion efficiency measured after 300 s at a constant voltage.

From Figure 37, we can observe the statistical parameters of the *J-V* characteristic values, taken with the configuration described here, and evaluating the presence of the C_{60} passivating layer in different concentrations. The PCE measured in backward direction is seen in Figure 37a, where the highest efficiency is achieved with the layer deposited from the 10 mg/ml solution. Comparing these results, it is clear that the increase in the efficiency does not come from a statistical increase of J_{SC} and V_{OC}, but from the fill factor, where an increase in 10 percentage points follows the same trend seen in the PCE. The hysteresis index (HI) indicates that devices with a thicker C_{60} interlayer have a stronger response against hysteresis and this is clearly seen in the *J-V* curves (Figure 36) where the s-shape is absent. In consequence, the implementation of C_{60} interlayers lessens the hysteresis in the devices by reducing the accumulation of the charge

carriers at the interface. This reduction, in turn, improves the power conversion stability of the devices.

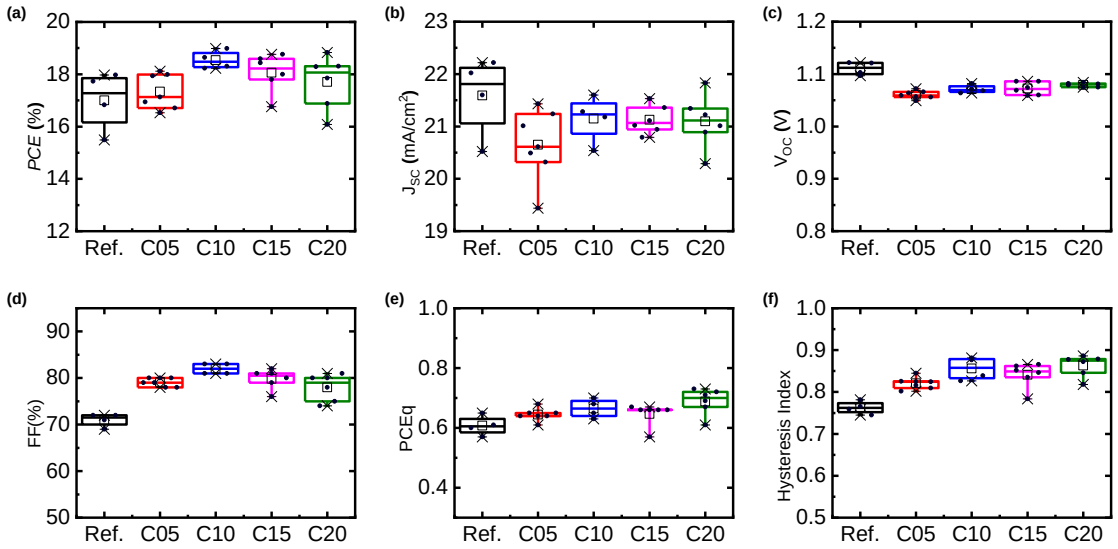

Figure 37. Statistical distribution of solar cell parameters extracted from *J-V* measurements in devices with C_{60} interlayer in the architecture: ITO/SnO_2/C_{60}/$MAPbI_{3-x}Cl_x$/Spiro/Au. Reference is the control device without C_{60} interlayer. (a) Power conversion efficiency, PCE. (b) Short-circuit current, J_{SC}. (c) Open circuit voltage, V_{OC}. (d) Fill factor, FF. (e) PCE quotient, PCEq, the ratio of the backward and forward PCE, and (f) Hysteresis index, HI.

Solar cells with C_{60} interlayers deposited through thermal evaporation were also implemented to compare the performance of the devices. Three thicknesses (5, 10 and 15 nm) were used. As with the solution-processed interlayers, the inclusion of an interlayer in the cell architecture improved the performance: both in the *J-V*, and in its stability.

6.2. Morphology of the interfaces and layers

Having shown that the C_{60} interlayer is effective in its improvement of the ETL/perovskite contact and as such, an improvement of the electrical performance, a study of the underlying principles behind this improvement is executed. The morphology of the interfaces and layers is now studied through AFM and SEM images.

In Figure 38, AFM images of the surface of the C_{60} interlayers can be compared to the bare SnO_2 surface[14]. The reference substrate, with SnO_2 as the underlying substrate (Figure 38a), presents a rough surface with a roughness of ~20 nm. The perovskite layer is ~300 nm thick, so it can be assumed that there is a uniform coverage of the perovskite forming on top of them. However, the roughness of the surface may oppose the transfer of charges. The C_{60} layers in the concentrations here used can be seen in Figure 38b-e. The thinnest concentration used (5 mg/ml) does not fully cover the SnO_2 layer and the low quality of this layer can be responsible for the drop in performance when used in devices. In the other parameters, the roughness of the

[14] The AFM images in this manuscript are taken by Tobias Leonhard.

SnO_2 underlying layer is dampened, giving an effective roughness of ~10 nm with the addition of the C_{60} interlayer (or even less for the 20 mg/ml concentration). As it grows thicker, the C_{60} layers start showing also aggregations on the surface, seen as the white round peaks in Figure 38d and e. Altogether, the reduction of the surface roughness can facilitate the contact between the perovskite layer and the ETL, due to a more homogeneous interface.

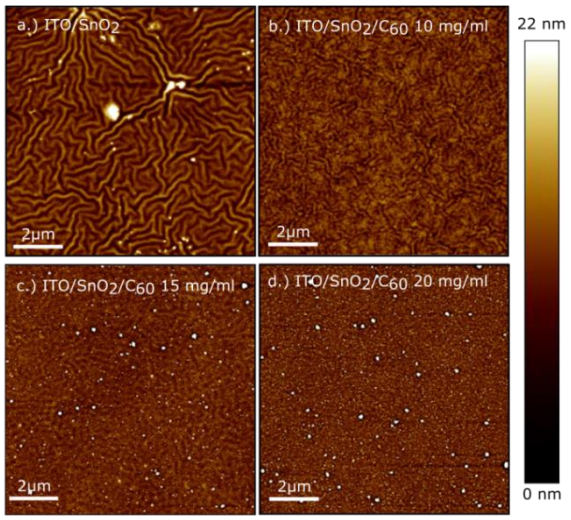

Figure 38. AFM images of the substrates for the perovskite layer in the reference and with the passivating layers. (a) ITO/SnO_2 (reference), (b) ITO/SnO_2/C_{60} 10 mg/ml, (c) ITO/SnO_2/C_{60} 15 mg/ml, (d) ITO/SnO_2/C_{60} 20 mg/ml.

After the deposition of the perovskite solution on the different surfaces, SEM images of the perovskite layers are taken to observe the quality of the layers and whether the underlying layer has an influence on the final morphology and crystallization of the top (perovskite) layer[15].

Figure 39 depicts the SEM images of a perovskite ($MAPbI_{3-x}Cl_x$) layer deposited with the optimized lead acetate method (described in 4.2.3). In Figure 39a and b, SEM images of the reference (ITO/SnO_2/ $MAPbI_{3-x}Cl_x$) show that the resulting perovskite layer consists of flat and large grains (~1 µm), with uneven layers covering the surface. The layer does not present any visible pinholes, demonstrating good coverage of the perovskite layer on top of SnO_2. There are, additionally, some smaller grains, seen in the image as lighter in color that may be an indication of PbI_2 formation and serrated boundaries on the perovskite grains. It should be noted that the reference layer already shows signs of degradation as evidenced by the small grains and serrated edges in the larger grains. These serrated boundaries may provide recombination centers or traps for the charges during extraction and as such, are undesirable. In contrast, the perovskite layers deposited over the C_{60} interlayer (10 and 15 mg/ml in Figure 39c-f) have large grains as well (~1 µm), with a well-defined layered surface. The serrated boundaries and smaller lighter grains seen in the reference are notably absent, indicating a reduction of the recombination centers and showing that the perovskite layer using the C_{60} interlayer has a higher quality than on the reference substrate.

[15] The SEM images in this manuscript were taken by Tobias Abzieher.

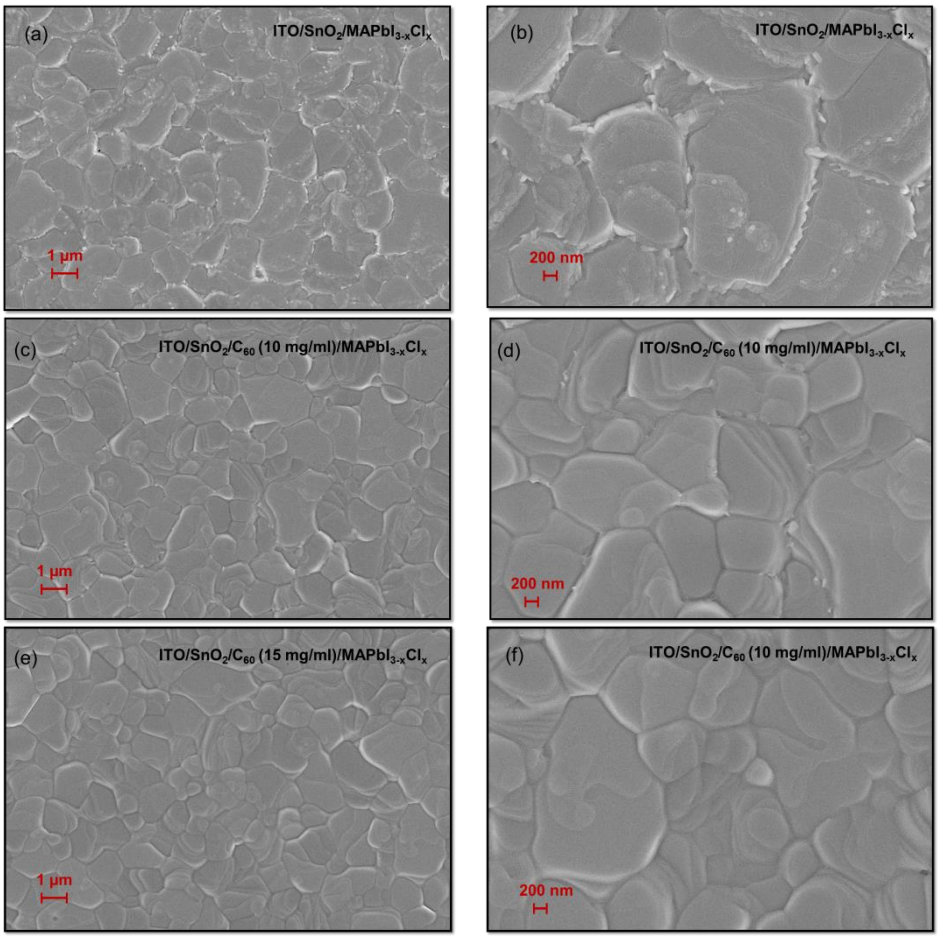

Figure 39. SEM images of perovskite layers with different substrates. (a, b): ITO/SnO_2. (c, d) ITO/SnO_2/C_{60} 10 mg/ml. (e, f) ITO/SnO_2/C_{60} 15 mg/ml. Images on the left are taken with a 20k x magnification and the images on the right with 50k x magnification.

6.3. Crystallization of the perovskite layer

In order to determine the composition of the smaller grains, and the orientation of the crystalline planes in the perovskite layer, x-ray diffraction (XRD) is executed on the layers to evaluate the influence of the underlying passivating layer in the formation of the perovskite crystalline layers.

Figure 40a shows the difractogram of the perovskite layer deposited on the different substrates. The main perovskite peaks can be seen at 14 ° ((100) plane, cubic), 28 ° ((200) plane, cubic) and 32 ° ((210) plane, cubic), indicating a pseudo-cubic crystalline structure [214]. These peaks are very strong indicating a high crystallinity in the perovskite layer. The dominant peak is the (100) crystalline plane, and the second largest is the (200) peak reaching ~36 % of the maximum. A small lead iodide peak can also be seen at 12.7 °, accounting for ~1.1 % of the highest perovskite peak (at 14 °). This percentage remains constant for all samples. This finding showcases that the smaller grains are not an indication of additional PbI_2 formation since lead iodide content remains constant all through the samples. The smaller grains then are evidence of broken pieces of the larger perovskite grains due to a higher defect density during crystallization.

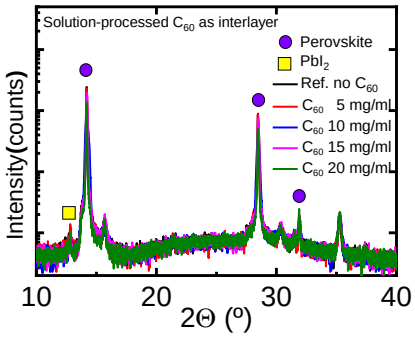

Figure 40. X-ray difractogram of perovskite deposited on different substrates, following the ITO/SnO_2/C_{60}/$MAPbI_{3-x}Cl_x$ architecture. Reference is the control device without C_{60} interlayer. The y-axis is a logarithmic scale. The perovskite peaks are signaled by purple circles, the PbI_2 peaks, with yellow squares.

Through the analysis of these spectra, it can be stated that there are no discernable differences in the alignment of the perovskite crystal planes for the samples with and without C_{60} interlayer, so the underlying substrate does not affect the crystallization of the perovskite layer. Therefore, the improvement of the electrical performance cannot be related to a change in the perovskite crystallization.

6.4. Optical characteristics

In the previous section, it is established that the crystal formation in the perovskite layer doesn't suffer strong changes due to the underlying layer. In this section the influence of the underlying layer is evaluated in terms of the optical response. Firstly, the transmission of different systems is presented in Figure 41a and b, (from the air side[16] and from the ITO side): the perovskite layer on glass, on ITO/SnO_2, and with the additional passivating layers. A sharp increase in the transmission is seen in all samples above 730 nm, related to the perovskite response. The slope and the starting point of the transmission band remain constant for all samples, ensuring that there are no changes in the bandgap of the perovskite layer, agreeing with the XRD results, as the lattice constants do not change in the different samples and thus, maintaining the same bandgap. The perovskite layers were also deposited on evaporated C_{60} layers following the same method to compare the optical characteristics (Appendix B), and the spectra showed no difference from the perovskite layers deposited on solution-processed C_{60}, thus confirming the robustness of the method.

A small increase in the transmission of the layers in the 500-700 nm range is the contribution of the presence of PbI_2 in the layer, corroborating the results of the X-Ray diffraction. After the bandgap, evidence of interference can be observed in the 750-1000 nm range due to the changes in the thickness of the different C_{60} layers. However, the drop in transmission at higher wavelengths (>1000 nm) is caused by an increase in the absorption of the substrate (ITO/SnO_2).

[16] Air side: illuminated from the side facing the perovskite layer

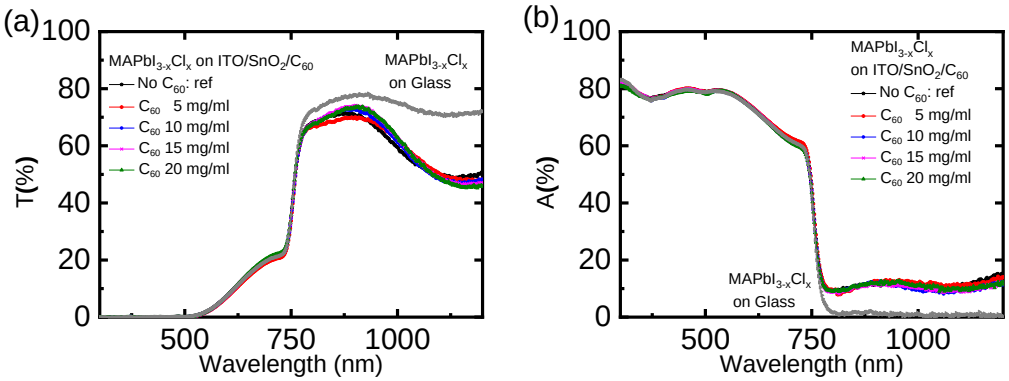

Figure 41. UV-Vis spectra of the ITO/SnO_2/C_{60}/$MAPbI_{3-x}Cl_x$ architecture, with different C_{60} layers. (a) Transmittance spectra, (b) Absorptance spectra of $MAPbI_{3-x}Cl_x$ on ITO/SnO_2/C_{60} (measured from the air side).

In Figure 42a, the spectral response of the solar cells with this configuration (C_{60} as interlayer, SnO_2 as ETL) shows an overall increase in the EQE with increasing C_{60} concentration, especially strong in the higher wavelengths (from 450-750 nm). This is another evidence of recombination losses that affect the reference device. The addition of a passivating layer reduces the losses at the interface and improves the overall performance. It should be noted that the reference devices do not perform with stable efficiency. Therefore, J_{SC} values do not match current density calculated from the EQE (J_{EQE}). In the C_{60} devices, the J_{SC} values match and the trend seen in J_{SC} is seen as well in J_{EQE} (Figure 43b).

In Figure 42b, the normalized EQEs are presented, taking the maxima of the reference EQE as normalization value to observe clearly the influence of the C_{60} interlayer. We can observe then, the trend in the higher wavelengths, with the EQE growing with the increase in the C_{60} concentration (or the thickening of the layers). However, in the PCE statistical values (Figure 37a), for increasing C_{60} concentration, the trend reaches a plateau. For a concentration of 20 mg/ml, there is a drop in the EQE at lower wavelengths (400-500 nm) that would indicate a reduction on the successfully extracted electron-hole pairs. This can also be evidenced in the transmission spectra of the C_{60} layers deposited on ITO/SnO_2: the transmittance drops in this range indicating absorption of light in this range that doesn't reach the perovskite layer (Figure 43a).

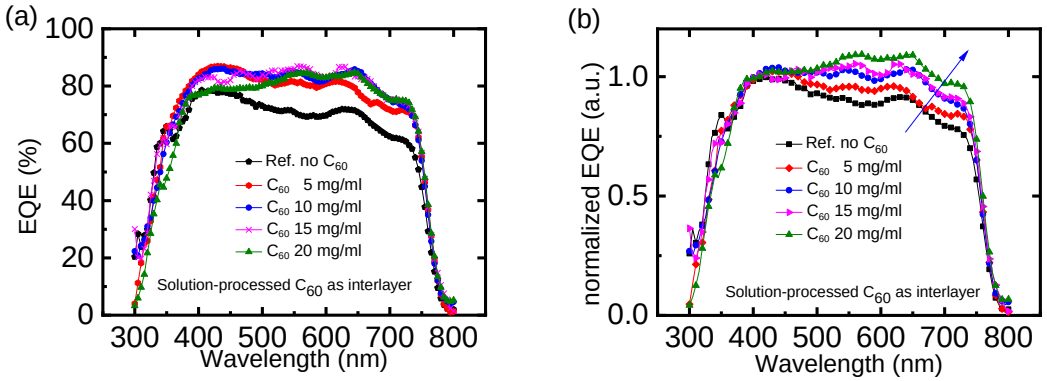

Figure 42. (a) EQE of the solar cells following the configuration ITO/SnO_2/C_{60} X/ $MAPbI_{3-x}Cl_x$/Spiro/Au. C_{60} is deposited via spin-coating from solutions. (b) Normalized EQE of the same cells. All signals are normalized to the maximum at the reference (at 400 nm).

The EQE peak shifts from 400 nm at the reference to 645 nm for the thicker concentrations. The layer with 10 mg/ml C_{60} concentration presents peaks both at 400 and at 645 nm, pointing at the origin of the plateau seen in the statistical PCE. A critical thickness of the C_{60} passivating layer is needed to balance the drop due to absorption at the interlayer, with the increase of the spectral response at higher wavelengths.

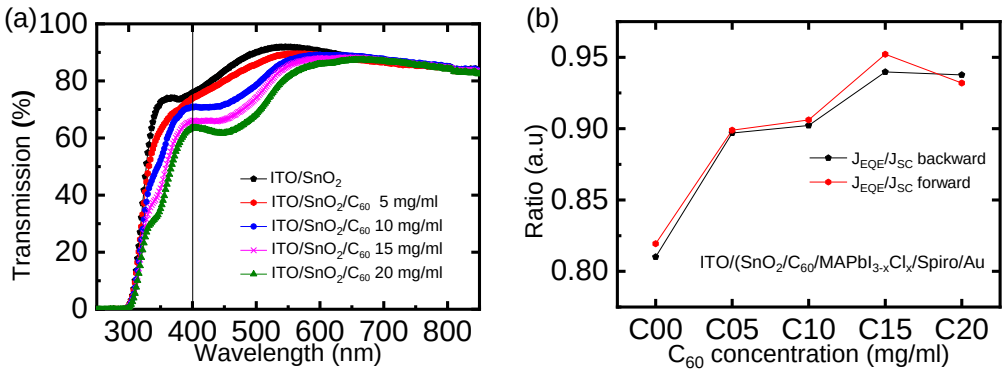

Figure 43. (a) Transmission of layers before perovskite deposition. The ITO/SnO_2 layer as reference and ITO/SnO_2 layers with C_{60} deposited from different concentrations. Black line denotes the wavelength for the maximum EQE value in the reference, shown here as a guide to the eye. (b) Ratio of the integral current from EQE measurement and the short circuit current (J_{SC}, measured in backward and forward direction).

The conjunction of these characterizations explains the changes in the electrical performance with different thickness of the passivating layer, despite having a similar transmittance response. Further evaluation of the layer indicated that when the evaluation of the spectra is measured from the ITO side (Appendix A), the absorption spectra of all the systems are increased compared to the same measurement from the air side. However, they do not significantly differ from one another. Despite the increasing thickness of the passivating layers, the absorption of the systems remains unchanged indicating that a percentage of the incoming light is absorbed by the C_{60} layer. In consequence, the light intensity that reaches the perovskite layer is reduced, compared to the light intensity for the reference or for the perovskite on glass, in agreement with the electrical parameters obtained in Figure 36, where the use of passivating layer also results in the drop of the short circuit current. These results, however, do not explain the improvement of the power conversion efficiency.

6.5. Transport mechanisms

With the evaluation of the UV-Vis spectra, the influence of the passivating layers in the absorption is defined and the source of the reduction of the short-circuit current determined. In order to discern the improvement of the fill factor in the devices, the generation and extraction of photo-generated charges in the samples are evaluated using photoluminescence and transient absorption.

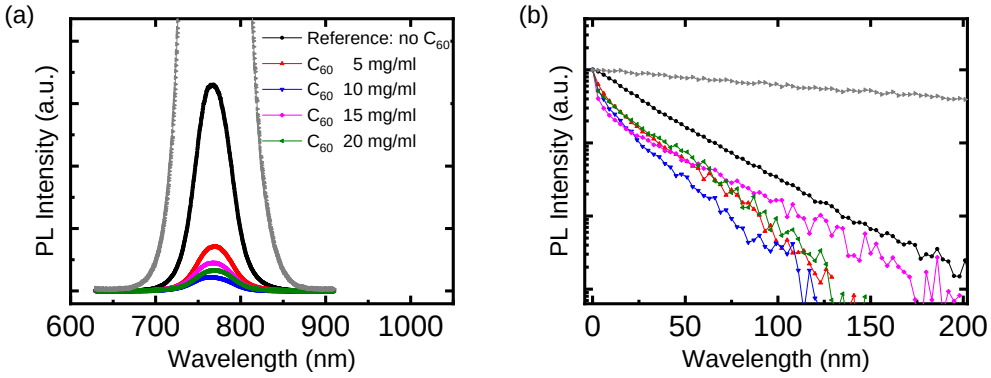

Figure 44. (a) Steady-state and (b) Time-resolved Photoluminescence of perovskite layers on glass, ITO/SnO_2 (reference), and ITO/SnO_2/C_{60} in different concentrations. In grey, the perovskite layer on glass for comparison.

The photoluminescence (PL) of the perovskite layers (without hole transport layer and gold electrode) is measured and compared (Figure 44) to observe the influence of the C_{60} layers in the charge transfer after optical stimulation. The measurement is executed before and after light soaking for 300 s (following the timeframe used for the stabilized PCE). During this time, there is no evidence of changes in the steady-state PL intensity and shape, indicating that there is no degradation of the samples during the measurement.

Perovskite on	τ_1 (ns)	A_1	τ_2 (ns)	A_2	τ_w (ns)	CTE relative to τ_w	CTE relative to τ_1
Glass	320±0.2	1	-	-	320 ±0.2	-	-
ITO/SnO_2: ref	11.4±0.1	0.96	41.6±2.0	0.05	12.8±0.2	0.95	0.96
ITO/SnO_2/C_{60} 5 mg/ml	4.4±0.3	0.63	16.2±1.0	0.36	8.7±0.5	0.97	0.98
ITO/SnO_2/C_{60} 10 mg/ml	2.6±0.2	0.64	14.1±1.0	0.34	6.5±0.4	0.98	0.99
ITO/SnO_2/C_{60} 15 mg/ml	1.9±0.1	0.60	14.6±0.6	0.39	6.9±0.2	0.98	0.99
ITO/SnO_2/C_{60} 20 mg/ml	4.2±0.4	0.87	24.7±1.1	0.13	6.8±0.5	0.97	0.98

Table 5. Lifetimes (τ_1 and τ_2) obtained from time-resolved photoluminescence measurements. For the sample in glass and ITO/SnO_2, a single-exponential decay equation is used (Eq. (6.1)). For the samples with C_{60} layers, a two-exponential decay equation (Eq. (6.2)) where A_1 and A_2 are the respective weights of τ_1 and τ_2. The weighted lifetime is calculated from $\tau_w = (\tau_1 * A_1 + \tau_2 * A_2)/(A_1 + A_2)$. The CTE is calculated using Eq. (3.11).

The photoluminescence of the perovskite layer on glass (Figure 44, in grey) is used as an insulating layer, to observe the lifetime of the charges when there is no quencher for the generated electron-hole pairs. The strong PL intensity and long lifetime (~320 ns) are evidence of the high-quality of the perovskite layer [129], [135]. In the steady-state measurement (Figure 44a), the reference sample (in black) is one order of magnitude smaller than the PL of perovskite on glass, indicating a quenching of the photoluminescence. The addition of the passivating layers continues to quench the PL signal even further, but it does not modify the shape of the PL. It should be noted that the quenching of the PL signal of a semiconductor, when

deposited on a quencher (in this case, an electron transport layer), is an indication of charge transfer between the semiconductor material (the perovskite) and the electron quencher (the ETL). This charge transfer results from the photo-generated charges no longer radiatively recombining but being transferred to the quencher (ETL) for further extraction. In consequence, the stronger quenching in the samples with a C_{60} interlayer is a sign of an improvement of the transfer of charges.

In the time-resolved measurements, the decay in the ITO/SnO_2/ $MAPbI_{3-x}Cl_x$ sample substrate is shortened compared to the perovskite on glass. This indicates an alternative path for the recombination of the photo-generated electrons: in addition to recombining radiatively at the perovskite layer (band-to-band recombination[215]), they can also be transferred to the SnO_2 layer and then extracted. This process is fast and it explains the drop in the lifetime (from 320 ns to 23 ns). The PL decay in this layer can be described using a single-exponential decay equation (Eq. (6.1)), where τ_1 is the charge transfer lifetime, A_1 is the weight of the lifetime and y_0 is the offset:

$$y(t) = y_0 + A_1 * e^{-t/\tau_1} \tag{6.1}$$

Adding the passivating layers to the architecture has two effects on the photoluminescence: an even stronger quenching of the steady-state PL (compared to the reference) and a faster decay of the time-resolved PL. However, in this case, the PL decay can no longer be described with a single exponential decay, indication of a second mechanism at work. In order to obtain the lifetime, the PL decay in the samples with C_{60} interlayers is fitted with a two-exponential decay equation (Eq. (6.2)), where τ_1 and τ_2 are the short and long lifetimes, A_1 and A_2 represent the weights of each lifetime and y_0 is the offset.

$$y(t) = y_0 + A_1 * e^{-t/\tau_1} + A_2 * e^{-t/\tau_2} \tag{6.2}$$

The fast lifetime is related to the transfer of charges [216], while the longer one is generated by another mechanism: electron back-transfer to the perovskite layer after being transported to the C_{60} layer, due to the closeness of the conduction band of C_{60} and the perovskite. This mechanism is explained further in Section 6.5.1.

For the architectures evaluated here, Table 5 presents the lifetimes and weights extracted from time-resolved measurements, with the weighted lifetime and charge transfer efficiencies (CTE). Both the CTE relative to the weighted lifetime and the CTE relative to τ_1 are included. It is relevant to note that for all C_{60} layers, the CTE is higher than in the reference, indicating that the addition of the C_{60} interlayer improves the charge transport in all cases.

6.5.1. Transient absorption

The second long lifetime seen in the time-resolved PL of the systems with C_{60} passivating layers can be attributed to a number of sources: delayed radiative decay [179], [216], and electron

back transfer. The transient absorption (TA) spectra and decay are then evaluated to determine the origin of the slow lifetime[17].

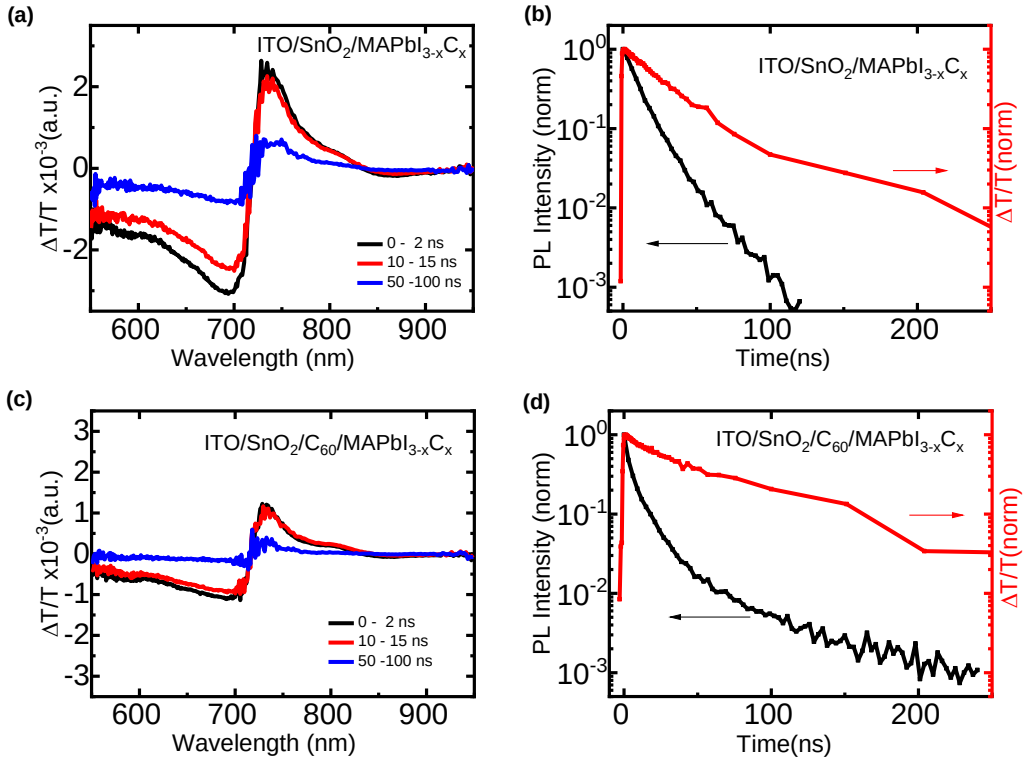

Figure 45. (a) Transient Absorption (TA) spectra of ITO/SnO_2/C_{60} (10 mg/ml)/$MAPbI_{3-x}Cl_x$. Transient Absorption decay and time-resolved photoluminescence data of (b) Reference: ITO/SnO_2/$MAPbI_{3-x}Cl_x$ and (c) Sample with C_{60}: ITO/SnO_2/C_{60} (10 mg/ml)/$MAPbI_{3-x}Cl_x$. The TA signal is integrated from the 600-700 nm range and inverted for ease of comparison. The blue lines serve as a guide to the eye.

Figure 45a and c show the transient absorption spectra of $MAPbI_{3-x}Cl_x$ measured on the reference (ITO/SnO_2) and with on ITO/SnO_2/C_{60} (10 mg/ml). For both samples, a first band can be seen in the 600-700 nm range, an indication of the induced absorption. A second band is seen, centered at 750 nm, sign of stimulated emission, alongside the ground state bleaching.

The evaluation of the transient is done by integrating the decay of the transient absorption in the 600-700 nm range and comparing it with the time-resolved PL (Figure 45b and d). For the reference (Figure 45b), the two decays (PL and TA) have lifetimes with different orders of magnitude, indicating that the mechanisms at work are different: the PL probes the extraction of electrons and is related then to the transfer of charges as explained above. Conversely, the TA is sensitive to the holes remaining in the valence band and will decay from non-radiative recombination with deeper states in the valence band (Figure 46a).

[17] The TA spectra were measured by Marius Jakoby.

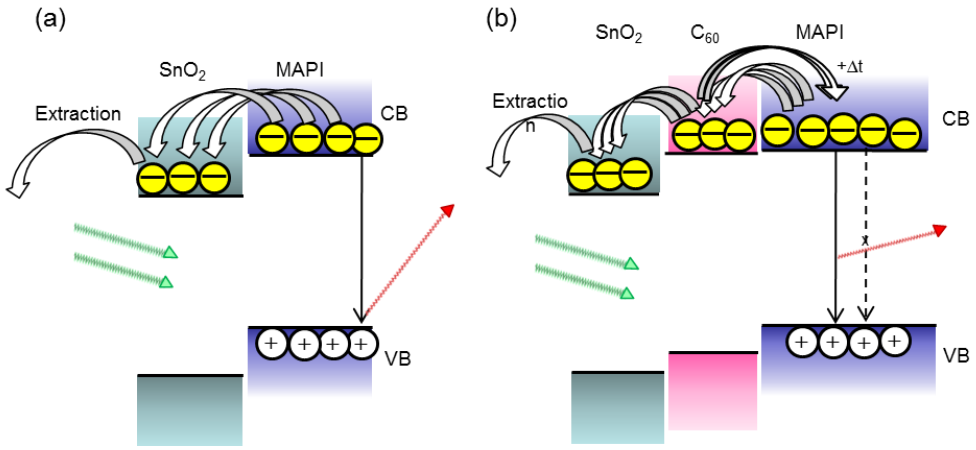

Figure 46. Schematic diagram of the energy bands and transport mechanisms in: (a) the reference (ITO/SnO_2/ $MAPbI_{3-x}Cl_x$) and in (b) ITO/SnO_2/ C_{60} (10 mg/ml)/ $MAPbI_{3-x}Cl_x$.

On the samples with C_{60}, the long PL lifetime follows the decay of the TA as seen in Figure 45d. After probing the sample, the excited charges are transferred to the extraction layer, demonstrated by the fast lifetime in the time-resolved PL measurement. However, due to the small difference of the energy level at the conduction bands of the perovskite and the C_{60}, a percentage of these charges can be transferred back to the perovskite conduction band. There, they can recombine radiatively with the holes remaining in the valence band, seen in the PL measurements as the second slower lifetime. At this moment, there are two mechanisms that are competing for the hole population in the valence band: the radiative recombination of the back-transferred electrons at the conduction band and the non-radiative recombination with electrons from deeper states at the valence band (Figure 46b). Since both mechanisms are limited by the hole density at the valence band, it shows as a similar lifetime in the TA decay and the time-resolved PL. In the reference layers, the difference at the conduction band is larger (4.5 eV [217]) and it is unlikely that charges return to the perovskite conduction band for any electron back transfer to occur. Additionally, the transfer of charges in the reference is slower and thus, dominates for longer time over other mechanisms.

6.6. Discussion

In the devices evaluated here, the influence of the C_{60} passivating layers is seen as an improvement in the fill factor of the *J-V* characteristic curve and in the absence of s-shape (which has been often related to interface phenomena [211]). Therefore, conclusions extracted from these transients assist in identifying the origin of such improvements. Even though the band alignment of C_{60} is not the optimal choice due to the closeness of the energy levels at the conduction band with the perovskite, it allows for a strong improvement of the charge transport from the perovskite towards the ETL. In the reference, the extraction is hindered by traps and charges are accumulated at the interface. During the backward measurement, the charges are easily extracted, and both the incoming light and the driving potential push for the extraction of current, facilitating the separation of charges. When the devices are measured in forward direction, the driving potential is not large enough to extract the charges that may accumulate during generation and extraction, increasing the resistance of the material to the electron flow and can explain the loss in efficiency and s-shape seen (with the second slope in the curve

caused by the breaking of the depletion zone due to a larger potential differential). In the forward measurement of the C_{60} devices, the closeness of the bands may introduce charges at the interface thus reducing the resistance of the material to the electron flow. During the measurement, the s-shape fades and therefore the fill factor increases.

In summary, hysteresis in the *J-V* characteristics can be significantly reduced by engineering the PSCs interfaces. To achieve an improvement in the performance, the good contact between the extraction and the perovskite layers needs to be ensured, and the perovskite interfaces need to be tightly controlled. The presented results show that the introduction of a passivating layer leads to a significant improvement of the performance by passivating the traps and facilitating the charge transport through the interface to better performing devices.

7. C_{60} as ETL: Stability and long-term performance

In this chapter, I study the effect of degradation in perovskite devices and layers. It is found that architectures with C_{60} as ETL maintain the quality of the perovskite layer for longer shelf-time and sustain the electrical performance of devices in time.

7.1. Introduction

Having determined that the interfaces are paramount for the improvement of the electrical performance, the stability of the devices is evaluated, and whether the proposed architecture is promising for a long-term stable device.

While evaluating the stabilized power conversion efficiency (PCE) of the devices with C_{60} as interlayer, it was established that the sole addition of the interlayer generates an increase in the efficiency after 300 s. Posterior measurements after storing the devices in nitrogen gloveboxes in the dark (Figure 47), show that the SnO_2 reference has a strong decrease in its performance. The devices with C_{60} as interlayer are stable, during a period of 2 months, but after 70 days, the performance dropped to 15 % (1 percentage point lost in the timeframe measured, 75 days).

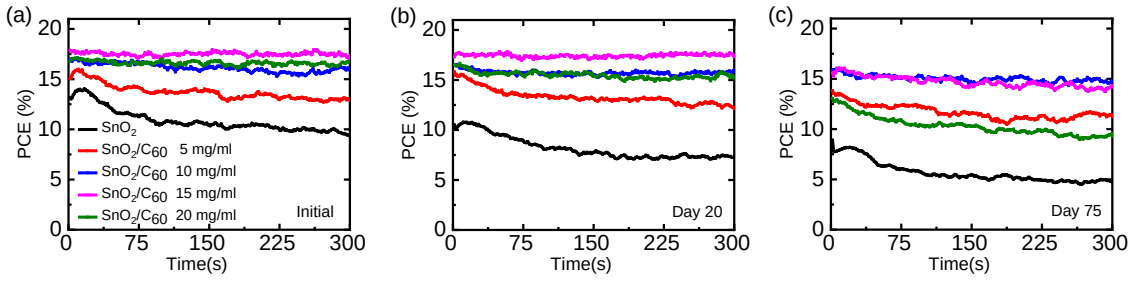

Figure 47. Evolution of the PCE at constant voltage for architecture with SnO_2 as ETL and C_{60} as interlayer measured: (a) upon fabrication, (b) after 7 days and (c) after 70 days.

SnO_2 as ETL introduces degradation mechanisms in the PSC through the accumulation of charges at the perovskite/ETL interface. In the *J-V* characteristic curve of reference devices (ITO/SnO_2/Perovskite/Spiro/Au), an s-shape can be seen reducing the PCE of the devices and in the evaluation of the PCE under constant voltage, a reduction of the stabilized PCE is measured after only 60 s of measuring. From the analysis executed in Chapter 6, it can be stated that under illumination, holes accumulate at the perovskite/ETL interface. The sustained presence of charges at the interface will facilitate the layer decomposition at the surface[218], detrimental to the perovskite crystal and increasing even further the surface trap density. Furthermore, the easy absorption of water in the SnO_2 surface affects electron mobility within the SnO_2 layer and causes a reduced band bending [219], hindering the electrical performance but also offering a degradation mechanism to the moisture-sensitive perovskite.

With the addition of the C_{60} interlayer in the device architecture described in Chapter 6, it is concluded that the charge accumulation at the ETL/perovskite interface can be avoided by improving the charge transport at the interface. Furthermore, since the devices are better with the addition of an interlayer, and C_{60} itself is an n-type semiconductor, the usage of SnO_2 as ETL can be brought into question.

C_{60} is a hydrophobic material with ambivalent behavior. It will repel the presence of water on its surface, acting as a hydrophobic material but when the water molecule is placed in the space between two fullerenes, it will keep the moisture caged [220]. When deposited in the ETL/interface of n-i-p PSCs, as shown in Chapter 6, the presence of C_{60} assists in the reduction of charge carrier accumulation at the frontal perovskite interface, facilitating the charge transport at this interface and, improving the performance of the devices. In perovskite solar cells, C_{60} has been used both as a passivating layer but also as ETL. So-called self-assembled monolayers (2 nm) have been deposited from dipping the substrates in a C_{60} solution [203], as well as single C_{60} layers fabricated from thermal evaporation (from 1-40 nm) [126], [174], [176]–[178], [180] obtaining a range of PCEs from 1.6% to 18.2%.

From chapter 6, solution-processed C_{60} layers are established as viable options for interlayers between the ETL and the perovskite to achieve stable and high-efficiency perovskite solar cells (PSCs). The next step involves the implementation of devices without the metal oxide ETL, given that the devices with the stand-alone ETL had lower and unstable performance. In this chapter, the metal oxide ETL is replaced by an organic semi-hydrophobic n-type material such as C_{60} and the effects of this modification on the long-term stability and degradation of the devices are studied.

7.2. Electrical performance upon fabrication

The architecture analyzed in this chapter consists of ITO/C_{60}/$MAPbI_{3-x}Cl_x$/Spiro/Au. The transparent frontal electrode is pre-structured ITO; C_{60} is deposited via spin-coating from solution as the electron transport layer (ETL). The fabrication parameters are described in Chapter 4 for the perovskite layer (deposited using the lead acetate 1-step optimized method), the C_{60} layer, the SpiroMeOTAD layer, and the gold evaporation. The concentrations used here for the samples are 5, 10, 15 and 20 mg/ml. During the experiments, it became clear that the C_{60} solution with 5 mg/ml concentration is too thin for providing sufficient coverage of the substrate, and therefore it is not an adequate concentration to use as a stand-alone ETL. However, this parameter is included in the analysis to establish the lower limits of the C_{60} concentration to use. Higher concentrations than 20 mg/ml reach the solubility limit of C_{60} in DCB and are not used in this study. The high performance of devices built with solution-process C_{60} layers with the concentrations of 10, 15, 20 mg/ml is corroborated in the statistical studies (Figure 49). Despite the loss in short-circuit current (compared to the ITO/SnO_2 reference device, with an average of 21.8 mA/cm^2), the devices show improved efficiency, influenced by the high open-circuit voltage and excellent fill factor. The hysteresis is also reduced in these devices.

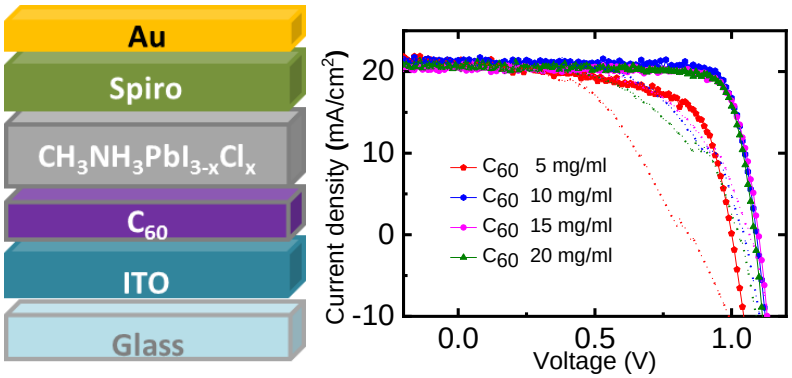

Figure 48. Left: Schematic diagram of the architecture. Right: *J-V* characteristic curve of solar cells with the architecture: ITO/C_{60}/$MAPbI_{3-x}Cl_x$ /Spiro/Au, with different C_{60} concentrations.

The devices with the architecture previously described (Figure 48, left) perform successfully upon fabrication, without evidence of shunt paths within the device due to perovskite infiltration into the C_{60} ETL. Furthermore, the average power conversion efficiency (PCE) in the devices with C_{60} as ETL is improved with respect to the former architecture (with SnO_2 as ETL and C_{60} as interlayer). For C_{60} concentrations higher than 10 mg/ml, the PCEs obtained in the *J-V* curve are over 18 % (18.8 % for the best cell), with open-circuit voltages (V_{OC}) around 1.1 eV, fill factors (FF) over 80% and very good hysteresis indexes (HI), despite the loss in short-circuit current density. Furthermore, a reduction of the series resistance can be seen with increasing C_{60} layer concentration (Figure 48, right).

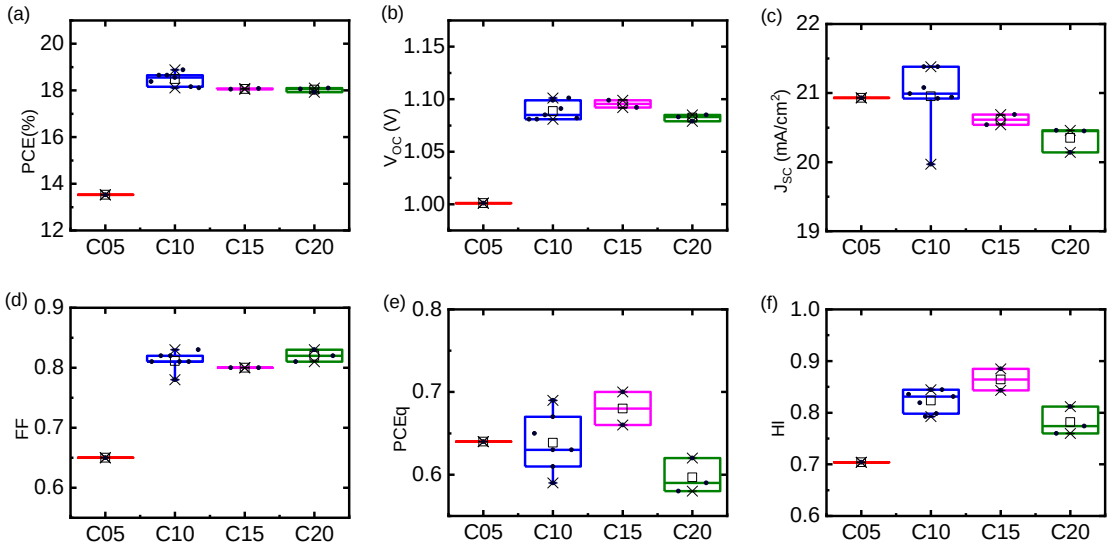

Figure 49. Statistical parameters extracted from the *J-V* characteristic curves of solar cells with the architecture: ITO/C_{60}/$MAPbI_{3-x}Cl_x$ /Spiro/Au. a.) power conversion efficiency, b.) Open circuit voltage, c.) Short-circuit current, d.) Fill factor, e.) PCE quotient f.) Hysteresis index.

The drop in short-circuit current for increasing C_{60} concentration is generated by the reduction in the incident light reaching the perovskite absorber. As mentioned in Chapter 6, Section 6.4, the thickening of the C_{60} layer with increasing solution concentration reduces the transmission

in the 320-600 nm range. However, this reduction is compensated by the increase in fill factor, leading to the improvement in the PCE.

7.3. Morphology and crystallization

In terms of the morphology of the perovskite layers, SEM images of the perovskite layers deposited directly on ITO (Figure 50, upper images) are evaluated, showing a mixture of two types of grains: a large, flat one, related to the $MAPbI_{3-x}Cl_x$ and smaller grains, often related to the formation of PbI_2 [221]. As mentioned before, the smaller grains can be a source for non-radiative recombination due to the higher density of defects. On the other hand, when C_{60} is used as ETL (Figure 50, lower images), the C_{60} acts as a stabilizer of the perovskite in formation, and as a consequence, the quality of the perovskite layer is improved, with tightly-packed flat grains, with well-defined boundaries and fully covered layers.

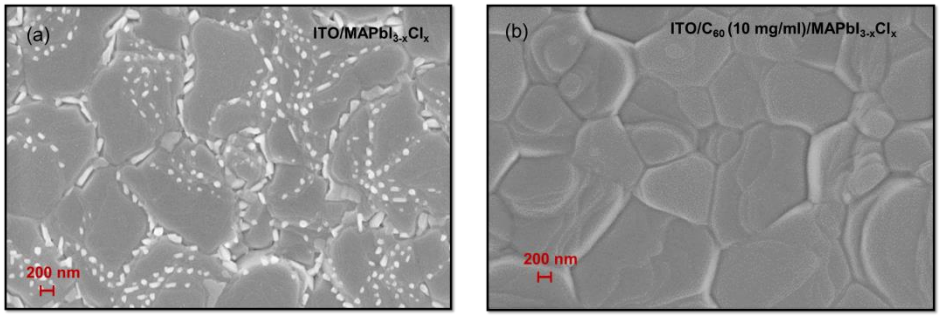

Figure 50. SEM images of perovskite layers with different substrates. (a) ITO/ $MAPbI_{3-x}Cl_x$, (b) ITO/C_{60}/$MAPbI_{3-x}Cl_x$. Images with 50k x Magnification.

In order to evaluate the resistance of the devices to degradation, measurements of the characteristics are executed at different times. Alongside this, we evaluated the reference (ITO/SnO_2/ $MAPbI_{3-x}Cl_x$) under the same circumstances to establish a control device.

In the initial results of the x-ray di ffraction (XRD) of the perovskite layers on the different ETLs, the data indicates that there are no discernable shifts or peak reduction between the spectra of the perovskite deposited on C_{60} or on SnO_2 (Figure 51a). Therefore, in the initial state, the crystal alignment of the perovskite deposited on the two types of ETL remains constant. Moreover, in all evaluated samples a small PbI_2 peak can be seen at 12.7 °, indicating a small percentage present in the perovskite layers. Bi *et al.*[222] reported that a small percentage of PbI_2 in the perovskite layer may improve the performance since it reduces non-radiative recombination.

Further evaluation on days 7 and 90 (Figure 51b-d) shows that there is an increase of the PbI_2 peak in all samples, evidence of the aging process already started even though the samples are kept in the dark and in the glovebox. The main differences are seen in the perovskite peaks (100) and (200): in the reference, the perovskite peaks are smaller and narrower after 90 days, while in the C_{60} samples, the perovskite peaks remain stable. A narrower peak often is related to an increase in the crystallite size; however, the reduction of the peak magnitude also indicates a reduction in the crystalline planes alignment. Based on these results, the crystal alignment and intensity of the perovskite peaks is maintained during 90 days in the perovskite layers with C_{60}

as a substrate. In the reference, the perovskite peaks get reduced during this timeframe, evidence of the erosion and increased crystal disorder of the perovskite layer.

With these characterizations, the initial frame is established for high-performance devices using C_{60} as ETL. The perovskite layer thus obtained has an improved quality layer evidenced by the increased stability of the perovskite crystal, reduced defect density, and improved grain size.

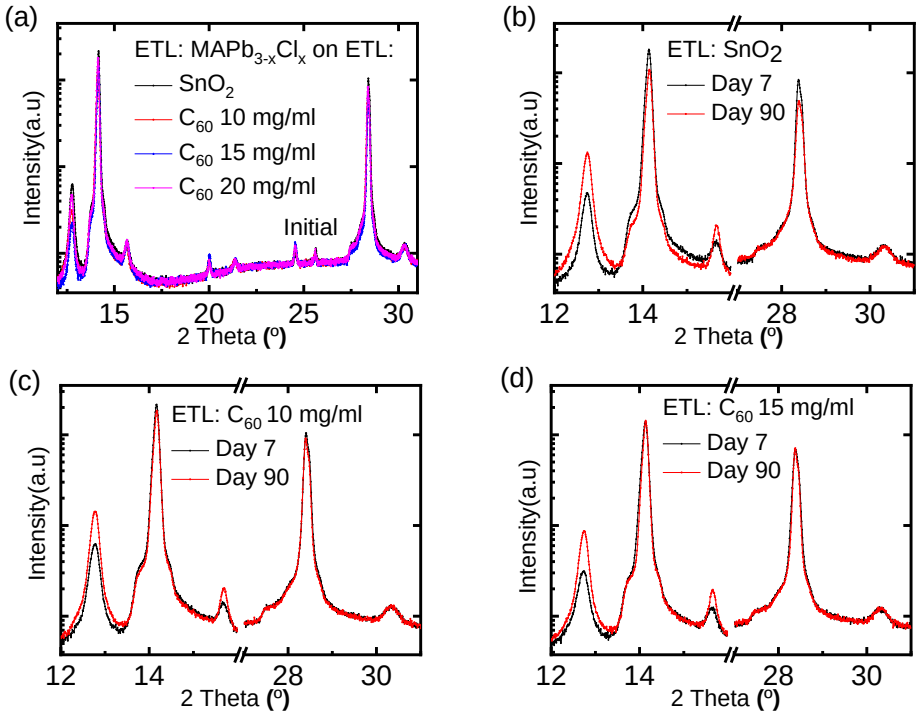

Figure 51. (a) X-ray diffraction spectra of $MAPbI_{3-x}Cl_x$ layers on ITO/SnO_2 and ITO/C_{60} (from different concentrations). Zoom of the main perovskite peaks, (100) and (200), as evaluated from day 6 and day 90 in (b) Reference, (c) C_{60} 10 mg/ml, (d) C_{60} 15 mg/ml.

7.4. Degradation in the EQE

Having corroborated that the morphology of the perovskite layers with different substrates is modified, however, the crystal alignment remains similar. Therefore, the next step is to study the spectral performance and how the aging mechanisms affect the response.

Evaluation of the EQE spectra in the C_{60} devices compared to the SnO_2 reference devices upon fabrication is presented in Figure 52a. In the EQE spectra, a sharp drop at 750 nm is observed for all devices. In the C_{60} devices, there is an increase in the overall EQE compared to the reference, seen mainly in the longer (red) wavelengths. The reduction of the EQE in the reference is introduced by recombination losses (as described in Section 6.4). Replacing the SnO_2 with a solution-processed C_{60} layer improves the EQE and normalizing the values at the maxima of the control device, it can be determined that the increase is seen in the entire range of the EQE. However, since the C_{60} layer absorbs in the blue region, it is only seen as a change in the red wavelength range.

Reductions in the overall EQE are often related to reflection losses and changes in the diffusion length, but the perovskite layer remains unaltered for the evaluated devices and the reflection spectra do not show strong differences that could explain the EQE response (Appendix C). However, the charge transport between the perovskite and the C_{60} layer is significantly improved compared to the charge transport between SnO_2 and the perovskite layer, and as such, the increase of the overall EQE is a consequence of the improved charge transfer in the C_{60} /perovskite interface. A slowed-down transport limited by charge carrier accumulation at the ETL/ perovskite interface will render (if calculated) an underestimation of the perovskite diffusion length, given that the real value is going to be masked by the charge accumulation at the interface.

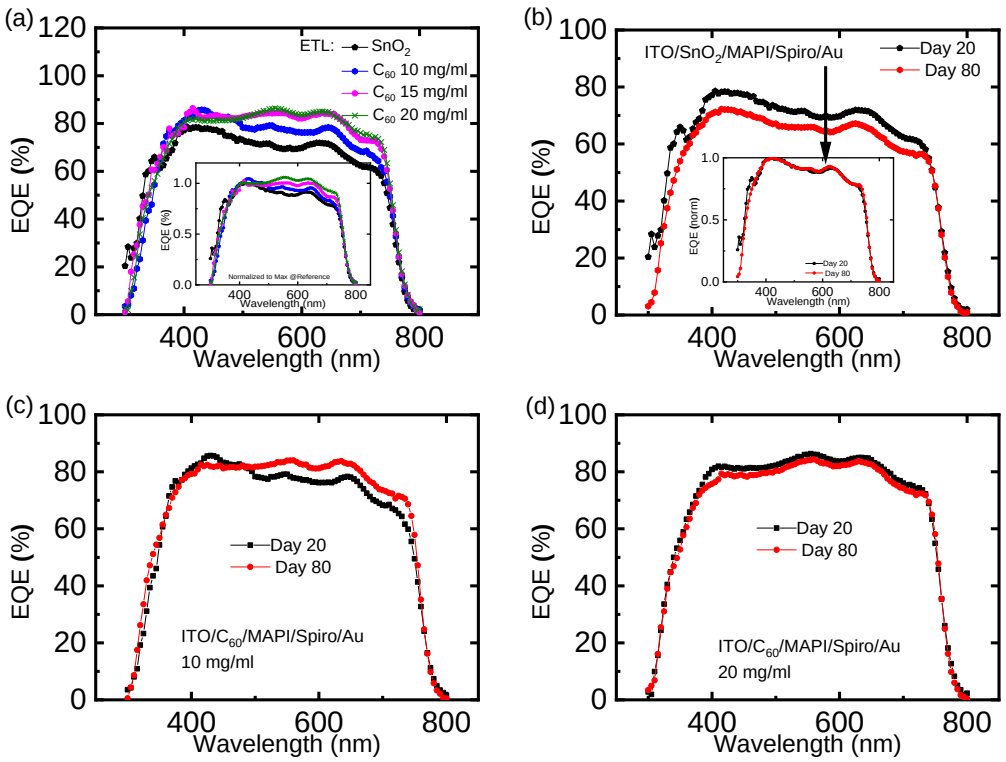

Figure 52. (a) EQE of the C_{60} devices under illumination compared to the Reference (SnO_2 as ETL). Comparison of the EQE after storage time in (b) the Reference device, (c) device with 10 mg/ml C_{60} layer as ETL and (d) the device with 20 mg/ml C_{60} layer as ETL.

Further evaluation of the changes in the EQE after the devices are stored in the dark in a nitrogen glovebox (after 20 and 80 days, to impose aging degradation, Figure 52b-d), indicates that the reference device shows a reduction of the EQE all throughout the wavelength range. Normalizing the spectra (insert in Figure 52) shows that this loss is related to the reduction of the total current extracted from the device in the measured range. On the other hand, the C_{60} devices barely suffer any changes between the two measurements, evidencing a suppression of the aging process that in the reference devices starts as a drop in current.

7.5. Degradation in the *J-V* measurements

After studying the spectral response of the devices and identifying initial sources of performance losses, the following step was performed to study the performance in time and how the aging mechanisms affect the stability of the PCE.

One of the limiting factors of PSCs is their performing lifetime in comparison with silicon SCs. Thus, much of the current research is devoted to extend their lifetime either by isolating the material from environmental factors that degrade the absorber or by making the absorber less susceptible to these factors. As mentioned earlier, SnO_2 is a material sensitive to both moisture[219] and oxygen [223] and its electronic properties change under the presence of either. Thus, even by ensuring that the water is extracted from the devices after SnO_2 deposition (*e.g.* by placing the devices in a hot plate for over an hour at 100 °C inside of a glovebox), there is the probability of oxygen absorption in the SnO_2 layer during the oxygen doping step for the Spiro layer and thus, a path for the degradation of the device.

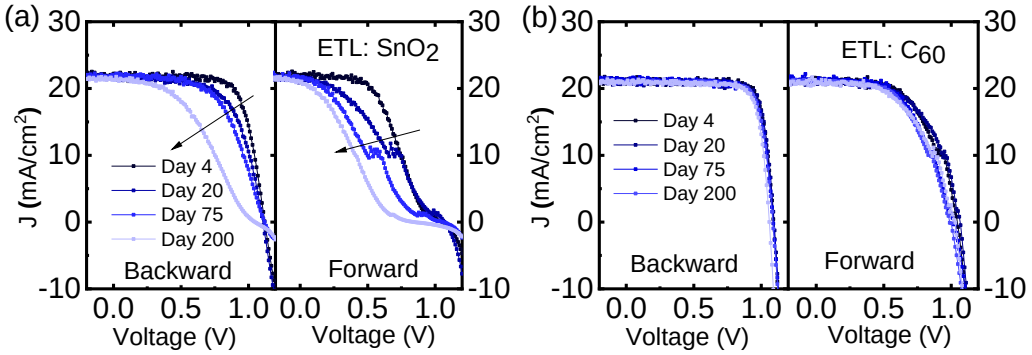

Figure 53. *J-V* curve of the reference (a) and the C_{60} device (b) evaluated in the backward and forward direction and throughout a range of days. The samples are stored between measurements in a nitrogen glovebox in the dark.

Comparison between the current density-voltage (*J-V*) curve of the reference devices and the *J-V* of devices with C_{60} as ETL, measured throughout a range of days, showcases a different influence of the aging in the electrical parameters (Figure 53). For the reference sample at the starting point, the s-shape in the forward measurement is an indication of charge accumulation at the frontal interface (as is discussed in Chapter 6). With aging, this s-shape is accentuated, even appearing in the backward measurement. At the end of this period, the performance of the reference devices has lost 10 percentage points. On the other hands, in the C_{60} devices (with the 10 mg/ml concentration here presented due to its optimum performance) the *J-V* curves barely show any changes throughout the timeframe of measurements. The fill factor remains stable in this period and while there is a slight drop in the open-circuit voltage (V_{OC}), the average performance is sustained.

The evolution in time of the electrical parameters is presented in Figure 54, as they are measured through a 180-days timeframe. The reference sample presents a strong loss of the PCE (from 17 to 15%) in the first 10 days, continuing to lose percentage points at a slower rate after. The evaluation of the XRD of the reference shows also the PbI_2 peaks increase after storage time, as an indication of a larger percentage of PbI_2 in the perovskite layer, and that the perovskite peaks are reduced in intensity, compared to the initial measurements. In other words, the quality of the perovskite layer in the reference is reduced after storage time. Erosion of the perovskite layer introduces then, additional defects states that diminish the electrical performance.

On the other hand, C_{60} devices presented no changes in the perovskite peaks during the measured timeframe. In the same way, the PCE of the C_{60} devices remained stable. At the

beginning of the evaluation, the average PCE is 18% and the devices maintained a PCE over 16% throughout 180 days of measurement, losing only 2 percentage points after the measured timeframe.

In terms of aging, the fill factor in the *J-V* curve is the parameter that introduces the most discerning information, as a loss of the quality of the perovskite layer will be reflected directly on this parameter, facilitating the identification of the level of damage affecting the absorber. In this evaluation, the reference device loses most of the performance on the first few days and this reduction is led by the fill factor (Figure 54d). On the later part of the timeframe, the fill factor remains constant while the V_{OC} and J_{SC} start to drop. Therefore losses related to these parameters start affecting the devices after 60 days.

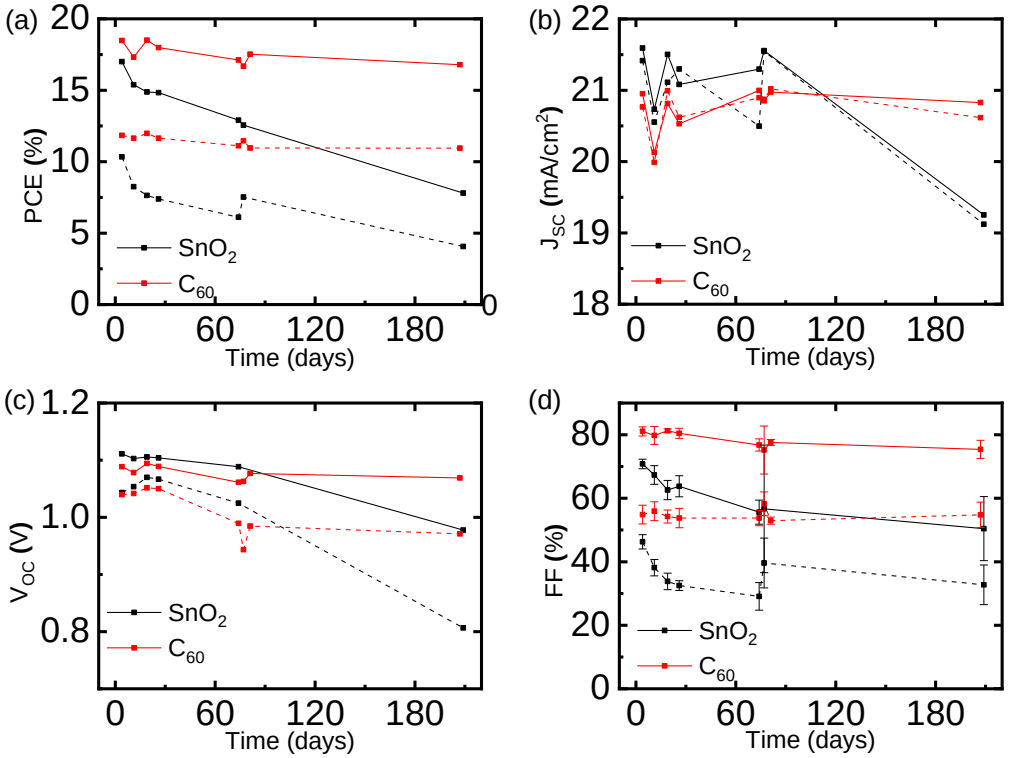

Figure 54. Average values of the *J-V* parameters of the reference and C_{60} devices (10 mg/ml), measured in the backward direction through a range of days: (a) PCE, (b) J_{SC} (c) V_{OC}, (d) FF. In dotted lines, the forward measurement.

In order to observe the stability of the device after illumination, constant power output measurements are done for 300 s (Figure 55a). The devices with thicker C_{60} layers are performing during the measurement with PCE above 16 %, confirming that solution processed C_{60} is an apt replacement for SnO_2, circumventing its disadvantages. Upon fabrication, the power conversion efficiency measured at a constant voltage over time remains over 16.2 % for the measured time frame (best cell: 17.1 %). Devices with the lower concentration (5 mg/ml) performed with a much lower PCE than its counterparts and the power conversion efficiency measured at a constant voltage over time drops to less than 10 % in a few minutes.

A comparison of the stabilized PCE upon fabrication and after different storage times can be seen in Figure 55a-c, with the results from the reference included as a control. In these measurements, the performance of the C_{60} devices (10, 15 and 20 mg/ml) remains constant, while the reference continues to diminish. In the devices with interlayers (Figure 47) a small

drop in performance is seen after 75 days, but in the devices where the SnO_2 is altogether removed from the architecture, the stabilized PCE is higher and stable for a longer time. The stable performance of the C_{60} devices after such a timeframe indicates that the degradation mechanisms are being retarded in devices with C_{60} as ETL.

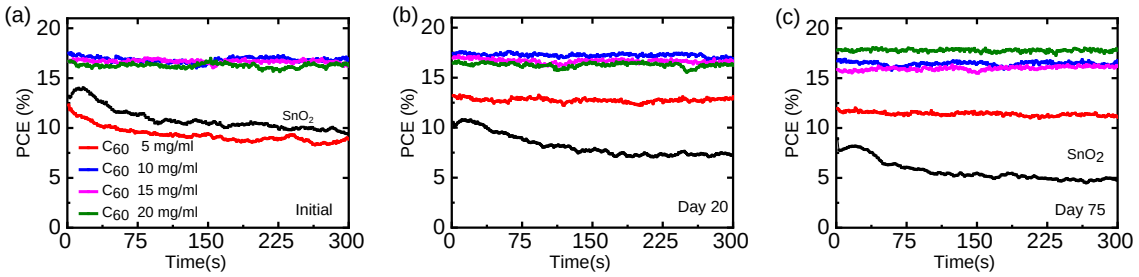

Figure 55. Evolution of the PCE of the devices with C_{60} as ETL measured at constant voltage upon fabrication (a), in day 20 (b) and day 75 (c). In black, the reference. The samples are stored between measurements in a nitrogen glovebox in the dark.

7.6. Temperature stability over time

During the implementation of the devices in real conditions, they can be subjected to a range of temperatures different than in the usual lab conditions. The *J-V* characteristic curve is *e.g.* measured at a constant temperature of 25°C. In real conditions, as the day starts, the temperatures can be cool, with temperatures rising in the midday and then cooling down again as night approaches. In this section, the impact of the temperature variation on performance is evaluated in three different architectures: SnO_2 as ETL, C_{60} as ETL and C_{60} as an interlayer.

The short-circuit current density (J_{SC}) of the selected devices is measured to evaluate their stability under a temperature cycle[18] (Figure 56a). The devices are measured from 10-60 °C in 5° C steps, from low to high temperatures and then low again following the progression in Figure 56 (in green). The evaluation under this temperature cycle shows how the short-circuit current density is affected by the variation of temperature and the stability of the samples under the correspondent cycle.

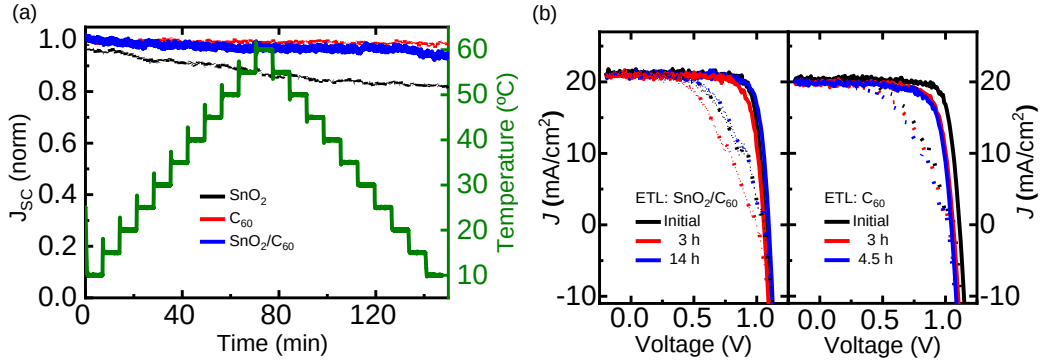

Figure 56. (a) Normalized short-circuit current density in perovskite solar cells with different ETLs under a temperature cycle (10 °C-60 °C, in steps of 5 °C, in green). (b) *J-V*

[18] The evaluation of the *J-V* and short-circuit current density under temperature variation was measured by Jonas Schwenzer.

characteristic curve of the C_{60} devices (as interlayer and as ETL) before, after the temperature cycle (3h), and after 4.5 and 14h.

During this measurement, the J_{SC} is heavily degraded in devices with SnO_2 as ETL, presenting a continuous decay during the measurement and losing 20 % of the initial value after the cycle. This reduction in the J_{SC} under temperature variation is related to an increase in the ion accumulation at the interface[18]. On the other hand, in devices with SnO_2 as ETL and C_{60} as interlayer (labeled SnO_2/C_{60}), a small loss can also be seen but it is significantly reduced (smaller than 4 % after the temperature cycle). Furthermore, in the devices with C_{60} as ETL, the J_{SC} remains constant during the measurement and the degradation of the short-circuit current can thus be avoided. In these cases, the presence of the C_{60} interlayer is then reducing the charge accumulation at the frontal interface and the series resistance in the *J-V* measurements, which is the main source of J_{SC} losses [18].

After measurement under the temperature cycle (Figure 56b), the *J-V* curve of the C_{60} devices is measured. The devices with C_{60} (either as ETL or as interlayer) presented recovery while the SnO_2 devices are no longer stable (not shown as the devices are no longer working). In this measurement, the devices with C_{60} interlayer presented an instant recovery and maintained its performance during 14h.

7.7. Discussion

Wojciechowski *et al*. state that DMF deposition on top of a C_{60} layer dissolves the layer [224] and proceed to build PSCs devices with evaporated MAPI. In this publication, they measured the UV-vis spectra of C_{60} layers before and after spin-coating DMF. However, using the method evaluated in this chapter, we have no evidence that the C_{60} layer is dissolved. Both in PL measurements (where the PL amplitude and lifetime are quenched in samples with C_{60}) and in the evaluation of the solar cells, the influence of the C_{60} layer is present. Furthermore, in the case that the C_{60} layer was, in fact, dissolved by the solvent in the perovskite solution, the devices would not have an ETL, leading towards performance with very low power conversion efficiencies. In the experiments here executed, the results are the opposite: the devices perform with increased efficiency and stability. It can be stated then, that with this fabrication method, the C_{60} layer remains in the solar cell architecture after deposition of the perovskite solution.

Furthermore, a strong improvement in the performance and stability of the PSCs is achieved when SnO_2 is replaced as ETL for C_{60}. The increased charge transport assist in the improvement of the electrical performance and a reduction in the hysteresis. The fast extraction of charges increases the PCE stability due to the reduction of charge accumulation in the frontal perovskite interface. Moreover, charge accumulation at the interface erodes the perovskite layer shortening the useful life.

Undesired accumulation of charges at the interface cause cumulative damage to the perovskite layer since the presence of non-extracted charges will break the perovskite crystal bonds. The breaking of the bonds will facilitate the formation of undesired components while eroding the perovskite layer. With SnO_2, perovskite layers fabricated with the same method suffered an accelerated degradation, indicating the PSC lifetime has to be evaluated in terms of the

interfaces that the perovskite layer is in contact. C_{60} as ETLs facilitates the charge transport and eliminates the charge accumulation, protecting the absorber from degradation in the process.

By controlling extraction layers and ensuring that charge extraction is executed properly, the lifetime of the perovskite device can be lengthened. As a result of this study, it can be stated that the ETL/perovskite interface is a governing factor in reduction of hysteresis and in the extension of the stability and life of the PSCs. It is then important to note, when doing degradation studies, not only to evaluate the performance of the perovskite layer but also the interaction with their extraction layers.

Conclusions

By means of different characterization methods, I have studied the optical properties and charge transport mechanisms in perovskites. Different deposition techniques modify the thin perovskite film properties and through optical characterization, the selection of the fabrication method that provides a better layer quality and a better performance in solar cells can be chosen.

Since the quality and morphology of the perovskite layer affect strongly the electrical performance, special care needs to be implemented to ensure that the layer quality is not affected when introducing changes to the architecture of the solar cell. Moreover, evaluation of the perovskite absorber alone is not sufficient for the determination of the electrical performance. Assessment of the interaction with the extraction layers and the contact between the interfaces is paramount for the evaluation of a material for the solar cell architecture. During the evaluation of these results, it can be concluded that interfaces are an important parameter of the cells that need to be controlled and carefully designed to obtain better electrical performance and delay the degradation. It is through the interfaces that the degradation mechanisms start damaging the perovskite layer, accelerating the degradation and reducing the solar cell life.

Even though light soaking can be seen as beneficial to the device performance, it is also a sign of photosensitive traps and of higher photoactive trap density. The light soaking phenomena is evidence of an increase in the number of non-radiative traps still present in the perovskite layer and in the long term can still impair the device.

Hysteresis in the devices can be reduced with an improvement of the contact between the extraction layers and the perovskite. In this dissertation, this was addressed with the introduction of passivating C_{60} layer, improving both power conversion efficiency and stability. Moreover, the improvement of the contact is directly related to better charge transport which will reduce undesired charge accumulation at the perovskite interfaces. Charge accumulation at the interfaces should be avoided, not only because it reduces the power conversion efficiency but also can cause cumulative damage to the perovskite layer since the presence of non-extracted charges will break the perovskite crystal bonds.

Further investigation can improve the perovskite interface with the hole transport layer. In this dissertation, Spiro is used as HTL, and the addition of interlayers between the perovskite and the HTL layer may improve the device power conversion efficiency. It also offers an opportunity to use a layer to insulate the cell from the environment and further protect it from degradation.

Using layers with hydrophobic properties may provide a solution to the perovskite sensitivity to moisture. An additional layer of carbon or C_{60} after gold evaporation may protect even further from any moisture infiltration into the cell, which may be one of the most damaging factors affecting the perovskite layer. Coffee grounds have been used to remove lead ions in drinking water due to their strong lead ion adsorption[225]. Adding the coffee grounds to the perovskite

solution can be used to reduce ion migration within the perovskite layer, increasing then the stability of the devices.

Another future approach can further evaluate the energy of the traps within perovskite devices and it would provide an accurate identification of the trap types a fabrication method creates. This can be executed through the combination of the characterizations included here with thermally stimulated current (TSC) or transient photocurrent/photovoltage (TPC/TPV). TSC is a powerful technique proven to identify the TPV/TPC is a technique used to extract the effective recombination mechanism on optoelectrical devices, which, alongside the photoluminescence measurements, would give an integral perspective on the dominant recombination on the complete solar cells.

Abbreviations

A	absorption
AFM	atomic force microscopy
CCD	charge-coupled device
CIGS	Cupper-indium-galium selenide, $CuIn_{1-x}Ga_xSe_2$
CTE	Charge transfer efficiency
DCB	1,2- dichlorobenzene
DMF	dimethylformamide
DMSO	dimethlysulfoxide
DSSC	dye-sensitized solar cell
E_g	Bandgap energy (also called bandgap)
EQE	external quantum efficiency
ETL	electron transport layer
FA	formamidinium, $NH_2CH=NH_2$
FF	fill factor
FTO	fluor-doped tin oxide
GBL	γ-butyrolactone
J_{SC}	short circuit current
HI	hysteresis index
HTL	hole transport layer
HTM	hole transport material
ICCD	intensified charge-coupled device
IPA	isopropanol
ITO	indium-doped tin oxide
I-V	current-voltage
J-V	current density-voltage
LS	light soaking
LTI	Light Technology Institute
MA	methylammonium (cation)
MAI	methylammonium iodide
MAPI	methlyammonium lead iodide
MPP	maximum power point
ND	neutral density
NREL	National Renewable Energy Laboratory
OMH	organometal halides
OPV	organic photovoltaics
PCBM	phenyl-C_{61}-butyric acid methyl ester
PCE	power conversion efficiency
PCEq	power conversion efficiency ratio (between backward and forward direction of measurement)
PL	Photoluminescence
PSC	Perovskite solar cells
PV	photovoltaics
R	reflection
RH	relative humidity
SC	Solar cell
SMU	Source measurement unit

SEM	scanning electron microscope
SPCE	Stabilized power conversion efficiency
Spiro	SpiroMeOTAD, 2,2,7,7-tetrakis-(N,N-di-p-methoxyphenylamine)-9,9-spirobifluorene
T	transmission
TA	transient absorption
trPL	time-resolved photoluminescence
V_{OC}	open circuit voltage
UV	ultraviolet
UV-Vis	ultraviolet-visible
XRD	X-ray Diffraction

Bibliography

[1] A. Kojima, K. Teshima, Y. Shirai, and T. Miyasaka, "Organometal halide perovskites as visible-light sensitizers for photovoltaic cells.," *J. Am. Chem. Soc.*, vol. 131, no. 17, pp. 6050–1, May 2009.

[2] S.-H. Turren-Cruz, A. Hagfeldt, and M. Saliba, "Methylammonium-free, high-performance and stable perovskite solar cells on a planar architecture," *Science*, vol. 362, pp. 449–453, 2018.

[3] Y. Wang, Y. Zhang, P. Zhang, and W. Zhang, "High intrinsic carrier mobility and photon absorption in the perovskite CH3NH3PbI3," *Phys. Chem. Chem. Phys.*, vol. 17, pp. 11516–11520, 2015.

[4] W.-J. Yin, T. Shi, and Y. Yan, "Unique Properties of Halide Perovskites as Possible Origins of the Superior Solar Cell Performance.," *Adv. Mater.*, pp. 1–6, May 2014.

[5] M. A. Green, Y. Jiang, A. Mahboubi, and A. Ho-baillie, "Optical Properties of Photovoltaic Organic – Inorganic Lead Halide Perovskites," *J. Phys. Chem. Lett.*, vol. 6, pp. 4774–4785, 2015.

[6] E. Edri, S. Kirmayer, M. Kulbak, G. Hodes, and D. Cahen, "Chloride Inclusion and Hole Transport Material Doping to Improve Methyl Ammonium Lead Bromide Perovskite-Based High Open- Circuit Voltage Solar Cells," 2014.

[7] X. Deng, X. Wen, S. Huang, R. Sheng, T. Harada, T. W. Kee, M. Green, and A. Ho-baillie, "Ultrafast Carrier Dynamics in Methylammonium Lead Bromide Perovskite," 2016.

[8] E. Edri, S. Kirmayer, D. Cahen, and G. Hodes, "High Open-Circuit Voltage Solar Cells Based on Organic-Inorganice Lead Bromide Perovskite," *J. Phys. Chem. Lett.*, vol. 4, pp. 897–902, 2013.

[9] N. Pellet, P. Gao, G. Gregori, T.-Y. Yang, M. K. Nazeeruddin, J. Maier, and M. Grätzel, "Mixed-organic-cation perovskite photovoltaics for enhanced solar-light harvesting.," *Angew. Chem. Int. Ed. Engl.*, vol. 53, no. 12, pp. 3151–7, Mar. 2014.

[10] Web of Science, "Web of Science [v.5.31] - Web of Science Core Collection Result Analysis." [Online]. Available: http://wcs.webofknowledge.com/RA/analyze.do?product=WOS&SID=F5rt3heCuRVoa4cOytq&field=PY_PublicationYear_PublicationYear_en&yearSort=true. [Accessed: 05-Dec-2018].

[11] "Czochralski Crystal Growth Process." [Online]. Available: https://www.tf.uni-kiel.de/matwis/amat/elmat_en/kap_6/illustr/i6_1_1.html. [Accessed: 18-Apr-2019].

[12] D. V. Morgan and K. Board, *An introduction to semiconductor microtechnology*. J. Wiley, 1990.

[13] A. L. Wani, A. Ara, and J. A. Usmani, "Lead toxicity: a review.," *Interdiscip. Toxicol.*, vol. 8, no. 2, pp. 55–64, Jun. 2015.

[14] Canadian Solar, “LIMITED WARRANTY STATEMENT PHOTOVOLTAIC MODULE PRODUCTS,” 2018.

[15] S. Venkatesan, F. Hao, J. Kim, Y. Rong, Z. Zhu, Y. Liang, J. Bao, and Y. Yao, “Moisture-driven phase transition for improved perovskite solar cells with reduced trap-state density,” *Nano Res.*, vol. 10, no. 4, pp. 1413–1422, 2017.

[16] M. Shirayama, M. Kato, T. Miyadera, T. Sugita, T. Fujiseki, S. Hara, H. Kadowaki, D. Murata, M. Chikamatsu, and H. Fujiwara, “Degradation mechanism of CH3NH3PbI3perovskite materials upon exposure to humid air,” *J. Appl. Phys.*, vol. 119, no. 11, 2016.

[17] W. R. Mateker and M. D. McGehee, “Progress in Understanding Degradation Mechanisms and Improving Stability in Organic Photovoltaics,” *Adv. Mater.*, vol. 29, no. 10, 2017.

[18] J. A. Schwenzer, L. Rakocevic, R. Gehlhaar, T. Abzieher, S. Gharibzadeh, S. Moghadamzadeh, A. Quintilla, B. S. Richards, U. Lemmer, and U. W. Paetzold, “Temperature Variation Induced Performance Decline of Perovskite Solar Cells,” *ACS Appl. Mater. Interfaces*, vol. 10, pp. 16390–16399, 2018.

[19] J. P. Bastos, U. W. Paetzold, R. Gehlhaar, W. Qiu, D. Cheyns, S. Surana, V. Spampinato, T. Aernouts, and J. Poortmans, “Light-Induced Degradation of Perovskite Solar Cells: The Influence of 4-Tert-Butyl Pyridine and Gold,” *Adv. Energy Mater.*, vol. 8, no. 23, pp. 1–9, 2018.

[20] W. F. (William F. Smith and J. Hashemi, *Foundations of materials science and engineering*. McGraw-Hill, 2010.

[21] A. K. Sood, J. W. Zeller, Y. R. Puri, C. Rouse, P. Haldar, H. Efstathiadis, N. K. Dhar, and P. S. Wijewarnasuriya, “SiGe focal plane array detector technology for near-infrared imaging,” *Int. J. Eng. Res. Technol.*, vol. 10, no. 1, pp. 81–103, 2017.

[22] M. Guarnieri, “More Light on Information [Historical],” *IEEE Ind. Electron. Mag.*, vol. 9, no. 4, pp. 58–61, Dec. 2015.

[23] A. Einstein, “Concerning an Heuristic Point of View Toward the Emission and Transformation of Light- Translation into English,” *Am. J. Phys.*, vol. 33, no. 5, 1965.

[24] A. Einstein, “Über einen die Erzeugung und Verwandlung des Lichtes betreffenden heuristischen Gesichtspunkt,” *Ann. Phys.*, vol. 17, no. 6, pp. 132–148, 1905.

[25] NREL, “Reference Air Mass 1.5 Spectra | Grid Modernization | NREL.” [Online]. Available: https://www.nrel.gov/grid/solar-resource/spectra-am1.5.html. [Accessed: 03-Apr-2019].

[26] Solar Cell Central, “P/N Junctions and Band Gaps.” [Online]. Available: http://solarcellcentral.com/junction_page.html. [Accessed: 03-Apr-2019].

[27] “Best Research-Cell Efficiency Chart | Photovoltaic Research | NREL.” [Online]. Available: https://www.nrel.gov/pv/cell-efficiency.html. [Accessed: 20-Feb-2019].

[28] J. Ramanujam and U. P. Singh, “Copper indium gallium selenide based solar cells – a review,” *Energy Environ. Sci.*, vol. 10, no. 6, pp. 1306–1319, Jun. 2017.

[29] A. A. Rockett, “Current status and opportunities in chalcopyrite solar cells,” *Curr. Opin. Solid State Mater. Sci.*, vol. 14, no. 6, pp. 143–148, Dec. 2010.

[30] M. Grätzel, “Dye-sensitized solar cells,” *J. Photochem. Photobiol. C Photochem. Rev.*, vol. 4,

no. 2, pp. 145–153, Oct. 2003.

[31] Y. Li, G. Xu, C. Cui, and Y. Li, “Flexible and Semitransparent Organic Solar Cells,” *Adv. Energy Mater.*, vol. 8, no. 7, p. 1701791, Mar. 2018.

[32] M. B. Schubert and J. H. Werner, “Flexible solar cells for clothing,” *Mater. Today*, vol. 9, no. 6, pp. 42–50, Jun. 2006.

[33] S. Fabric, “Solar Fabric and Solar Protective Fabric - Stay Powered Up With Solar Powered Textiles !” [Online]. Available: https://solarfabric.com/. [Accessed: 03-Apr-2019].

[34] B. O’Regan and M. Grätzel, “A low-cost, high-efficiency solar cell based on dye-sensitized colloidal TiO2 films,” *Nature*, vol. 353, pp. 737–740, 1991.

[35] C.-H. M. Chuang, P. R. Brown, V. Bulović, and M. G. Bawendi, “Improved performance and stability in quantum dot solar cells through band alignment engineering,” *Nat. Mater.*, vol. 13, no. 8, pp. 796–801, Aug. 2014.

[36] H. Choi, C. Nahm, J. Kim, C. Kim, S. Kang, T. Hwang, and B. Park, “Review paper: Toward highly efficient quantum-dot- and dye-sensitized solar cells,” *Curr. Appl. Phys.*, vol. 13, no. 2013, pp. S2–S13, Jul. 2013.

[37] H.-S. Kim, C.-R. Lee, J.-H. Im, K.-B. Lee, T. Moehl, A. Marchioro, S.-J. Moon, R. Humphry-Baker, J.-H. Yum, J. E. Moser, M. Grätzel, and N.-G. Park, “Lead iodide perovskite sensitized all-solid-state submicron thin film mesoscopic solar cell with efficiency exceeding 9%.,” *Sci. Rep.*, vol. 2, p. 591, Jan. 2012.

[38] X. Ziang, L. Shifeng, Q. Laixiang, P. Shuping, W. Wei, Y. Yu, Y. Li, C. Zhijian, W. Shufeng, D. Honglin, Y. Minghui, G. G. Qin, H. Chen, X. Pan, W. Liu, M. Cai, D. Kou, Z. Huo, X. Fang, S. Dai, H. Hu, J. Zhang, S. Lv, Y. Yu, F. Wei, T. Qin, H. Xu, Z. Liu, and G. Cui, “Refractive index and extinction coefficient of CH3NH3PbI3 studied by spectroscopic ellipsometry,” *Opt. Mater. Express*, vol. 5, no. 1, pp. 29–43, 2013.

[39] X. Zhu, D. Yang, R. Yang, B. Yang, Z. Yang, X. Ren, J. Zhang, J. Niu, J. Feng, and S. Liu, “Superior stability for perovskite solar cells with 20% efficiency using vacuum co-evaporation,” *Nanoscale*, vol. 9, no. 34, pp. 12316–12323, 2017.

[40] P. Pistor, J. Borchert, W. Fra, R. Csuk, and R. Scheer, “Monitoring the Phase Formation of Coevaporated Lead Halide Perovskite Thin Films by in Situ X‐ray Diffraction,” 2014.

[41] G. E. Eperon, V. M. Burlakov, P. Docampo, A. Goriely, and H. J. Snaith, “Morphological Control for High Performance, Solution-Processed Planar Heterojunction Perovskite Solar Cells,” *Adv. Funct. Mater.*, vol. 24, no. 1, pp. 151–157, Jan. 2014.

[42] F. Mathies, T. Abzieher, A. Hochstuhl, K. Glaser, A. Colsmann, U. W. Paetzold, and G. Hernandez-sosa, “Multipass inkjet printed planar methylammonium lead iodide perovskite solar cells,” *J. Mater. Chem. A Mater. energy Sustain.*, vol. 4, pp. 19207–19213, 2016.

[43] P. Qin, S. Tanaka, S. Ito, N. Tetreault, K. Manabe, H. Nishino, M. K. Nazeeruddin, and M. Grätzel, “Inorganic hole conductor-based lead halide perovskite solar cells with 12.4% conversion efficiency.,” *Nat. Commun.*, vol. 5, no. May 2014, p. 3834, Jan. 2014.

[44] J. H. Kim, S. T. Williams, N. Cho, C.-C. Chueh, and A. K.-Y. Jen, “Enhanced Environmental

Stability of Planar Heterojunction Perovskite Solar Cells Based on Blade-Coating," *Adv. Energy Mater.*, vol. 5, no. 4, p. 1401229, Feb. 2015.

[45] J. Xing, Y. Zhao, M. Askerka, L. N. Quan, X. Gong, W. Zhao, J. Zhao, H. Tan, G. Long, L. Gao, Z. Yang, O. Voznyy, J. Tang, Z.-H. Lu, Q. Xiong, and E. H. Sargent, "Color-stable highly luminescent sky-blue perovskite light-emitting diodes," *Nat. Commun. 2018 91*, vol. 9, no. 1, p. 3541, Aug. 2018.

[46] P. Brenner, M. Stulz, D. Kapp, T. Abzieher, U. W. Paetzold, A. Quintilla, I. a. Howard, H. Kalt, and U. Lemmer, "Highly stable solution processed metal-halide perovskite lasers on nanoimprinted distributed feedback structures SI," *Appl. Phys. Lett.*, vol. 109, no. 14, pp. 4–7, 2016.

[47] H. Kim, S. H. Im, and N. Park, "Organolead Halide Perovskite: New Horizons in Solar Cell Research," 2014.

[48] I. Grinberg, D. V. West, M. Torres, G. Gou, D. M. Stein, L. Wu, G. Chen, E. M. Gallo, A. R. Akbashev, P. K. Davies, J. E. Spanier, and A. M. Rappe, "Perovskite oxides for visible-light-absorbing ferroelectric and photovoltaic materials.," *Nature*, vol. 503, no. 7477, pp. 509–12, Nov. 2013.

[49] B. V Lotsch, "New light on an old story: perovskites go solar.," *Angew. Chem. Int. Ed. Engl.*, vol. 53, no. 3, pp. 635–7, Jan. 2014.

[50] P. P. Boix, K. Nonomura, N. Mathews, and S. G. Mhaisalkar, "Current progress and future perspectives for organic/inorganic perovskite solar cells," *Mater. Today*, vol. 17, no. 1, pp. 16–23, Jan. 2014.

[51] Z. Shi and A. H. Jayatissa, "Perovskites-based solar cells: A review of recent progress, materials and processing methods," *Materials (Basel).*, vol. 11, no. 5, 2018.

[52] F. Di Giacomo, S. Razza, F. Matteocci, A. D'Epifanio, S. Licoccia, T. M. Brown, and A. Di Carlo, "High efficiency CH3NH3PbI(3-x)Clx perovskite solar cells with poly(3-hexylthiophene) hole transport layer," *J. Power Sources*, vol. 251, pp. 152–156, Apr. 2014.

[53] T. Leijtens, G. E. Eperon, S. Pathak, A. Abate, M. M. Lee, and H. J. Snaith, "Overcoming ultraviolet light instability of sensitized TiO2 with meso-superstructured organometal tri-halide perovskite solar cells.," *Nat. Commun.*, vol. 4, p. 2885, Dec. 2013.

[54] G. Niu, W. Li, F. Meng, L. Wang, H. Dong, and Y. Qiu, "Study on the stability of CH3NH3PbI3 films and the effect of post-modification by aluminum oxide in all-solid-state hybrid solar cells," *J. Mater. Chem. A*, vol. 2, no. 3, p. 705, 2014.

[55] D. Liu and T. L. Kelly, "Perovskite solar cells with a planar heterojunction structure prepared using room-temperature solution processing techniques," *Nat. Photonics*, no. December, pp. 1–6, Dec. 2013.

[56] Q. Chen, H. Zhou, Z. Hong, S. Luo, H. Duan, H. Wang, Y. Liu, G. Li, and Y. Yang, "Planar Heterojunction Perovskite Solar Cells via Vapor-Assisted Solution Process," *J. Am. Chem. Soc.*, vol. 136, no. Scheme 1, pp. 622–625, 2014.

[57] M. M. Lee, J. Teuscher, T. Miyasaka, T. N. Murakami, and H. J. Snaith, "Efficient Hybrid Solar Cells Based on Meso-Superstructured Organometal Halide Perovskites," *Science (80-.).*, vol. 338, no. (6107), pp. 643–647, 2012.

[58] C. H. Nh, P. Cl, Q. Chen, H. Zhou, Y. Fang, A. Z. Stieg, T. Song, H. Wang, X. Xu, Y. Liu, S. Lu, J. You, P. Sun, J. Mckay, M. S. Goorsky, and Y. Yang, "The optoelectronic role of chlorine in

CH3NH3PbI3-based perovskite solar cells," *Nat. Commun.*, vol. 6, pp. 1–9, 2015.

[59] S. Zhang, X. Yang, Y. Numata, and L. Han, "Highly efficient dye-sensitized solar cells: progress and future challenges," *Energy Environ. Sci.*, vol. 6, no. 5, p. 1443, 2013.

[60] D. B. Liu, G. Wang, F. Wu, R. Wu, T. Chen, B. F. Ding, and Q. L. Song, "Crystallization process of perovskite modified by adding lead acetate in precursor solution for better morphology and higher device efficiency," *Org. Electron. physics, Mater. Appl.*, vol. 43, no. February, pp. 189–195, 2017.

[61] S. Colella, E. Mosconi, P. Fedeli, A. Listorti, F. Gazza, F. Orlandi, P. Ferro, T. Besagni, A. Rizzo, G. Calestani, G. Gigli, F. De Angelis, and R. Mosca, "MAPbI3-xClx mixed halide perovskite for hybrid solar cells: The role of chloride as dopant on the transport and structural properties," 2013.

[62] T. Ng, C. Chan, M. Lo, Q. Guan, and C. Lee, "Formation chemistry of perovskites with mixed iodide/chloride content and the implications on charge transport properties," *J. Mater. Chem. A Mater. energy Sustain.*, vol. 3, pp. 9081–9085, 2015.

[63] M. Grätzel, "The light and shade of perovskite solar cells," *Nat. Mater.*, vol. 13, no. 9, pp. 838–842, Aug. 2014.

[64] G. Grancini, S. Marras, M. Prato, C. Giannini, C. Quarti, F. De Angelis, M. De Bastiani, G. E. Eperon, H. J. Snaith, L. Manna, and A. Petrozza, "The Impact of the Crystallization Processes on the Structural and Optical Properties of Hybrid Perovskite Films for Photovoltaics," *J. Phys. Chem. Lett.*, vol. 5, pp. 3839–3842, 2014.

[65] Y. Deng, Q. Dong, C. Bi, Y. Yuan, and J. Huang, "Air-Stable, Efficient Mixed-Cation Perovskite Solar Cells with Cu Electrode by Scalable Fabrication of Active Layer," *Adv. Energy Mater.*, vol. 6, no. 11, p. 1600372, Jun. 2016.

[66] D. P. McMeekin, G. Sadoughi, W. Rehman, G. E. Eperon, M. Saliba, M. T. Horantner, A. Haghighirad, N. Sakai, L. Korte, B. Rech, M. B. Johnston, L. M. Herz, and H. J. Snaith, "A mixed-cation lead mixed-halide perovskite absorber for tandem solar cells," *Science (80-.).*, vol. 351, no. 6269, pp. 151–155, Jan. 2016.

[67] M. Saliba, T. Matsui, J.-Y. Seo, K. Domanski, J.-P. Correa-Baena, M. K. Nazeeruddin, S. M. Zakeeruddin, W. Tress, A. Abate, A. Hagfeldt, and M. Grätzel, "Cesium-containing triple cation perovskite solar cells: improved stability, reproducibility and high efficiency," *Energy Environ. Sci.*, vol. 9, no. 6, pp. 1989–1997, 2016.

[68] B. Suarez, V. Gonzalez-pedro, T. S. Ripolles, R. S. Sanchez, L. Otero, and I. Mora-sero, "Recombination Study of Combined Halides (Cl, Br, I) Perovskite Solar Cells," 2014.

[69] C. C. Stoumpos, C. D. Malliakas, and M. G. Kanatzidis, "Semiconducting tin and lead iodide perovskites with organic cations: phase transitions, high mobilities, and near-infrared photoluminescent properties.," *Inorg. Chem.*, vol. 52, no. 15, pp. 9019–38, Aug. 2013.

[70] F. Hao, C. C. Stoumpos, D. H. Cao, R. P. H. Chang, and M. G. Kanatzidis, "Lead-free solid-state organic–inorganic halide perovskite solar cells," *Nat. Photonics*, no. May, May 2014.

[71] N. K. Noel, S. D. Stranks, A. Abate, C. Wehrenfennig, S. Guarnera, A.-A. Haghighirad, A. Sadhanala, G. E. Eperon, S. K. Pathak, M. B. Johnston, A. Petrozza, L. M. Herz, and H. J. Snaith, "Lead-Free Organic-Inorganic Tin Halide Perovskites for Photovoltaic Applications," *Energy Environ. Sci.*, vol. 7, pp. 3061–3068, 2014.

[72] M. H. Kumar, S. Dharani, W. L. Leong, P. P. Boix, R. R. Prabhakar, T. Baikie, C. Shi, H. Ding, R. Ramesh, M. Asta, M. Graetzel, S. G. Mhaisalkar, and N. Mathews, "Lead-Free Halide Perovskite Solar Cells with High Photocurrents Realized Through Vacancy Modulation," *Adv. Mater.*, p. n/a-n/a, Sep. 2014.

[73] M. Konstantakou and T. Stergiopoulos, "A critical review on tin halide perovskite solar cells," *J. Mater. Chem. A*, vol. 5, no. 23, pp. 11518–11549, 2017.

[74] A. Marchioro, J. Teuscher, D. Friedrich, M. Kunst, R. van de Krol, T. Moehl, M. Grätzel, and J.-E. Moser, "Unravelling the mechanism of photoinduced charge transfer processes in lead iodide perovskite solar cells," *Nat. Photonics*, no. January 2014, pp. 1–6, Jan. 2014.

[75] T. Leitjens, S. D. Stranks, G. E. Eperon, R. Lindblad, E. M. J. Johansson, J. M. Ball, M. M. Lee, H. J. Snaith, and I. J. Mcpherson, "Electronic Properties of Meso-Superstructured and Planar Organometal Halide Perovskite Films : Charge Trapping, Photodoping, and Carrier Mobility," *ACS Nano*, vol. 8, no. 7, pp. 7147–7155, 2014.

[76] Z. Ku, Y. Rong, M. Xu, T. Liu, and H. Han, "Full printable processed mesoscopic CH3NH3PbI3/TiO2 heterojunction solar cells with carbon counter electrode.," *Sci. Rep.*, vol. 3, p. 3132, Jan. 2013.

[77] Y. Da, Y. Xuan, and Q. Li, "Quantifying energy losses in planar perovskite solar cells," *Sol. Energy Mater. Sol. Cells*, vol. 174, no. September 2017, pp. 206–213, 2018.

[78] X. Huang, Z. Hu, J. Xu, P. Wang, L. Wang, J. Zhang, and Y. Zhu, "Low-temperature processed SnO2compact layer by incorporating TiO2layer toward efficient planar heterojunction perovskite solar cells," *Sol. Energy Mater. Sol. Cells*, vol. 164, no. February, pp. 87–92, 2017.

[79] S.-M. Yong, N. Tsvetkov, L. Larina, B. T. Ahn, and D. K. Kim, "Ultrathin SnO2 layer for efficient carrier collection in dye-sensitized solar cells," *Thin Solid Films*, pp. 6–11, Jan. 2014.

[80] W. Li, J. Li, L. Wang, G. Niu, R. Gao, and Y. Qiu, "Post modification of perovskite sensitized solar cells by aluminum oxide for enhanced performance," *J. Mater. Chem. A*, vol. 1, no. 38, p. 11735, 2013.

[81] E. Edri, S. Kirmayer, A. Henning, S. Mukhopadhyay, K. Gartsman, Y. Rosenwaks, G. Hodes, and D. Cahen, "Why Lead Methylammonium Tri-Iodide Perovskite-Based Solar Cells Require a Mesoporous Electron Transporting Scaffold (but Not Necessarily a Hole Conductor)," 2014.

[82] G. E. Eperon, V. M. Burlakov, A. Goriely, and H. J. Snaith, "Neutral color semitransparent microstructured perovskite solar cells.," *ACS Nano*, vol. 8, no. 1, pp. 591–8, Jan. 2014.

[83] J. Burschka, N. Pellet, S.-J. Moon, R. Humphry-Baker, P. Gao, M. K. Nazeeruddin, and M. Grätzel, "Sequential deposition as a route to high-performance perovskite-sensitized solar cells.," *Nature*, vol. 499, no. 7458, pp. 316–9, Jul. 2013.

[84] I. Chung, B. Lee, J. He, R. P. H. Chang, and M. G. Kanatzidis, "All-solid-state dye-sensitized solar cells with high efficiency.," *Nature*, vol. 485, no. 7399, pp. 486–9, May 2012.

[85] M. Liu, M. B. Johnston, and H. J. Snaith, "Efficient planar heterojunction perovskite solar cells by vapour deposition," *Nature*, vol. 501, no. 7467, pp. 395–398, Sep. 2013.

[86] D. Liu, M. K. Gangishetty, and T. L. Kelly, "Effect of CH3NH3PbI3 Thickness on Device Efficiency in Planar Heterojunction Perovskite Solar Cells," *J. Mater. Chem. A*, vol. 2, pp.

19873–19881, Oct. 2014.

[87] X. Wang, X. Li, G. Tang, L. Zhao, W. Zhang, T. Jiu, and J. Fang, "Improving efficiency of planar hybrid CH 3 NH 3 PbI 3 - x Cl x perovskite solar cells by isopropanol solvent treatment," *Org. Electron.*, vol. 24, no. May, pp. 1–7, 2015.

[88] C. Tao, J. Van Der Velden, L. Cabau, N. F. Montcada, S. Neutzner, A. R. Srimath Kandada, S. Marras, L. Brambilla, M. Tommasini, W. Xu, R. Sorrentino, A. Perinot, M. Caironi, C. Bertarelli, E. Palomares, and A. Petrozza, "Fully Solution-Processed n–i–p-Like Perovskite Solar Cells with Planar Junction: How the Charge Extracting Layer Determines the Open-Circuit Voltage," *Adv. Mater.*, vol. 29, no. 15, 2017.

[89] W. Yang, Y. Yao, C. Wu, W. Yang, Y. Yao, and C. Wu, "Origin of the high open circuit voltage in planar heterojunction perovskite solar cells : Role of the reduced bimolecular recombination Origin of the high open circuit voltage in planar heterojunction perovskite solar cells : Role of the reduced bimolecul," vol. 095502, no. May, pp. 0–7, 2015.

[90] E. H. Anaraki, A. Kermanpur, L. Steier, K. Domanski, T. Matsui, W. Tress, M. Saliba, A. Abate, M. Grätzel, A. Hagfeldt, and J. P. Correa-Baena, "Highly efficient and stable planar perovskite solar cells by solution-processed tin oxide," *Energy Environ. Sci.*, vol. 9, no. 10, pp. 3128–3134, 2016.

[91] C. C. Boyd, R. Cheacharoen, T. Leijtens, and M. D. McGehee, "Understanding Degradation Mechanisms and Improving Stability of Perovskite Photovoltaics," *Chem. Rev.*, 2018.

[92] H. Zhang, C. Liang, Y. Zhao, M. Sun, H. Liu, J. Liang, D. Li, F. Zhang, and Z. He, "Dynamic interface charge governing the current – voltage hysteresis in perovskite," *Phys. Chem. Chem. Phys.*, vol. 17, pp. 9613–9618, 2015.

[93] Y. Zhao, A. M. Nardes, and K. Zhu, "Solid-State Mesostructured Perovskite CH3NH3PbI3 Solar Cells: Charge Transport, Recombination, and Diffusion Length," *J. Phys. Chem. Lett.*, vol. 5, pp. 490–494, 2014.

[94] Y. Rong, Z. Ku, A. Mei, T. Liu, M. Xu, S. Ko, X. Li, and H. Han, "Hole-Conductor-Free Mesoscopic TiO 2 /CH 3 NH 3 PbI 3 Heterojunction Solar Cells Based on Anatase Nanosheets and Carbon Counter Electrodes," pp. 2160–2164, 2014.

[95] S. Kazim, M. K. Nazeeruddin, M. Grätzel, and S. Ahmad, "Perovskite as light harvester: a game changer in photovoltaics.," *Angew. Chem. Int. Ed. Engl.*, vol. 53, no. 11, pp. 2812–24, Mar. 2014.

[96] Y. Chen, J. Peng, D. Su, X. Chen, and Z. Liang, "Efficient and Balanced Charge Transport Revealed in Planar Perovskite Solar Cells," *ACS Appl. Mater. Interfaces*, vol. 7, no. 8, pp. 4471–4475, Mar. 2015.

[97] A. Babayigit, A. Ethirajan, M. Muller, and B. Conings, "Toxicity of organometal halide perovskite solar cells," *Nat. Mater. 2016 153*, Feb. 2016.

[98] Y. Takahashi, R. Obara, Z.-Z. Lin, Y. Takahashi, T. Naito, T. Inabe, S. Ishibashi, and K. Terakura, "Charge-transport in tin-iodide perovskite CH3NH3SnI3: origin of high conductivity.," *Dalton Trans.*, vol. 40, no. 20, pp. 5563–8, May 2011.

[99] J. Liu, M. Ozaki, S. Yakumaru, T. Handa, R. Nishikubo, Y. Kanemitsu, A. Saeki, Y. Murata, R. Murdey, and A. Wakamiya, "Lead-Free Solar Cells based on Tin Halide Perovskite Films with High Coverage and Improved Aggregation," *Angew. Chemie - Int. Ed.*, vol. 57, no. 40,

pp. 13221–13225, 2018.

[100] A. Babayigit, D. Duy Thanh, A. Ethirajan, J. Manca, M. Muller, H.-G. Boyen, and B. Conings, "Assessing the toxicity of Pb- and Sn-based perovskite solar cells in model organism Danio rerio," *Sci. Rep.*, vol. 6, no. 1, p. 18721, May 2016.

[101] P. V. Kamat, J. Bisquert, and J. Buriak, "Toward Lead-Free Perovskite Solar Cells," *ACS Energy Lett.*, vol. 2, pp. 904–905, 2017.

[102] M. Chen, M.-G. Ju, A. D. Carl, Y. Zong, R. L. Grimm, J. Gu, X. C. Zeng, Y. Zhou, and N. P. Padture, "Cesium Titanium(IV) Bromide Thin Films Based Stable Lead-free Perovskite Solar Cells," *Joule*, vol. 2, no. 3, pp. 558–570, Mar. 2018.

[103] A. D. Sheikh, A. Bera, M. A. Haque, R. B. Rakhi, S. Del Gobbo, H. N. Alshareef, and T. Wu, "Atmospheric effects on the photovoltaic performance of hybrid perovskite solar cells," *Sol. Energy Mater. Sol. Cells*, vol. 137, no. November, pp. 6–14, 2015.

[104] T. Leijtens, G. E. Eperon, N. K. Noel, S. N. Habisreutinger, A. Petrozza, and H. J. Snaith, "Stability of Metal Halide Perovskite Solar Cells," pp. 1–23, 2015.

[105] D. Wang, M. Wright, N. K. Elumalai, and A. Uddin, "Stability of perovskite solar cells," *Sol. Energy Mater. Sol. Cells*, vol. 147, pp. 255–275, 2016.

[106] O. Malinkiewicz, A. Yella, Y. H. Lee, G. M. Espallargas, M. Graetzel, M. K. Nazeeruddin, and H. J. Bolink, "Perovskite solar cells employing organic charge-transport layers," *Nat. Photonics*, no. December 2013, pp. 1–5, Dec. 2013.

[107] Y. Han, S. Meyer, Y. Dkhissi, K. Weber, J. M. Pringle, U. Bach, L. Spiccia, and Y.-B. Cheng, "Degradation observations of encapsulated planar $CH_3NH_3PbI_3$ perovskite solar cells at high temperatures and humidity," *J. Mater. Chem. A*, vol. 3, no. 15, pp. 8139–8147, Mar. 2015.

[108] B. Hailegnaw, S. Kirmayer, E. Edri, G. Hodes, and D. Cahen, "Rain on Methylammonium Lead Iodide Based Perovskites: Possible Environmental E ff ects of Perovskite Solar Cells," 2015.

[109] R. T. Ginting, M.-K. Jeon, K.-J. Lee, W.-Y. Jin, T.-W. Kim, and J.-W. Kang, "Degradation mechanism of planar-perovskite solar cells: correlating evolution of iodine distribution and photocurrent hysteresis," *J. Mater. Chem. A*, vol. 5, no. 9, pp. 4527–4534, 2017.

[110] P. H. Joshi, L. Zhang, I. M. Hossain, H. A. Abbas, R. Kottokkaran, S. P. Nehra, M. Dhaka, M. Noack, and V. L. Dalal, "The physics of photon induced degradation of perovskite solar cells," *AIP Adv.*, vol. 6, no. 11, 2016.

[111] P. Docampo and T. Bein, "A Long-Term View on Perovskite Optoelectronics," 2016.

[112] A. Mei, X. Li, L. Liu, Z. Ku, T. Liu, Y. Rong, M. Xu, M. Hu, J. Chen, Y. Yang, M. Grätzel, and H. Han, "A hole-conductor–free, fully printable mesoscopic perovskite solar cell with high stability," *Science (80-.).*, vol. 345, no. 6194, pp. 295–298, Jul. 2014.

[113] H. J. Snaith, A. Abate, J. M. Ball, G. E. Eperon, T. Leijtens, N. K. Noel, S. D. Stranks, J. T. W. Wang, K. Wojciechowski, and W. Zhang, "Anomalous hysteresis in perovskite solar cells," *J. Phys. Chem. Lett.*, vol. 5, no. 9, pp. 1511–1515, 2014.

[114] D. H. Song, M. H. Jang, M. H. Lee, and J. H. Heo, "A discussion on the origin and solutions of hysteresis in perovskite hybrid solar cells," 2016.

[115] Y. Wu, H. Shen, D. Walter, D. Jacobs, T. Duong, J. Peng, L. Jiang, Y. B. Cheng, and K. Weber, "On the Origin of Hysteresis in Perovskite Solar Cells," *Adv. Funct. Mater.*, vol. 26, no. 37, pp. 6807–6813, 2016.

[116] D. W. Miller, G. E. Eperon, E. T. Roe, C. W. Warren, H. J. Snaith, M. C. Lonergan, D. W. Miller, G. E. Eperon, E. T. Roe, C. W. Warren, and H. J. Snaith, "Defect states in perovskite solar cells associated with hysteresis and performance," vol. 153902, 2016.

[117] J. M. Azpiroz, E. Mosconi, J. Bisquert, and F. De Angelis, "Defect migration in methylammonium lead iodide and its role in perovskite solar cell operation," *Energy Environ. Sci.*, vol. 8, no. 7, pp. 2118–2127, 2015.

[118] O. Almora, I. Zarazua, E. Mas-Marza, I. Mora-Sero, J. Bisquert, and G. G. Garcia-Belmonte, "Capacitive Dark Currents, Hysteresis, and Electrode Polarization in Lead Halide Perovskite Solar Cells," *J. Phys. Chem. Lett.*, pp. 1645–1652, 2015.

[119] E. Ghahremanirad, A. Bou, S. Olyaee, and J. Bisquert, "Inductive Loop in the Impedance Response of Perovskite Solar Cells Explained by Surface Polarization Model," *J. Phys. Chem. Lett.*, vol. 8, no. 7, pp. 1402–1406, 2017.

[120] H. Imran and N. Z. Butt, "Investigation of dominant hysteresis phenomenon in perovskite solar cell," *Conf. Rec. IEEE Photovolt. Spec. Conf.*, vol. 2016–Novem, pp. 776–780, 2016.

[121] D. A. Jacobs, Y. Wu, H. Shen, C. Barugkin, F. J. Beck, T. P. White, K. Weber, and K. R. Catchpole, "Hysteresis phenomena in perovskite solar cells: the many and varied effects of ionic accumulation," *Phys. Chem. Chem. Phys.*, vol. 19, no. 4, pp. 3094–3103, 2017.

[122] Y. C. Kim, N. J. Jeon, J. H. Noh, S. Yang, J. Seo, J. S. Yun, A. Ho-baillie, S. Huang, M. A. Green, J. Seidel, T. K. Ahn, S. Il Seok, C. W. V. Gmbh, and C. Kgaa, "Beneficial Effects of PbI 2 Incorporated in Organo-Lead Halide Perovskite Solar Cells," 2015.

[123] J. Y. Jeng, Y. F. Chiang, M. H. Lee, S. R. Peng, T. F. Guo, P. Chen, and T. C. Wen, "CH3NH3PbI3 perovskite/fullerene planar-heterojunction hybrid solar cells," *Adv. Mater.*, vol. 25, no. 27, pp. 3727–3732, 2013.

[124] J. Shi, X. Xu, D. Li, and Q. Meng, "Interfaces in Perovskite Solar Cells," no. 21, pp. 2472–2486, 2015.

[125] Y. Shao, Z. Xiao, C. Bi, Y. Yuan, and J. Huang, "Origin and elimination of photocurrent hysteresis by fullerene passivation in CH3NH3PbI3 planar heterojunction solar cells," *Nat. Commun.*, vol. 5, pp. 1–7, 2014.

[126] L. Kegelmann, C. M. Wol, C. Awino, F. Lang, E. L. Unger, L. Korte, T. Dittrich, D. Neher, B. Rech, and S. Albrecht, "It Takes Two to Tango-- Double-Layer Selective Contacts in Perovskite Solar Cells for Improved Device Performance and Reduced Hysteresis," *Appl. Mater. Interfaces*, vol. 9, pp. 17245–17255, 2017.

[127] T. H. Gfroerer, "Photoluminescence in Analysis of Surfaces and Interfaces," in *Encyclopedia of Analytical Chemistry*, R. A. Meyers, Ed. Chichester: John Wiley & Sons Ltd, 2000, pp. 9209–9231.

[128] "5. Laser Peak Fluence, Intensity and Peak Power - LIDARIS." [Online]. Available: http://lidaris.com/glossary-2/fluence/. [Accessed: 18-Dec-2018].

[129] G. Xing, N. Mathews, S. S. Lim, Y. M. Lam, S. Mhaisalkar, and T. C. Sum, "Long-range balanced electron- and hole-transport lengths in organic-inorganic CH3NH3PbI3.,"

Science, vol. 342, pp. 344–347, 2013.

[130] L. M. Herz, "Charge-Carrier Dynamics in Organic-Inorganic Metal Halide Perovskites," *Annu. Rev. Phys. Chem.*, vol. 67, no. 1, pp. 65–89, 2016.

[131] R. R. Chang, R. Iyer, and D. L. Lile, "Surface characterization of InP using photoluminescence," *J. Appl. Phys.*, vol. 61, no. 5, p. 1995, 1987.

[132] S. R. Scully and M. D. McGehee, "Effects of optical interference and energy transfer on exciton diffusion length measurements in organic semiconductors," *J. Appl. Phys.*, vol. 100, no. 3, p. 034907, 2006.

[133] P. E. Shaw, A. Ruseckas, and I. D. W. Samuel, "Exciton Diffusion Measurements in Poly(3-hexylthiophene)," *Adv. Mater.*, vol. 20, no. 18, pp. 3516–3520, Jul. 2008.

[134] D. Amans, O. Guillois, G. Ledoux, D. Porterat, and C. Reynaud, "Influence of light intensity on the photoluminescence of silicon nanostructures," *J. Appl. Phys.*, vol. 91, no. 8, p. 5334, 2002.

[135] S. D. Stranks, G. E. Eperon, G. Grancini, C. Menelaou, M. J. P. Alcocer, T. Leijtens, L. M. Herz, A. Petrozza, and H. J. Snaith, "Electron-Hole Diffusion Lengths Exceeding 1 Micrometer in an Organometal Trihalide Perovskite Absorber," *Science*, vol. 342, no. October, pp. 341–344, 2013.

[136] Y. Yamada, T. Nakamura, M. Endo, A. Wakamiya, and Y. Kanemitsu, "Photoelectronic Responses in Solution-Processed Studied by Photoluminescence and Photoabsorption Spectroscopy," vol. 5, no. 1, pp. 401–405, 2015.

[137] S. D. Stranks, V. M. Burlakov, T. Leijtens, J. M. Ball, A. Goriely, and H. J. Snaith, "Recombination Kinetics in Organic-Inorganic Perovskites: Excitons, Free Charge, and Subgap States," *Phys. Rev. Appl.*, vol. 2, no. 3, p. 034007, Sep. 2014.

[138] R. Chen, "Apparent stretched-exponential luminescence decay in crystalline solids," *J. Lumin.*, vol. 102–103, pp. 510–518, May 2003.

[139] S. Bai, Z. Wu, X. Wu, Y. Jin, N. Zhao, Z. Chen, Q. Mei, X. Wang, Z. Ye, T. Song, R. Liu, S. Lee, and B. Sun, "High-performance planar heterojunction perovskite solar cells: Preserving long charge carrier diffusion lengths and interfacial engineering," *Nano Res.*, vol. 7, no. 12, pp. 1749–1758, Aug. 2014.

[140] P. Docampo, F. Hanusch, S. D. Stranks, M. Döblinger, J. M. Feckl, M. Ehrensperger, N. K. Minar, M. B. Johnston, H. J. Snaith, and T. Bein, "Solution Deposition-Conversion for Planar Heterojunction Mixed Halide Perovskite Solar Cells," *Adv. Energy Mater.*, p. n/a-n/a, May 2014.

[141] J. R. Lakowicz, *Principles of Fluorescence Spectroscopy*, 3rd ed. Baltimore, Maryland, USA: Springer US.

[142] M. Cesaria, a P. Caricato, and M. Martino, "Realistic absorption coefficient of ultrathin films," *J. Opt.*, vol. 14, no. 10, p. 105701, Oct. 2012.

[143] M. Cesaria, a P. Caricato, and M. Martino, "Realistic absorption coefficient of each individual film in a multilayer architecture," *J. Opt.*, vol. 17, 2015.

[144] W. Shockely, "The Theory of p-n Junctions in Semiconductors and p-n Junction Transistors," *Bell Syst. Tech. J.*, vol. 28, no. 3, pp. 435–489, 1949.

[145] Ossila, “Solar Cells: A Guide to Theory and Measurement – Ossila.” [Online]. Available: https://www.ossila.com/pages/solar-cells-theory#theory. [Accessed: 29-Mar-2019].

[146] P. Würfel and Wiley InterScience (Online service), *Physics of solar cells : from principles to new concepts*. Weinheim, Germany: Wiley-VCH Verlag GmbH, 2005.

[147] H. J. Snaith, A. Abate, J. M. Ball, G. E. Eperon, T. Leijtens, N. K. Noel, S. D. Stranks, J. T. Wang, K. Wojciechowski, and W. Zhang, “Anomalous Hysteresis in Perovskite Solar Cells,” no. iii, 2014.

[148] W. Ananda, “External Quantum Efficiency Measurement of Solar Cell,” in *2017 15th International Conference on Quality in Research (QiR) : International Symposium on Electrical and Computer Engineering*, 2017, no. 1, pp. 450–456.

[149] A. H. M. Smets, K. Jäger, O. Isabella, R. A. van Swaaij, and M. Zeman, *Solar energy : the physics and engineering of photovoltaic conversion, technologies and systems*. UIT Cambridge Ltd., 2016.

[150] W. H. Bragg and W. L. Bragg, “The Reflection of X-rays by Crystals References,” *Proc. R. Soc. London*, vol. 88, pp. 428–438, 1913.

[151] “Spin Coating: A Guide to Theory and Techniques – Ossila.” [Online]. Available: https://www.ossila.com/pages/spin-coating#spin-coating-nanoparticles. [Accessed: 01-Mar-2019].

[152] A. Farooq, I. M. Hossain, S. Moghadamzadeh, J. A. Schwenzer, T. Abzieher, B. S. Richards, E. Klampaftis, and U. W. Paetzold, “Spectral Dependence of Degradation under Ultraviolet Light in Perovskite Solar Cells,” *ACS Appl. Mater. Interfaces*, vol. 10, pp. 21985–21990, 2018.

[153] R. S. Ruoff, D. S. Tse, R. Malhotra, and D. C. Lorents, “Solubility of fullerene (C60) in a variety of solvents,” *J. Phys. Chem.*, vol. 97, no. 13, pp. 3379–3383, 1993.

[154] S. Sun, T. Salim, N. Mathews, M. Duchamp, C. Boothroyd, G. Xing, T. C. Sum, and Y. M. Lam, “The origin of high efficiency in low-temperature solution-processable bilayer organometal halide hybrid solar cells,” *Energy Environ. Sci.*, vol. 7, no. 1, p. 399, 2014.

[155] K. F. Lin, S. H. Chang, K. H. Wang, H. M. Cheng, K. Y. Chiu, K. M. Lee, S. H. Chen, and C. G. Wu, “Unraveling the high performance of tri-iodide perovskite absorber based photovoltaics with a non-polar solvent washing treatment,” *Sol. Energy Mater. Sol. Cells*, vol. 141, pp. 309–314, 2015.

[156] D. B. Liu, G. Wang, F. Wu, R. Wu, T. Chen, B. F. Ding, and Q. L. Song, “Crystallization process of perovskite modified by adding lead acetate in precursor solution for better morphology and higher device efficiency,” *Org. Electron.*, vol. 43, no. February, pp. 189–195, 2017.

[157] H. Röhm, T. Leonhard, M. J. Hoffmann, and A. Colsmann, “Ferroelectric domains in methylammonium lead iodide perovskite thin-films,” *Energy Environ. Sci.*, vol. 10, no. 4, pp. 950–955, 2017.

[158] F. Mathies, T. Abzieher, A. Hochstuhl, K. Glaser, A. Colsmann, U. W. Paetzold, G. Hernandez-Sosa, U. Lemmer, and A. Quintilla, “Multipass inkjet printed planar methylammonium lead iodide perovskite solar cells,” *J. Mater. Chem. A*, vol. 4, no. 48, pp. 19207–19213, 2016.

[159] F. Mathies, H. Eggers, B. S. Richards, G. Hernandez-Sosa, U. Lemmer, and U. W. Paetzold, "Inkjet-Printed Triple Cation Perovskite Solar Cells," *ACS Appl. Energy Mater.*, p. acsaem.8b00222, Apr. 2018.

[160] H. Li, S. Li, Y. Wang, H. Sarvari, P. Zhang, M. Wang, and Z. Chen, "A modified sequential deposition method for fabrication of perovskite solar cells," *Sol. Energy*, vol. 126, pp. 243–251, 2016.

[161] T. Abzieher, F. Mathies, M. Hetterich, A. Welle, D. Gerthsen, U. Lemmer, U. W. Paetzold, and M. Powalla, "Additive-Assisted Crystallization Dynamics in Two-Step Fabrication of Perovskite Solar Cells," *Phys. status solidi*, vol. 214, no. 12, p. 1700509, Dec. 2017.

[162] O. Malinkiewicz, C. Roldán-Carmona, A. Soriano, E. Bandiello, L. Camacho, M. K. Nazeeruddin, and H. J. Bolink, "Metal-Oxide-Free Methylammonium Lead Iodide Perovskite-Based Solar Cells: the Influence of Organic Charge Transport Layers," *Adv. Energy Mater.*, p. n/a-n/a, Jun. 2014.

[163] H. J. Snaith, "Perovskites: The Emergence of a New Era for Low-Cost , High-Efficiency Solar Cells," *J. Phys. Chem. Lett.*, vol. 4, pp. 3623–3630, 2013.

[164] P.-H. Huang, Y.-H. Wang, J.-C. Ke, and C.-J. Huang, "The effect of solvents on the performance of CH3NH3PbI3 Perovskite Solar Cells," *Energies*, vol. 10, no. 5, p. 599, 2017.

[165] N. J. Jeon, J. H. Noh, Y. C. Kim, W. S. Yang, S. Ryu, and S. Il Seok, "Solvent engineering for high-performance inorganic–organic hybrid perovskite solar cells," *Nat. Mater.*, vol. 13, no. 9, pp. 897–903, Sep. 2014.

[166] K. Lin, S. Hsiung, K. Wang, H. Cheng, K. Yuan, K. Lee, S. Chen, and C. Wu, "Unraveling the high performance of tri-iodide perovskite absorber based photovoltaics with a non-polar solvent washing treatment," *Sol. Energy Mater. Sol. Cells*, vol. 141, pp. 309–314, 2015.

[167] W. Zhang, S. Pathak, N. Sakai, T. Stergiopoulos, P. K. Nayak, N. K. Noel, A. a. Haghighirad, V. M. Burlakov, D. W. deQuilettes, A. Sadhanala, W. Li, L. Wang, D. S. Ginger, R. H. Friend, and H. J. Snaith, "Enhanced optoelectronic quality of perovskite thin films with hypophosphorous acid for planar heterojunction solar cells," *Nat. Commun.*, vol. 6, no. May, p. 10030, 2015.

[168] A. Abrusci, S. D. Stranks, P. Docampo, H. L. Yip, A. K. Y. Jen, and H. J. Snaith, "High-performance perovskite-polymer hybrid solar cells via electronic coupling with fullerene monolayers," *Nano Lett.*, vol. 13, no. 7, pp. 3124–3128, 2013.

[169] J. M. Ball, M. M. Lee, A. Hey, and H. J. Snaith, "Low-temperature processed meso-superstructured to thin-film perovskite solar cells," *Energy Environ. Sci.*, vol. 6, no. 6, p. 1739, 2013.

[170] P. Docampo, J. M. Ball, M. Darwich, G. E. Eperon, and H. J. Snaith, "Efficient organometal trihalide perovskite planar-heterojunction solar cells on flexible polymer substrates.," *Nat. Commun.*, vol. 4, p. 2761, Jan. 2013.

[171] P. Brenner, M. Stulz, D. Kapp, T. Abzieher, U. W. Paetzold, A. Quintilla, I. a. Howard, H. Kalt, and U. Lemmer, "Highly stable solution processed metal-halide perovskite lasers on nanoimprinted distributed feedback structures," *Appl. Phys. Lett.*, vol. 109, no. 14, 2016.

[172] S. Luo and W. Daoud, "Crystal Structure Formation of CH3NH3PbI3-xClx Perovskite," *Materials (Basel).*, vol. 9, no. 12, p. 123, 2016.

[173] D. Wang, Z. Liu, Z. Zhou, H. Zhu, Y. Zhou, C. Huang, Z. Wang, H. Xu, Y. Jin, B. Fan, S. Pang,

and G. Cui, “Reproducible One-Step Fabrication of Compact MAPbI 3 − x Cl x Thin Films Derived from Mixed-Lead-Halide Precursors,” 2014.

[174] K. M. Lee, C.-C. Chen, L.-C. Chen, S. H. Chang, K. S. Chen, S. C. Yeh, C. T. Chen, and C. G. Wu, “Thickness effects of thermally evaporated C60 thin films on regular-type CH3NH3PbI3 based solar cells,” *Sol. Energy Mater. Sol. Cells*, vol. 164, no. February, pp. 13–18, 2017.

[175] G. Mihu, I. Mihalache, I. Graur, N. Watanabe, H. Jintoku, T. Sagawa, J. Park, Z. Wang, and D. Kwon, “Surface Free Energy and Wettability Determination of Various Fullerene Derivative Films on Amorphous Carbon Wafer Surface Free Energy and Wettability Determination of Various Fullerene Derivative Films on Amorphous Carbon Wafer,” *Jpn. J. Appl. Phys.*, vol. 47, no. 7, pp. 5730–5733, 2008.

[176] L.-C. Chen, Y.-S. Lin, P.-W. Tang, C.-Y. Tai, Z.-L. Tseng, J.-H. Lin, S.-H. Chen, and H.-C. Kuo, “Unraveling current hysteresis effects in regular-type C_{60} -$CH_3NH_3PbI_3$ heterojunction solar cells,” *Nanoscale*, vol. 2, pp. 17802–17806, 2017.

[177] D. Shin, D. Kang, J. Jeong, S. Park, M. Kim, H. Lee, and Y. Yi, “Unraveling the Charge Extraction Mechanism of Perovskite Solar Cells Fabricated with Two-Step Spin Coating: Interfacial Energetics between Methylammonium Lead Iodide and C60,” *J. Phys. Chem. Lett.*, vol. 8, no. 21, pp. 5423–5429, 2017.

[178] K. Zhang, H. Yu, X. Liu, Q. Dong, Z. Wang, Y. Wang, N. Chen, Y. Zhou, and B. Song, “Fullerenes and derivatives as electron transport materials in perovskite solar cells,” *Sci. China Chem.*, vol. 60, no. 1, pp. 144–150, 2017.

[179] A. Al Mamun, T. T. Ava, K. Zhang, H. Baumgart, and G. Namkoong, “New PCBM/carbon based electron transport layer for perovskite solar cells,” *Phys. Chem. Chem. Phys.*, vol. 19, no. 27, pp. 17960–17966, 2017.

[180] D. Liu, Q. Wang, C. J. Traverse, C. Yang, M. Young, P. S. Kuttipillai, S. Y. Lunt, T. W. Hamann, and R. R. Lunt, “Impact of Ultrathin C_{60} on Perovskite Photovoltaic Devices,” *ACS Nano*, p. acsnano.7b08561, 2018.

[181] K. Wojciechowski, T. Leijtens, S. Siprova, C. Schlueter, M. T. Ho, J. T. W. Wang, C. Z. Li, A. K. Y. Jen, T. L. Lee, H. J. Snaith, M. T. H??rantner, J. T. W. Wang, C. Z. Li, A. K. Y. Jen, T. L. Lee, H. J. Snaith, M. T. Hoerantner, J. T. W. Wang, C. Z. Li, A. K. Y. Jen, T. L. Lee, and H. J. Snaith, “C60 as an efficient n-type compact layer in perovskite solar cells,” *J. Phys. Chem. Lett.*, vol. 6, no. 12, pp. 2399–2405, 2015.

[182] A. Bera, A. D. Sheikh, M. A. Haque, R. Bose, E. Alarousu, O. F. Mohammed, and T. Wu, “Fast Crystallization and Improved Stability of Perovskite Solar Cells with Zn 2 SnO 4 Electron Transporting Layer: Interface Matters,” *Appl. Mater. Interfaces*, vol. 7, pp. 28404–28411, 2015.

[183] M. Xiao, F. Huang, W. Huang, Y. Dkhissi, Y. Zhu, J. Etheridge, A. Gray-Weale, U. Bach, Y.-B. Cheng, and L. Spiccia, “A Fast Deposition-Crystallization Procedure for Highly Efficient Lead Iodide Perovskite Thin-Film Solar Cells,” *Angew. Chemie*, vol. 126, no. 37, pp. 10056–10061, Sep. 2014.

[184] Y. Zhou, M. Yang, W. Wu, A. L. Vasiliev, K. Zhu, and N. P. Padture, “Room-Temperature Crystallization of Hybrid-Perovskite Thin Films via Solvent-Solvent Extraction for High-Performance Solar Cells,” *J. Mater. Chem. A*, vol. 3, pp. 8178–8184, 2015.

[185] X. Fang, Y. Wu, Y. Lu, Y. Sun, S. Zhang, J. Zhang, W. Zhang, N. Yuan, and J. Ding, “Annealing-

free perovskite films based on solvent engineering for efficient solar cells," *J. Mater. Chem. C*, vol. 5, no. 4, pp. 842–847, Jan. 2017.

[186] N. Ahn, D.-Y. Son, I.-H. Jang, S. Min Kang, M. Choi, and N.-G. Park, "Highly Reproducible Perovskite Solar Cells with Average Efficiency of 18.3% and Best Efficiency of 19.7% Fabricated via Lewis Base Adduct of Lead(II) Iodide," *J. Am. Chem. Soc*, vol. 137, p. 8699, 2015.

[187] J. Liu, C. Gao, X. He, Q. Ye, L. Ouyang, D. Zhuang, C. Liao, J. Mei, and W. Lau, "Improved Crystallization of Perovskite Films by Optimized Solvent Annealing for High Efficiency Solar Cell," 2015.

[188] Q. Dong, Y. Fang, Y. Shao, P. Mulligan, J. Qiu, L. Cao, and J. Huang, "Electron-hole diffusion lengths >175 mm in solution-grown CH3NH3PbI3 single crystals," *Science (80-.).*, vol. 347, no. 6225, p. 967, 2015.

[189] W. Zhang, S. Pathak, N. Sakai, T. Stergiopoulos, P. K. Nayak, N. K. Noel, A. A. Haghighirad, V. M. Burlakov, W. Dane, A. Sadhanala, W. Li, D. S. Ginger, R. H. Friend, and H. J. Snaith, "Enhanced optoelectronic quality of perovskite thin films with hypophosphorous acid for planar heterojunction solar cells," *Nat. Commun.*, vol. 6, no. May, pp. 1–9, 2015.

[190] A. Buin, P. Pietsch, J. Xu, O. Voznyy, A. H. Ip, R. Comin, and E. H. Sargent, "Materials Processing Routes to Trap-Free Halide Perovskites," *Nano Lett.*, vol. 14, pp. 6281–6286, 2014.

[191] J. Shi, H. Wei, S. Lv, X. Xu, H. Wu, Y. Luo, and D. Li, "Control of Charge Transport in the Perovskite CH 3 NH 3 PbI 3 Thin Film," pp. 842–847, 2015.

[192] P. Brenner, T. Glöckler, D. Rueda-Delgado, T. Abzieher, M. Jakoby, B. S. Richards, U. W. Paetzold, I. A. Howard, and U. Lemmer, "Triple cation mixed-halide perovskites for tunable lasers," *Opt. Mater. Express*, vol. 7, no. 11, 2017.

[193] W. Wang, H. Xu, J. Cai, J. Zhu, C. Ni, F. Hong, Z. Fang, F. Xu, S. Cui, R. Xu, L. Wang, F. Xu, J. Huang, Z. Xiao, C. Bi, Y. Shao, Q. Dong, Q. Wang, Y. Yuan, C. Wang, Y. Gao, and J. Huang, "Visible blind ultraviolet photodetector based on CH 3 NH 3 PbCl 3 thin film," *Opt. Express*, vol. 24, no. 8, 2016.

[194] Q. Chen, H. Zhou, Y. Fang, A. Z. Stieg, T.-B. Song, H.-H. Wang, X. Xu, Y. Liu, S. Lu, J. You, P. Sun, J. McKay, M. S. Goorsky, and Y. Yang, "The optoelectronic role of chlorine in CH3NH3PbI3-based perovskite solar cells," *Nat. Commun.*, vol. 6, pp. 1–9, 2015.

[195] T. Ng, C. Chan, M. Lo, Q. Guan, and C. Lee, "Formation chemistry of perovskites with mixed iodide / chloride content and the implications on charge transport properties," *J. Mater. Chem. A Mater. energy Sustain.*, vol. 3, pp. 1–5, 2014.

[196] R. A. Sasala and J. R. Sites, "Time dependent voltage in CuInSe/sub 2/ and CdTe solar cells," in *Conference Record of the Twenty Third IEEE Photovoltaic Specialists Conference - 1993 (Cat. No.93CH3283-9)*, pp. 543–548.

[197] F. Haug, D. Rudmann, H. Zogg, and A. N. Tiwari, "Light soaking effects in Cu (In , Ga) Se 2 superstrate solar cells," vol. 432, no. 03, pp. 431–435, 2003.

[198] C. Wehrenfennig, G. E. Eperon, M. B. Johnston, H. J. Snaith, and L. M. Herz, "High Charge Carrier Mobilities and Lifetimes in Organolead Trihalide Perovskites," *Adv. Mater.*, vol. 26, no. 10, pp. 1584–1589, Mar. 2014.

[199] K. Zheng, K. Zidek, M. Abdellah, M. E. Messing, M. J. Al-marri, and T. Pullerits, "Trap States

and Their Dynamics in Organometal Halide Perovskite Nanoparticles and Bulk Crystals Trap States and Their Dynamics in Organometal Halide Perovskite Nanoparticles and Bulk Crystals," 2016.

[200] X. Wu, M. T. Trinh, D. Niesner, H. Zhu, Z. Norman, J. S. Owen, O. Ya, B. J. Kudisch, and X. Zhu, "Trap States in Lead Iodide Perovskites," 2015.

[201] D. W. DeQuilettes, W. Zhang, V. M. Burlakov, D. J. Graham, T. Leijtens, A. Osherov, V. Bulović, H. J. Snaith, D. S. Ginger, and S. D. Stranks, "Photo-induced halide redistribution in organic-inorganic perovskite films," *Nat. Commun.*, vol. 7, no. May, 2016.

[202] Q. Dong, Y. Fang, Y. Shao, P. Mulligan, J. Qiu, L. Cao, and J. Huang, "SI Electron-hole diffusion lengths > 175 μm in solution-grown CH3NH3PbI3 single crystals," *Science (80-.).*, vol. 347, no. 6225, pp. 967–970, Jan. 2015.

[203] Y. Hou, S. Scheiner, X. Tang, N. Gasparini, M. Richter, N. Li, P. Schweizer, S. Chen, H. Chen, C. Omar, R. Quiroz, X. Du, G. J. Matt, A. Osvet, E. Spiecker, R. H. Fink, A. Hirsch, M. Halik, C. J. Brabec, C. O. R. Quiroz, X. Du, G. J. Matt, A. Osvet, E. Spiecker, R. H. Fink, A. Hirsch, M. Halik, and C. J. Brabec, "Suppression of Hysteresis Effects in Organohalide Perovskite Solar Cells," *Adv. Mater. Interfaces*, vol. 4, no. 1700007, pp. 1–9, 2017.

[204] H. Zhang, C. Liang, Y. Zhao, M. Sun, H. Liu, J. Liang, D. Li, F. Zhang, and Z. He, "Dynamic interface charge governing the current–voltage hysteresis in perovskite solar cells," *Phys. Chem. Chem. Phys.*, vol. 17, no. 15, pp. 9613–9618, 2015.

[205] E. L. Unger, E. T. Hoke, C. D. Bailie, W. H. Nguyen, A. R. Bowring, T. Heumuller, M. G. Christoforo, and M. D. McGehee, "Hysteresis and transient behavior in current-voltage measurements of hybrid-perovskite absorber solar cells," *Energy Environ. Sci.*, Aug. 2014.

[206] J. M. Azpiroz, E. Mosconi, J. Bisquert, and F. De Angelis, "Environmental Science and its role in perovskite solar cell operation †," *Energy Environ. Sci.*, vol. 8, pp. 2118–2127, 2015.

[207] W. Tress, N. Marinova, T. Moehl, S. M. Zakeeruddin, N. Mohammad K., M. Grätzel, M. K. Nazeeruddin, and M. Grätzel, "Understanding the rate-dependent J–V hysteresis, slow time component, and aging in CH 3 NH 3 PbI 3 perovskite solar cells: the role of a compensated electric field," *Energy Environ. Sci.*, vol. 8, no. 3, pp. 995–1004, 2015.

[208] W. Nie, H. Tsai, R. Asadpour, A. J. Neukirch, G. Gupta, J. J. Crochet, M. Chhowalla, S. Tretiak, M. a. Alam, H.-L. H. Wang, J.-C. Blancon, A. J. Neukirch, G. Gupta, J. J. Crochet, M. Chhowalla, S. Tretiak, M. a. Alam, H.-L. H. Wang, and a. D. Mohite, "High-efficiency solution-processed perovskite solar cells with millimeter-scale grains," *Science*, vol. 347, no. 6221, pp. 522–525, 2015.

[209] J. Duan, Q. Xiong, B. Feng, Y. Xu, J. Zhang, and H. Wang, "Low-temperature processed SnO2 compact layer for efficient mesostructure perovskite solar cells," *Appl. Surf. Sci.*, vol. 391, pp. 677–683, 2017.

[210] E. J. Juarez-Perez, M. Wu, F. Fabregat-Santiago, K. Lakus-Wollny, E. Mankel, T. Mayer, W. Jaegermann, and I. Mora-sero, "Role of the Selective Contacts in the Performance of Lead Halide Perovskite Solar Cells," *J. Phys. Chem. Lett.*, vol. 5, pp. 680–685, 2014.

[211] F. Xu, J. Zhu, R. Cao, S. Ge, W. Wang, H. Xu, R. Xu, Y. Wu, M. Gao, Z. Ma, F. Hong, and Z. Jiang, "Elucidating the evolution of the current-voltage characteristics of planar organometal halide perovskite solar cells to an S-shape at low temperature," *Sol. Energy Mater. Sol.*

Cells, vol. 157, pp. 981–988, 2016.

[212] M. F. Aygüler, A. G. Hufnagel, P. Rieder, M. Wussler, W. Jaegermann, T. Bein, V. Dyakonov, M. L. Petrus, A. Baumann, and P. Docampo, "Influence of Fermi Level Alignment with Tin Oxide on the Hysteresis of Perovskite Solar Cells," *ACS Appl. Mater. Interfaces*, p. acsami.8b00990, 2018.

[213] T. Gatti, E. Menna, M. Meneghetti, M. Maggini, A. Petrozza, and F. Lamberti, "The Renaissance of fullerenes with perovskite solar cells," *Nano Energy*, vol. 41, pp. 84–100, Nov. 2017.

[214] P. Pistor, J. Borchert, W. Fränzel, R. Csuk, and R. Scheer, "Monitoring the Phase Formation of Coevaporated Lead Halide Perovskite Thin Films by in Situ X-ray Diffraction," *J. Phys. Chem. Lett.*, vol. 5, no. 19, pp. 3308–3312, Oct. 2014.

[215] L. M. Herz, "Charge Carrier Dynamics in Organic-Inorganic Metal Halide Perovskites," *arXiv*, no. February, pp. 1–26, 2015.

[216] P.-W. Liang, C.-Y. Liao, C.-C. Chueh, F. Zuo, S. T. Williams, X.-K. Xin, J. Lin, and A. K.-Y. Jen, "Additive Enhanced Crystallization of Solution-Processed Perovskite for Highly Efficient Planar-Heterojunction Solar Cells.," *Adv. Mater.*, pp. 1–7, Mar. 2014.

[217] L. Xiong, Y. Guo, J. Wen, H. Liu, G. Yang, P. Qin, and G. Fang, "Review on the Application of SnO2 in Perovskite Solar Cells," *Adv. Funct. Mater.*, vol. 28, no. 35, pp. 1–18, 2018.

[218] N. Aristidou, C. Eames, I. Sanchez-Molina, X. Bu, J. Kosco, M. S. Islam, and S. A. Haque, "Fast oxygen diffusion and iodide defects mediate oxygen-induced degradation of perovskite solar cells," *Nat. Commun.*, vol. 8, p. 15218, May 2017.

[219] G. Santarossa, K. Hahn, and A. Baiker, "Free Energy and Electronic Properties of Water Adsorption on the SnO_2 (110) Surface," *Langmuir*, vol. 29, no. 18, pp. 5487–5499, May 2013.

[220] R. Zangi, "Are Buckyballs Hydrophobic?," *J. Phys. Chem. B*, vol. 118, p. 37, 2014.

[221] Q. Chen, H. Zhou, T. Bin Song, S. Luo, Z. Hong, H. S. Duan, L. Dou, Y. Liu, and Y. Yang, "Controllable self-induced passivation of hybrid lead iodide perovskites toward high performance solar cells," *Nano Lett.*, vol. 14, no. 7, pp. 4158–4163, 2014.

[222] D. Bi, W. Tress, M. I. Dar, P. Gao, J. Luo, C. Renevier, K. Schenk, A. Abate, F. Giordano, J. C. Baena, J. Decoppet, S. M. Zakeeruddin, M. K. Nazeeruddin, M. Grätzel, and A. Hagfeldt, "Efficient luminescent solar cells based on tailored mixed-cation perovskites," no. January, 2016.

[223] G. N. Advani, P. Kluge-Weiss, R. L. Longini, and A. G. Jordan, "Oxygen vacancy diffusion in SnO2 thin films," *Int. J. Electron. Theor. Exp.*, vol. 48, no. 5, pp. 403–411, 1980.

[224] K. Wojciechowski, T. Leijtens, S. Siprova, C. Schlueter, M. T. Ho, J. T. Wang, C. Li, A. K. Jen, T. Lee, and H. J. Snaith, "C60 as an E fficient n - type compact layer in Perovskite Solar Cells," 2015.

[225] T. Tokimoto, N. Kawasaki, T. Nakamura, J. Akutagawa, and S. Tanada, "Removal of lead ions in drinking water by coffee grounds as vegetable biomass," *J. Colloid Interface Sci.*, vol. 281, no. 1, pp. 56–61, 2005.

[226] Fraunhofer ISE, "PHOTOVOLTAICS REPORT," 2019.

List of Figures

List of Tables

Publication list

Papers

- **D. Rueda-Delgado**, I. Hossain, M. Jakoby, J. Schwenzer, I. Howard, U. Lemmer, and U. W. Paetzold. *Solution-processed and evaporated C_{60} interlayers in perovskite photovoltaics.* **Submitted.**
- J. A. Schwenzer, L. Rakocevic, T. Abzieher, **D. Rueda-Delgado**, S. Moghadamzadeh, S. Gharibzadeh, I. Hossain, R. Gehlhaar, B. Richards, U. Lemmer, and U. Paetzold. *Towards stable perovskite solar cell architectures: Robustness against temperature variations under real world conditions.* **Submitted.**
- I. Hossain, D. Hudry, F. Mathies, T. Abzieher, S. Moghadamzadeh, **D. Rueda-Delgado**, F. Schackmar, M. Bruns, R. Andriessen, T. Aernouts, F. Giacomo, U. Lemmer, B. Richards, U. Paetzold and A. Hadipour. *Scalable Processing of Low Temperature TiO_2 Nanoparticles for High Efficiency Perovskite Solar Cell.* ACS Appl. Energy Mater. **2019**, 2, 1, 47-58. https://doi.org/10.1021/acsaem.8b01567
- J. Schwenzer, L. Rakocevic, T. Abzieher, **D. Rueda-Delgado**, R. Gehlhaar, B. Richards, U. Lemmer, and U. Paetzold. *Stable Perovskite Solar Cell Architectures: Robustness against Temperature Variations Under Real World Conditions.* Conference: 2018 IEEE 7th World Conference on Photovoltaic Energy Conversion (WCPEC) (A Joint Conference of 45th IEEE PVSC, 28th PVSEC & 34th EU PVSEC) https://doi.org/10.1109/PVSC.2018.8547781
- P. Brenner, T. Glöckler**, D. Rueda-Delgado,** T. Abzieher, M. Jakoby, B. Richards, U. W. Paetzold, I. A. Howard, and U. Lemmer. *Triple cation mixed-halide perovskites for tunable lasers*. Opt. Mater. Express **2017** 7, 4082-4094 https://doi.org/10.1364/OME.7.004082

Conference poster

- Solution-processed C_{60} as passivating layer in perovskite solar cells. KSOP Summer School, Bad Herrenalb, Germany, 4 – 6.09.18 (Poster)
- Influence of passivating layers in perovskite-based solar cells. PhD Seminar on Photovoltaics, Karlsruhe, Germany, 11.10.17 (Presentation)
- Optical and electrical studies of charge carrier mechanisms in perovskite solar cell. KSOP Spring Seminar, Karlsruhe, Germany, 14.03.17 (Presentation)
- Light soaking induced enhancement of carrier lifetime in CH3NH3PbI3 layers. Europhotonics Spring School 2016, Porquerolles, France, 29 – 31.04.16 (Presentation)
- Photoluminescence studies on $CH_3NH_3PbI_3$: light soaking effect on carrier lifetime and influence of fabrication parameters. International Conference on Perovskite Solar Cells and Optoelectronics (PSCO), Genova, Italy, 26 – 28.09.2016 (Poster)
- Time-resolved Photoluminescence of Perovskite layers. Europhotonics Spring School 2015, Paderborn, Germany, 13 – 16.04.15 (Poster)
- Hybrid solar cells based on Perovskite Materials. Europhotonics Spring School 2014, Porquerolles, France, 31.03- 3.04.14 (Poster)

Acknowledgments

Doing a Ph.D. and writing a thesis requires strong doses of motivation, inspiration, and enthusiasm to overcome those moments of frustration and exhaustion. This is why I to thank all who were there when I needed it and who walked with me during this challenging but amazing time. First of all, none of this would be possible without the Erasmus Mundus Scholarship fund and the committee organizing the Erasmus Mundus Joint Doctorate program, Europhotonics. The opportunity that is granted to me allowed me to come to the European Union to study and work, to meet so many and diverse new people, to grow more as a scientist. Thanks to this journey, I continue to discover parts of myself I didn't know about before. Thank you for your support.

I would like to thank Prof. Dr. Uli Lemmer for his support, guidance, and patience. It is very easy to be overcome with the frustration of lab work and lose sight of your work. In these moments, I would seek him out to discuss my experiments and frustration and these discussions would always motivate and illuminate me. Conferring with him always lifted my spirits and helped me realize the value of my work. Thank you for always backing me up.

When I arrived to Karlsruhe, I was welcomed in the Karlsruhe School of Optics and Photonics and I would like to thank them for their hard work. I always looked forward to every KSOP event (the modules, the MBA fundamentals, the summer schools, and KDOPs) as a way to remain on the loop of what is being done in KIT and as a way to connect with other Ph.D. students facing the same challenges. Additionally, I would like to thank both KSOP and the DAAD for their financial support in the later years of my studies.

La primera persona que me recibió en Karlsruhe fue Dr. Aina Quintilla, gracias por invitarme a hacer el doctorado en Alemania, por darme la bienvenida. Por recibirme de brazos abiertos y por tu apoyo en los años que trabajamos juntas. Discutir contigo siempre fue un reto, pero era un reto divertido.

I would like to thank Dr. Uli Paetzold for his guidance. Through the many discussions and meetings, he helped bring clarity and structure to my ideas and for that, I am deeply grateful.

I would like to thank also the jury and the committee that evaluated this dissertation. Thank you for your valuable time and comments.

Ana, Ihteaz, Isabel, Laura, Oonagh, Ruben, Simon, and Tomás: thank you for reviewing this document. I really appreciate the time you invested and the comments you sent my way.

For answering my questions regarding the administrative topics, I would like to thank Claudia Holstein and Astrid Henne. Thank you for always being very welcoming and kind.

Part of my research time is executed in ICFO (Barcelona) and for the two periods I was there, everyone received me with open arms. I would like to make a special mention to the Functional

Optoelectronic Nanomaterials Group lead by Prof. Dr. Gerasimos Konstantatos: they are kind enough to answer my questions and to guide me into the ICFO world.

In the beginning, when I arrived to Karlsruhe I was very lucky to be welcomed by the MNOS group: Ruben-sama, Jan, Andreas, Anna, Katja, Carola, Siegfried, Matthias. Thank you for welcoming me into the German world, and teaching me how to move in this brand new world. Thank you for teaching me about the Feuerzangenboule, for painting with me my first Easter eggs, and for teaching me the long-honored German ways. I will never forget. Thanks also to the great spirit of the taskforce perovskite.

I would like to thank OSKar, for providing a group where we could discuss topics on optics, but also dance all night. Thank you for welcoming the new students arriving at Karlsruhe, who may feel a little bit lost and confused. May you always be there to provide them with a home away from home.

Thanks to the lunch group- whose name could easily be improved to the Cool People Table or Great and Funky Discussions over Coffee-: Isabel, Ihteaz, Simon, Andres, Leo, Fabian, Saba, Sara, and Ali (on our outings). Thank you for the funny moments, for the angry moments, for the funky conversations, for the venting moments, for the coffee breaks, and for the playing times. Even though feeling frustrated and powerless is not a good thing, it is always better when it´s shared.

Thanks to the LM group. May coffee always shower over you (hopefully not terribly hot) and may you always have a friend to remove the cement from your feet (inside joke).

Thanks to the Lichtgestalten group. Discussions with you guys had a tendency to go into the crazy very fast (*inverosímil* is the word I would use), often leaving behind just confused faces: Andres V, Charlie, Mr. Corni, Ivan, Jakob, Adi, Artyom, Diego, Isa (again), John, Patrick, Tobias, coffee Florian, and movie Florian. Thanx for putting a spark on my day.

Gracias a aquellos que están viviendo en Barcelona o que conocí durante mis estancias allá: Anita, Lisa, Javier, Rodri, Sebas. Su calidez y vida me impulsó en momentos donde lo necesitaba. Gracias por la oportunidad de conocerlos y gracias por permitirme entrar en sus vidas. Quisiera reconocerle el apoyo a Xavi, que estaba viviendo su propio proceso de escritura y que fue un apoyo increíble a la hora de establecer horarios y empujarnos el uno al otro a cumplir nuestros logros diarios.

Quiero agradecerle de nuevo a Isabel, cuyo apoyo incentivo la desaparición de lo gris de mi frustración. Gracias por tu apoyo y tus preguntas, que en su momento me molestaron, pero que eran piedritas que servían para empezar a moverme. Obrigada. Gracias Emilio por las discusiones sobre EQE, que rápidamente se volvían discusiones sobre la vida, obra y filosofía. Gracias a mis amigos en otros mares: Carolina, Gabriel, Andrés Z, Alberto, que me recuerdan partes de mí misma que a veces se me olvidan. Gracias por estar pendientes en la distancia.

Gracias a Laurita que me ayudó en todo el proceso y al final me dió el último empujoncito para terminar este trabajo dentro de un tiempo finito. Por sus llamadas, sus ayudas, su organización, por su paciencia. Gracias. Espero en algún momento poder darte el apoyo que me has dado. Gracias a mis papás, por su apoyo, sus llamadas, por su calma y su amor incondicional. Siempre han sido un puerto seguro y en calma en la tormenta.

Gracias ..... totales

Appendix

A. Solution-processed C_{60} ITO side

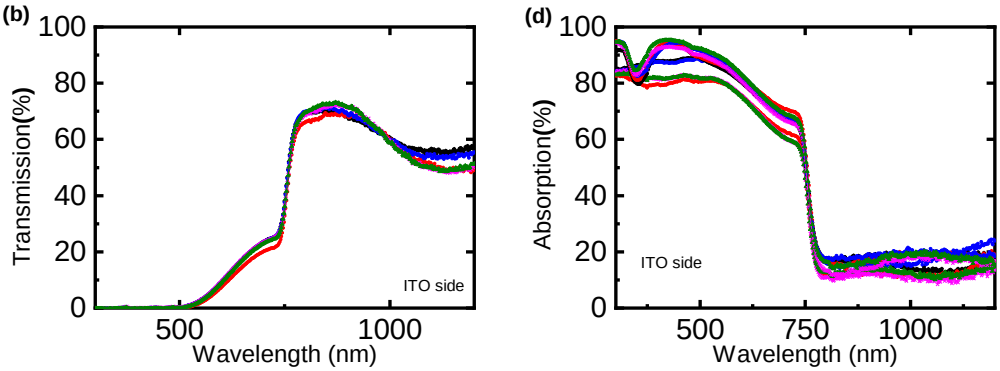

Figure 57. UV-Vis spectra of the ITO/SnO_2/C_{60}/$MAPbI_{3-x}Cl_x$ architecture, with different C_{60} layers. Transmittance spectra (a), (b) absorptance spectra (c) of $MAPbI_{3-x}Cl_x$ on ITO/SnO_2/C_{60} (calculated from the measurements at ITO side).

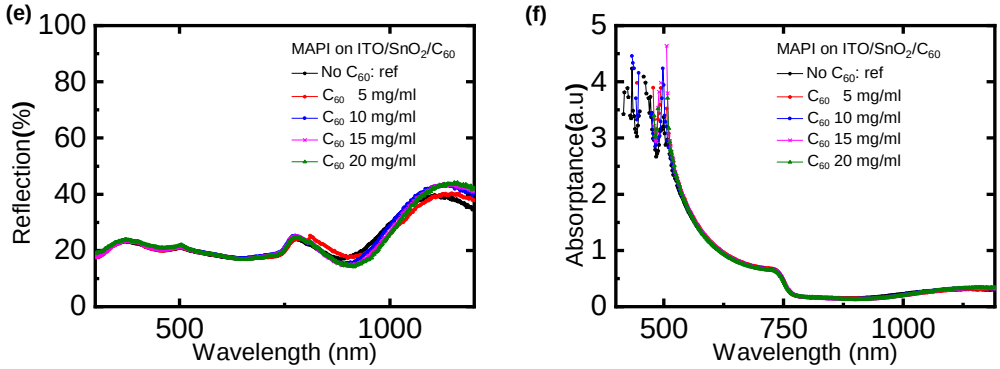

Figure 58. UV-Vis spectra of the ITO/SnO_2/C_{60}/$MAPbI_{3-x}Cl_x$ architecture, with different C_{60} layers (c) Reflection spectra from the air side, (f) Absorbance of $MAPbI_{3-x}Cl_x$ on ITO/SnO_2/C_{60} (calculated from the measurements at air side).

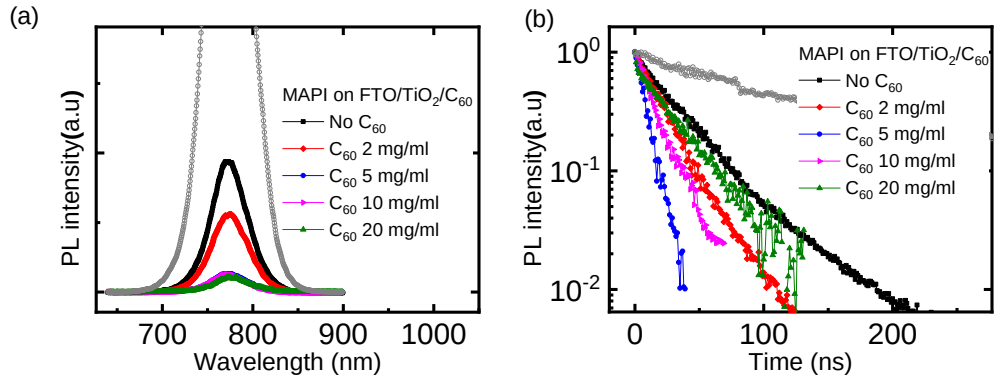

Figure 59. Steady-state and time-resolved PL of perovskite layers deposited on FTO/TiO_2/C_{60} in different concentrations. C_{60} is solution processed and the perovskite layers if deposited

using the lead acetate method. In gray, the data for the perovskite layer on glass.

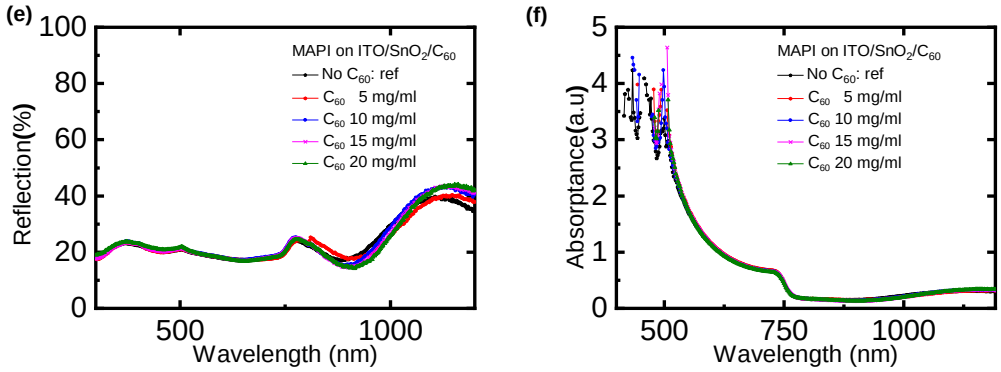

Figure 60. UV-Vis spectra of the ITO/SnO_2/C_{60}/$MAPbI_{3-x}Cl_x$ architecture, with different C_{60} layers (c) Reflection spectra from the air side, (f) Absorbance of $MAPbI_{3-x}Cl_x$ on ITO/SnO_2/C_{60} (calculated from the measurements at air side).

B. Evaporated C_{60} as interlayer.

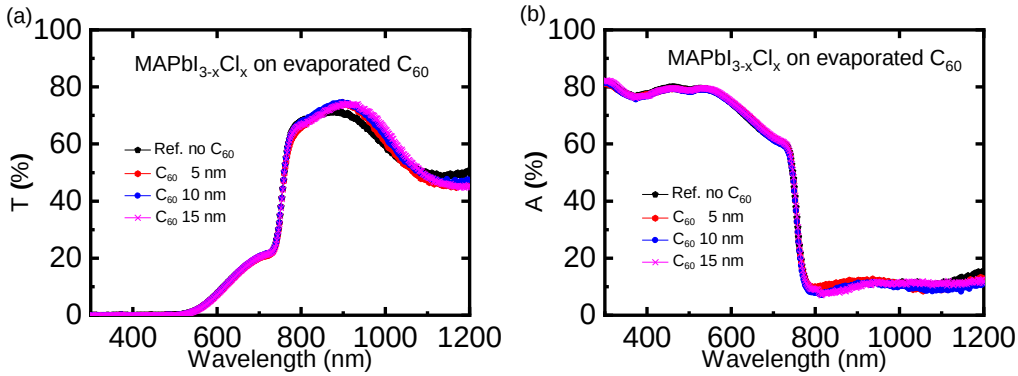

Figure 61. UV-Vis spectra of the ITO/SnO_2/C_{60}/$MAPbI_{3-x}Cl_x$ architecture, with C_{60} deposited through thermal evaporation. (a) Transmittance spectra (b) Absorptance spectra of $MAPbI_{3-x}Cl_x$ on ITO/SnO_2/C_{60} (measured from air side).

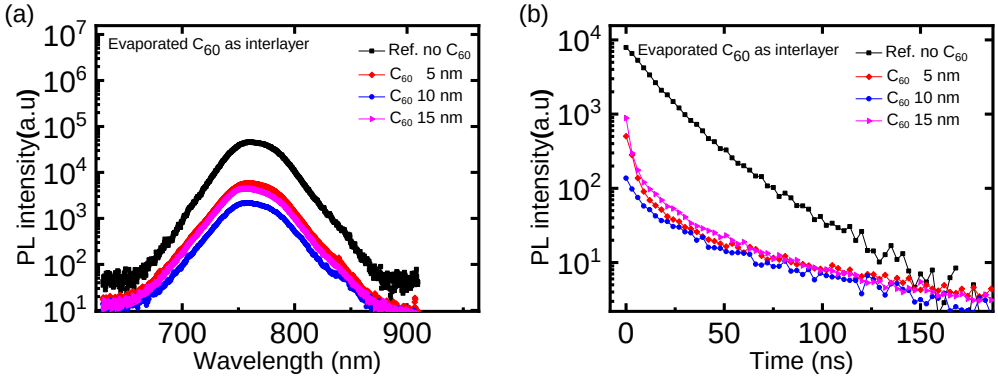

Figure 62. (a) Steady-state and (b) Time-resolved Photoluminescence of perovskite layers on glass, ITO/ (reference), and ITO/ C_{60} in different concentrations. In grey, the perovskite layer on glass for comparison.

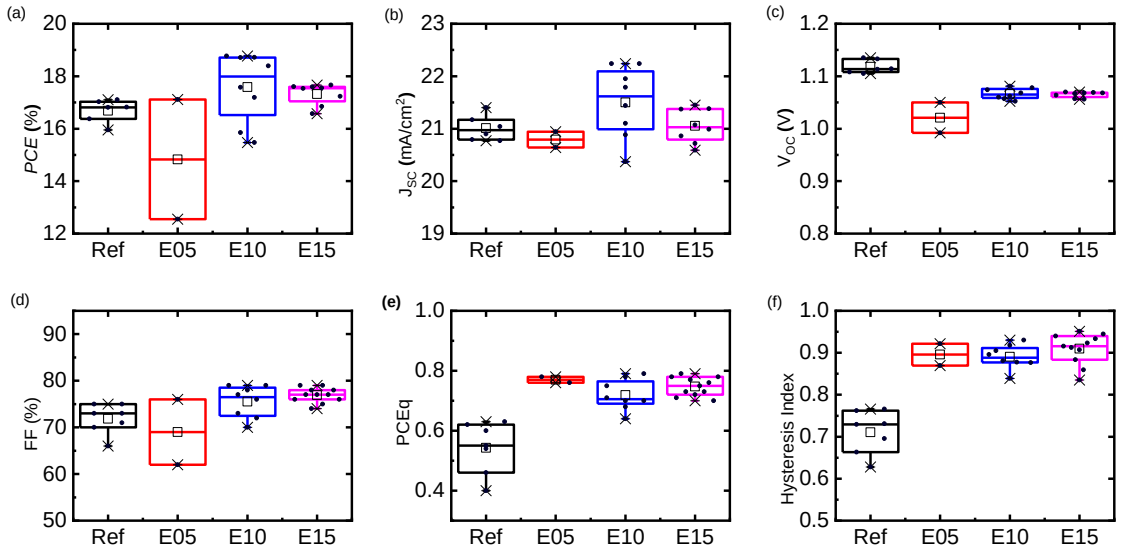

Figure 63. Statistical parameters extracted from the *J-V* characteristic curves of solar cells with the architecture: ITO/C_{60}/$MAPbI_{3-x}Cl_x$ /Spiro/Au, where C_{60} is evaporated. a.) power conversion efficiency, b.) Open circuit voltage, c.) Short-circuit current, d.) Fill factor, e.) PCE quotient f.) Hysteresis index.

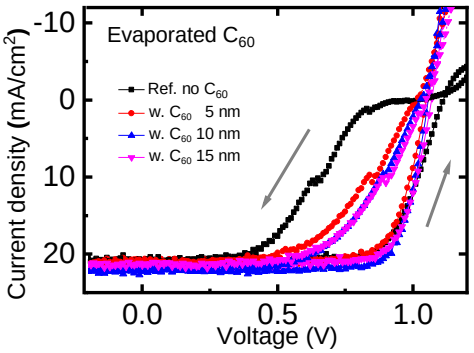

Figure 64. *J-V* characteristic curve of solar cells with the architecture: ITO/SnO_2/C_{60}/$MAPbI_{3-x}Cl_x$ /Spiro/Au, with C_{60} evaporated as interlayer in different thickness.

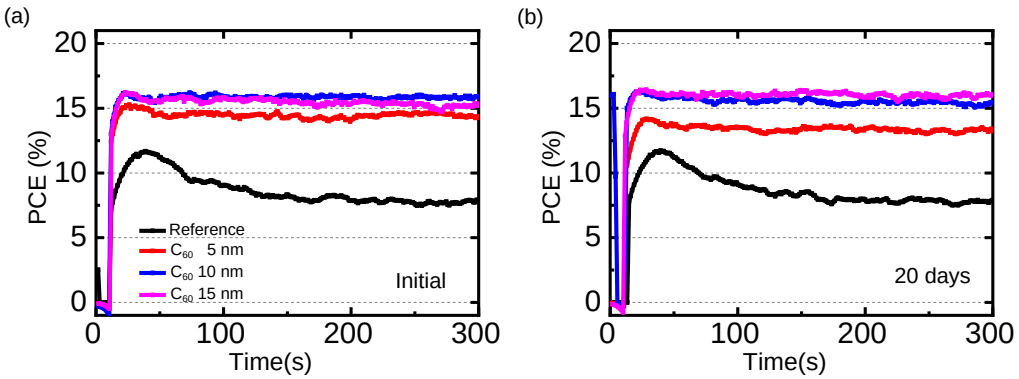

Figure 65. Evolution of the PCE at constant voltage for architecture: ITO/SnO_2/C_{60}/$MAPbI_{3-x}Cl_x$, where C_{60} is evaporated. The data is measured: (a) upon fabrication, (b) after 20 days.

C. C_{60} as ETL optical characterization.

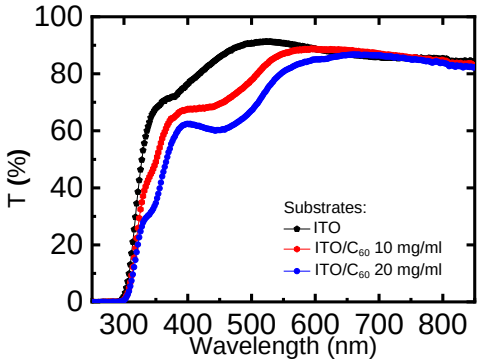

Figure 66. Tranmittance spectra of substrates: ITO, ITO/C_{60} (10 mg/ml) and ITO/ C_{60} (20 mg/ml).

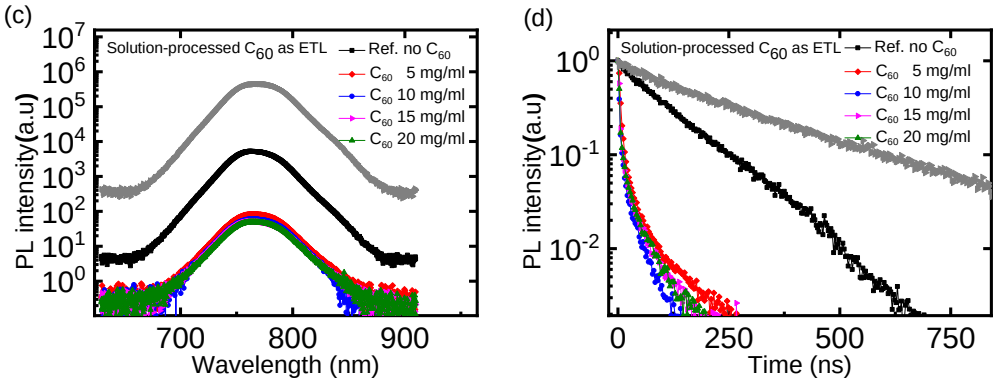

Figure 67. (a) Steady-state and (b) Time-resolved Photoluminescence of perovskite layers on glass, ITO/ (reference), and ITO/ C_{60} in different concentrations. In grey, the perovskite layer on glass for comparison.

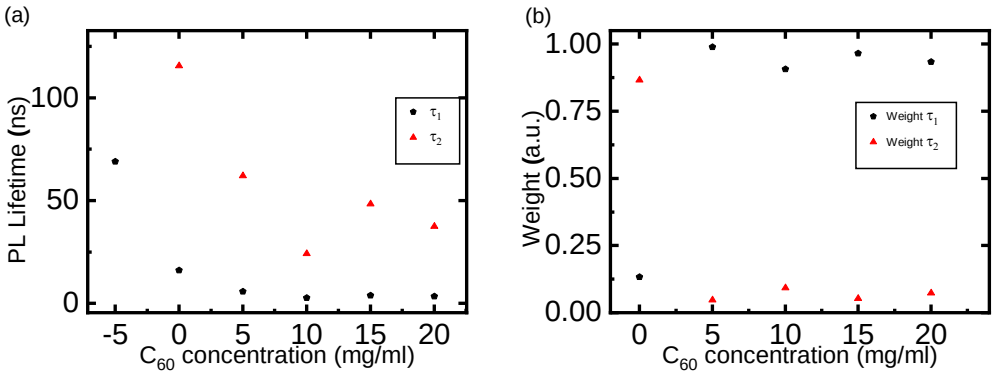

Figure 68. PL analysis plots of the layer architecture: ITO/C_{60}/$MAPbI_{3-x}Cl_x$ a.): Lifetimes and weights obtained from fitting the equation: $y(t)=y0+A1*\exp(-t/\tau_1)+A2*\exp(-t/\tau_2)$.

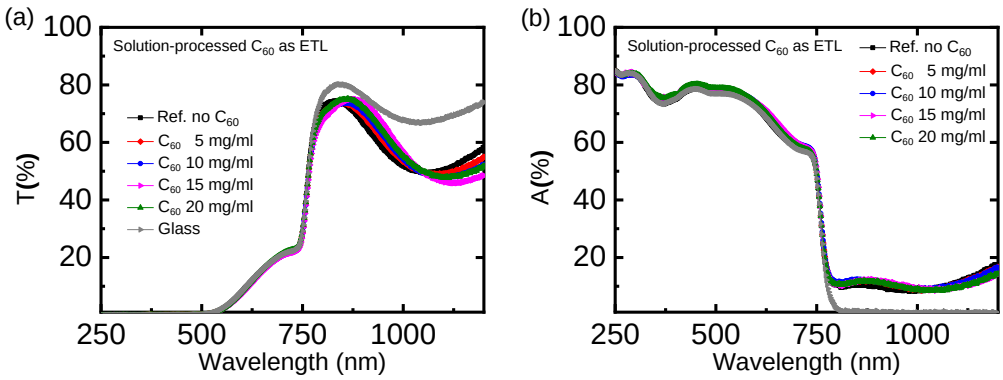

Figure 69. UV-Vis spectra of the ITO/ C_{60}/$MAPbI_{3-x}Cl_x$ architecture, with different C_{60} layers (c) Transmittance spectra (f) Absorptance spectra. All spectra are measured from the air side.

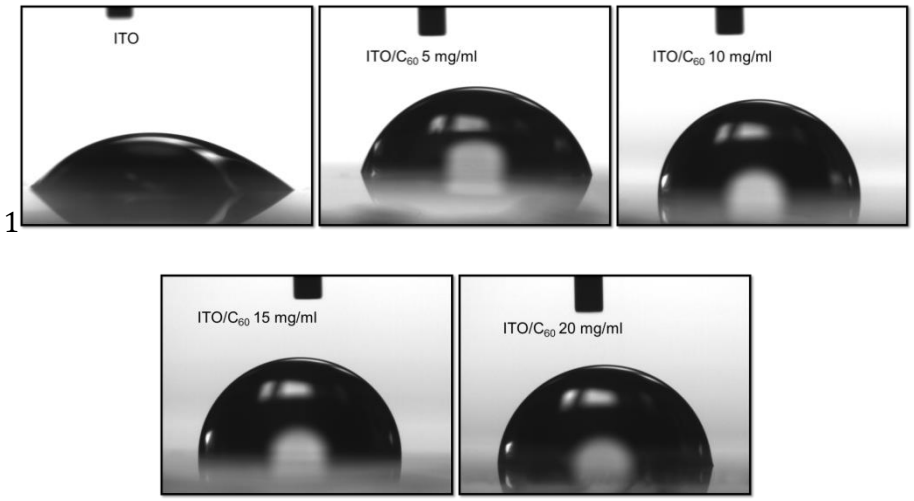

Figure 70. Water droplet on ITO/C_{60} in different concentrations

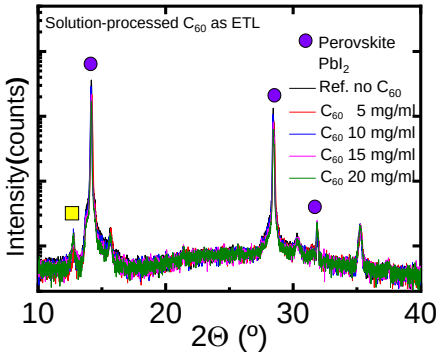

Figure 71. XRD layers with the ITO/ C_{60} /$MAPbI_{3-x}Cl_x$ architecture, with different C_{60} solution-processed ETL. In black, the perovskite layer deposited on ITO.

D. Optimization of fabrication parameters (others)

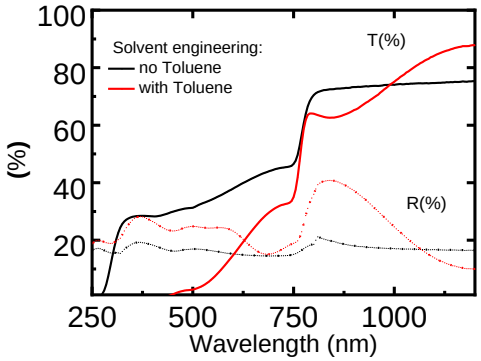

Figure 72. Transmittance and reflectance spectra of perovskite layer fabricated with the lead iodide method, with and without solvent-engineering step (toluene).

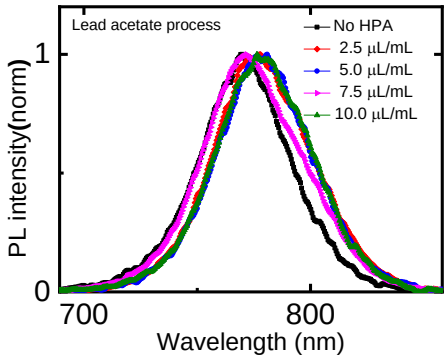

Figure 73. Normalized PL spectra of perovskite layers on glass deposited with the lead acetate method, with different HPA concentration (Figure 24)

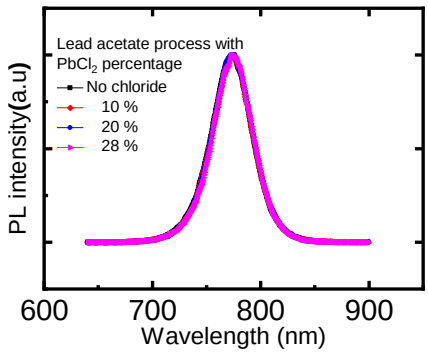

Figure 74. Normalized steady-state PL of MAPI on glass, with different $PbCl_2$ percentage in the perovskite solution (From Figure 26)

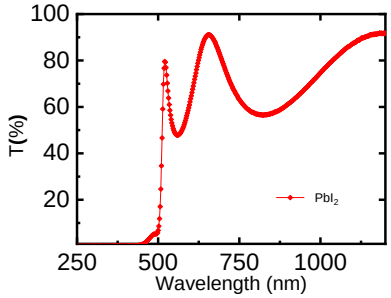

Figure 75. Transmittance spectra of lead iodide (PbI_2) spin-coated on glass.

E. Detailed preparation steps

The substrates have to be cleaned with glass cleaning detergent and water before placing them in the ultrasonic baths. Two ultrasonic baths are necessary: acetone and isopropanol. Before SnO_2 deposition, the surface of the samples is plasma cleaned in an O_2 plasma for 3 min at maximum power. Samples with SnO_2 layers can be stored in a glovebox. They however need to be completely cooled down before further depositions.

The C_{60} solution can be prepared up to 5 days before using, but it needs to be stirred thoroughly. Devices built with older C_{60} solutions show no difference from the reference. Before C_{60} deposition, the surface of the samples is plasma cleaned in an O_2 plasma for 1 min at 30 % the maximum power.

Before perovskite deposition, the surface of the samples is plasma cleaned in an O_2 plasma for 1 min at 30 % the maximum power. If C_{60} is the substrate, this step is executed before C_{60} deposition and skipped for the perovskite deposition.

The perovskite solution (optimized lead acetate single step) has to be mixed shortly before deposition. (Solutions mixed the day or hours before form layers with a white haze, signal of holes in the coverage).

For the slow dispense deposition technique, care should be take so the tip of the pipette does not touch the substrate below the drop.